



**HAL**  
open science

# Monte Carlo simulation of water diffusion through cardiac tissue and observation by virtual MRI

Yuhan Jing

► **To cite this version:**

Yuhan Jing. Monte Carlo simulation of water diffusion through cardiac tissue and observation by virtual MRI. Medical Imaging. INSA de Lyon, 2023. English. NNT : 2023ISAL0076 . tel-04427017

**HAL Id: tel-04427017**

**<https://theses.hal.science/tel-04427017>**

Submitted on 30 Jan 2024

**HAL** is a multi-disciplinary open access archive for the deposit and dissemination of scientific research documents, whether they are published or not. The documents may come from teaching and research institutions in France or abroad, or from public or private research centers.

L'archive ouverte pluridisciplinaire **HAL**, est destinée au dépôt et à la diffusion de documents scientifiques de niveau recherche, publiés ou non, émanant des établissements d'enseignement et de recherche français ou étrangers, des laboratoires publics ou privés.



# INSA

N°d'ordre NNT : 2023ISAL0076

## **THESE de DOCTORAT DE L'INSA LYON, membre de l'Université de Lyon**

**Ecole Doctorale N° ED 205 EDISS  
(INTERDISCIPLINAIRE SCIENCES-SANTÉ)**

**Spécialité/ discipline de doctorat :**  
Ingénierie biomédicale

Soutenue publiquement le 23/10/2023, par :  
**(Yuhan JING)**

---

# **Monte Carlo simulation of water diffusion through cardiac tissue and observation by virtual MRI**

---

Devant le jury composé de :

Cyril Poupon	Directeur de Recherche, CEA NeuroSpin	Président
Stéphanie Bricq	Maître de Conférences HDR, Université de Bourgogne	Rapportrice
Cyril Poupon	Directeur de Recherche, CEA NeuroSpin	Rapporteur
Bart Bijmens	Professeur, ICREA	Rapporteur
Carole Lartzien	Directeur de Recherche, INSA-LYON	Examinatrice
Stanislas Rappacchi	Chargé de recherche, Aix-Marseille Université	Examineur
Carole Frindel	Maître de Conférences HDR, INSA-LYON	Directrice de thèse

## Département FEDORA – INSA Lyon - Ecoles Doctorales

SIGLE	ECOLE DOCTORALE	NOM ET COORDONNEES DU RESPONSABLE
<b>CHIMIE</b>	<b>CHIMIE DE LYON</b> <a href="https://www.edchimie-lyon.fr">https://www.edchimie-lyon.fr</a> Sec. : Renée EL MELHEM Bât. Blaise PASCAL, 3e étage secretariat@edchimie-lyon.fr	<b>M. Stéphane DANIELE</b> C2P2-CPE LYON-UMR 5265 Bâtiment F308, BP 2077 43 Boulevard du 11 novembre 1918 69616 Villeurbanne <a href="mailto:directeur@edchimie-lyon.fr">directeur@edchimie-lyon.fr</a>
<b>E.E.A.</b>	<b>ÉLECTRONIQUE, ÉLECTROTECHNIQUE, AUTOMATIQUE</b> <a href="https://edeea.universite-lyon.fr">https://edeea.universite-lyon.fr</a> Sec. : Stéphanie CAUVIN Bâtiment Direction INSA Lyon Tél : 04.72.43.71.70 secretariat.edeea@insa-lyon.fr	<b>M. Philippe DELACHARTRE</b> INSA LYON Laboratoire CREATIS Bâtiment Blaise Pascal, 7 avenue Jean Capelle 69621 Villeurbanne CEDEX Tél : 04.72.43.88.63 <a href="mailto:philippe.delachartre@insa-lyon.fr">philippe.delachartre@insa-lyon.fr</a>
<b>E2M2</b>	<b>ÉVOLUTION, ÉCOSYSTÈME, MICROBIOLOGIE, MODÉLISATION</b> <a href="http://e2m2.universite-lyon.fr">http://e2m2.universite-lyon.fr</a> Sec. : Bénédicte LANZA Bât. Atrium, UCB Lyon 1 Tél : 04.72.44.83.62 secretariat.e2m2@univ-lyon1.fr	<b>Mme Sandrine CHARLES</b> Université Claude Bernard Lyon 1 UFR Biosciences Bâtiment Mendel 43, boulevard du 11 Novembre 1918 69622 Villeurbanne CEDEX <a href="mailto:sandrine.charles@univ-lyon1.fr">sandrine.charles@univ-lyon1.fr</a>
<b>EDISS</b>	<b>INTERDISCIPLINAIRE SCIENCES-SANTÉ</b> <a href="http://ediss.universite-lyon.fr">http://ediss.universite-lyon.fr</a> Sec. : Bénédicte LANZA Bât. Atrium, UCB Lyon 1 Tél : 04.72.44.83.62 secretariat.ediss@univ-lyon1.fr	<b>Mme Sylvie RICARD-BLUM</b> Institut de Chimie et Biochimie Moléculaires et Supramoléculaires (ICBMS) - UMR 5246 CNRS - Université Lyon 1 Bâtiment Raulin - 2ème étage Nord 43 Boulevard du 11 novembre 1918 69622 Villeurbanne Cedex Tél : +33(0)4 72 44 82 32 <a href="mailto:sylvie.ricard-blum@univ-lyon1.fr">sylvie.ricard-blum@univ-lyon1.fr</a>
<b>INFOMATHS</b>	<b>INFORMATIQUE ET MATHÉMATIQUES</b> <a href="http://edinfomaths.universite-lyon.fr">http://edinfomaths.universite-lyon.fr</a> Sec. : Renée EL MELHEM Bât. Blaise PASCAL, 3e étage Tél : 04.72.43.80.46 infomaths@univ-lyon1.fr	<b>M. Hamamache KHEDDOUCI</b> Université Claude Bernard Lyon 1 Bât. Nautibus 43, Boulevard du 11 novembre 1918 69 622 Villeurbanne Cedex France Tél : 04.72.44.83.69 <a href="mailto:hamamache.kheddouci@univ-lyon1.fr">hamamache.kheddouci@univ-lyon1.fr</a>
<b>Matériaux</b>	<b>MATÉRIAUX DE LYON</b> <a href="http://ed34.universite-lyon.fr">http://ed34.universite-lyon.fr</a> Sec. : Yann DE ORDENANA Tél : 04.72.18.62.44 yann.de-ordenana@ec-lyon.fr	<b>M. Stéphane BENAYOUN</b> Ecole Centrale de Lyon Laboratoire LTDS 36 avenue Guy de Collongue 69134 Ecully CEDEX Tél : 04.72.18.64.37 <a href="mailto:stephane.benayoun@ec-lyon.fr">stephane.benayoun@ec-lyon.fr</a>
<b>MEGA</b>	<b>MÉCANIQUE, ÉNERGÉTIQUE, GÉNIE CIVIL, ACOUSTIQUE</b> <a href="http://edmega.universite-lyon.fr">http://edmega.universite-lyon.fr</a> Sec. : Stéphanie CAUVIN Tél : 04.72.43.71.70 Bâtiment Direction INSA Lyon mega@insa-lyon.fr	<b>M. Jocelyn BONJOUR</b> INSA Lyon Laboratoire CETHIL Bâtiment Sadi-Carnot 9, rue de la Physique 69621 Villeurbanne CEDEX <a href="mailto:jocelyn.bonjour@insa-lyon.fr">jocelyn.bonjour@insa-lyon.fr</a>
<b>ScSo</b>	<b>ScSo*</b> <a href="https://edsciencessociales.universite-lyon.fr">https://edsciencessociales.universite-lyon.fr</a> Sec. : Mélina FAVETON INSA : J.Y. TOUSSAINT Tél : 04.78.69.77.79 melina.faveton@univ-lyon2.fr	<b>M. Bruno MILLY</b> Université Lumière Lyon 2 86 Rue Pasteur 69365 Lyon CEDEX 07 <a href="mailto:bruno.milly@univ-lyon2.fr">bruno.milly@univ-lyon2.fr</a>

\*ScSo : Histoire, Géographie, Aménagement, Urbanisme, Archéologie, Science politique, Sociologie, Anthropologie

# ABSTRACT

## MONTE CARLO SIMULATION OF WATER DIFFUSION THROUGH CARDIAC TISSUE AND OBSERVATION BY VIRTUAL MRI

Yuhan Jing

Ph.D. in Biomedical engineering

Advisor: Carole Frindel, Isabelle E. Magnin

September 2023

Diffusion magnetic resonance imaging shows great promise as a non-invasive technique for investigating biological tissues by analyzing the diffusion of water molecules. However, accurately assessing the diffusion properties of complex biological tissue micro-structures using practical MRI acquisitions remains a challenge. Monte Carlo simulation offers a solution by providing a ground truth and considering only the diffusion of water molecules within the tissues. Nonetheless, simulating diffusion presents three critical challenges: 1) generating a realistic tissue model as input, 2) setting the Monte Carlo simulator with optimal parameters, and 3) accounting for the impact of MR imaging sequence parameters on the observed diffusion. In this thesis, we developed various models of cardiac tissue with different degrees of realism in geometric and physical parameters and proposed scattering ground truths at optimal scales using Monte Carlo simulation. We then observed this diffusion using an MRI diffusion sequence with different parameter sets and quantified the observed diffusion distortion compared to the ground truths. This study aims to provide guidance for optimizing the observation parameters in MRI to accurately observe diffusion in cardiac biological tissues.

*Keywords:* Monte-Carlo simulation, water diffusion, microstructure, cardiac tissue, diffusion magnetic resonance imaging.

# Résumé

L'imagerie par résonance magnétique de diffusion offre de grandes perspectives en tant que technique non invasive pour l'étude des tissus biologiques en analysant la diffusion des molécules d'eau. Cependant, évaluer précisément les propriétés de diffusion des microstructures complexes des tissus biologiques à partir des acquisitions d'IRM pratiques reste un défi. La simulation de Monte Carlo offre une solution en fournissant une référence précise et en ne considérant que la diffusion des molécules d'eau au sein des tissus. Néanmoins, la simulation de la diffusion présente trois défis majeurs : 1) générer un modèle de tissu réaliste en entrée, 2) paramétrer le simulateur de Monte Carlo avec des paramètres optimaux, et 3) prendre en compte l'impact des paramètres de séquence d'imagerie par résonance magnétique sur la diffusion observée. Dans cette thèse, nous avons développé différents modèles de tissu cardiaque avec différents degrés de réalisme en termes de paramètres géométriques et physiques, et nous avons proposé des vérités de diffusion dispersées à des échelles optimales en utilisant la simulation de Monte Carlo. Ensuite, nous avons observé cette diffusion à l'aide d'une séquence de diffusion par IRM avec différents jeux de paramètres et quantifié la distorsion de diffusion observée par rapport aux vérités fondamentales. Cette étude vise à fournir des orientations pour optimiser les paramètres d'observation en IRM afin d'observer avec précision la diffusion dans les tissus biologiques cardiaques.

# Acknowledgement

I would like to express my sincere gratitude to all those who helped me during my thesis. First of all, I would like to warmly thank my PhD supervisors Carole FRINDEL and Isabelle MAGNIN, without whom this PhD would never have seen the light of day.

Isabelle, with her rich experience in the field of medical imaging, her ability to identify problems, her valuable suggestions regarding this adventure that is research, her patience in guiding me and her efforts to explain things clearly and simply, who helped me to finally finish this journey of doctoral research. I really appreciate these contributions, the time spent and her ideas on this work. I thank her very much for introducing me to the world of medical imaging and for supporting me so far. Her joy and enthusiasm for research and life have motivated throughout my PhD.

Carole, who guided me day by day, helped me to solve problems in detail, given me valuable advice on every aspect of this work and encouraged me when I lacked motivation. In addition to her scientific guidance, she is like a friend, sharing the toys and clothes to my daughter . Thanks to her, I had a very pleasant stay in France. I thank her from the bottom of my heart.

I'd like to express my gratitude to Wan-Yu LIU for recommending me to Creatis, which provided me with the opportunity to work in this top-level laboratory. I am grateful for his invaluable assistance throughout my journey.

I would also like to thank the members of my PhD jury, Ms. Carole LARTIZIEN, M. Stanislas RAPACCHI, especially the reviewers, Ms. Stéphanie BRICQ, Mr. Cyril POUPON, and Mr. Bart BIJNENS, for their expertise in evaluating my PhD work.

Thanks to my laboratory colleagues, they were always kind and patient. Thanks to Dr. Zexian WANG and Dr. Shunli WANG, with whom we have

shared work on the cardiac tissue structure and modeling. I also want to thank Prof. Yue-Min ZHU, for his help in deeper understanding of diffusion MRI and DTI. Thanks to Zinan LIU, his work about the motion of heart and DENSE MRI sequence helps me a lot. I also like to appreciate Patrick CLARYSSE, director of METISLAB, who helped me with administrative and financial aspects. Thanks also to Mr. Fabrice BELLET for the cluster instructions.

A big thank you to all my friends in France, Zexian WANG, Yunlong HE, Zinan LIU, Bingqing XIE, Yunyun SUN, Jiqing HUANG, Enyi CHEN, Zhiyuan LI, Ge FEI, thank you for all your help and encouragement over the years. Without you, life in France would not have been filled with happy and joyful memories. Finally, I'd like to thank my dear family, my husband, my daughter, all my best friends past and present over the years, today, not forgetting those I've met before, for their support, their listening, their encouragement, their help and their love. I'm very happy that you're always there for me.

# Contents

<b>I</b>	<b>Background</b>	<b>4</b>
<b>1</b>	<b>Structural and physical features of the cardiac tissue</b>	<b>5</b>
1.1	Heart structure at macroscopic scale . . . . .	6
1.2	Structure of the cardiac tissue . . . . .	8
1.2.1	Cardio-myocyte . . . . .	8
1.2.2	Extra-cellular matrix . . . . .	9
1.2.3	Laminar structure . . . . .	10
1.2.4	Myocyte transmural orientation change . . . . .	11
1.3	Cardiomyopathy . . . . .	12
<b>2</b>	<b>Diffusion magnetic resonance imaging</b>	<b>14</b>
2.1	Conventional MRI . . . . .	14
2.1.1	Principle . . . . .	14
2.1.2	Spatial encoding . . . . .	17

2.1.3	MRI Pulse Sequence . . . . .	19
2.2	Diffusion MRI . . . . .	20
2.2.1	History and development . . . . .	20
2.2.2	Principle . . . . .	22
2.2.3	Diffusion encoding schemes used for the <i>in vivo</i> heart . . . . .	23
2.2.4	Q-space encoding . . . . .	24
2.3	DMRI modeling and simulation . . . . .	25
2.3.1	Mathematical models in dMRI . . . . .	26
2.3.2	Bloch-Torrey analytical model . . . . .	29
2.3.3	Monte Carlo simulations . . . . .	32
<b>II</b>	<b>Contributions</b>	<b>35</b>
<b>3</b>	<b>Virtual cardiac tissue models</b>	<b>36</b>
3.1	State of the art . . . . .	36
3.2	Implementation . . . . .	37
3.2.1	One myocyte model . . . . .	37
3.2.2	Multi-cell models . . . . .	38
3.2.3	Global tissue model . . . . .	40
3.3	Conclusion . . . . .	42

<b>4</b>	<b>Water molecule diffusion simulation in cardiac tissue model</b>	<b>43</b>
4.1	State of the art . . . . .	43
4.2	Monte Carlo strategy . . . . .	45
4.2.1	Conditions on the Monte Carlo parameters . . . . .	50
4.2.2	Specific implementation for tissue model . . . . .	51
4.2.3	Evaluation . . . . .	54
4.3	Optimization of MC parameters . . . . .	55
4.3.1	Single-cell scale . . . . .	56
4.3.2	Multi-cell scale . . . . .	57
4.4	Conclusion . . . . .	65
<b>5</b>	<b>dMRI observation of water diffusion in cardiac tissue</b>	<b>67</b>
5.1	State of the art . . . . .	67
5.2	Virtual dMRI device . . . . .	69
5.2.1	Water diffusion displacements during two gradient pulses . . . . .	70
5.2.2	Physical versus Virtual observation . . . . .	71
5.2.3	Conditions on the MR observation parameters . . . . .	72
5.2.4	Evaluation . . . . .	73
5.3	Optimization of observation parameters . . . . .	74
5.3.1	Single-cell scale . . . . .	74

5.3.2	Multi-cell scale . . . . .	75
5.4	Conclusion . . . . .	84
<b>6</b>	<b>General conclusion and prospects</b>	<b>87</b>
6.1	Summary of contributions . . . . .	87
6.2	Discussion and future research . . . . .	88
6.3	Author’s contributions . . . . .	90
6.3.1	Journal articles . . . . .	90
6.3.2	International conference proceedings . . . . .	90

# List of Figures

1.1	(a) Heart anatomical structure at macroscopic scale. <a href="http://www.texasheartinstitute.org/hic/anatomy/anatomy2.cfm">http://www.texasheartinstitute.org/hic/anatomy/anatomy2.cfm</a> . (b) Heart wall structure. <a href="http://encyclopedia.lubopitko-bg.com/Structure of the Heart.html">http://encyclopedia.lubopitko-bg.com/Structure of the Heart.html</a> . . . . .	7
1.2	Histological cuts of human cardiac tissue ( $\times 20$ ) courtesy of TIMC, CNRS UMR 5525, France. Hematoxylin and Eosin staining. Cut perpendicular to cells (left) and cut parallel to cells (right). . . . .	8
1.3	Schematic of laminar structure model for cardiac fiber. Image from LeGrice et al. [1]. . . . .	10
1.4	(a) Definition of helix angle $\alpha$ and transverse angle $\beta$ . Image from Bernus et al. [2]. (b) Helix angle of Myocardial fiber orientation in the short axis plane of the left ventricle for normal 2 months human infant hearts from polarized lighted imaging. Image from Wang et al. [3]. . . . .	11
2.1	(a) Spinning protons. (b) Protons precessing around the field direction when placed in a strong magnetic field. (c) Definition of a proton's phase $\theta$ as the projection of its precession vector in a transverse plane. (d) Randomized phase of each proton after excitation. . . . .	16

2.2	$T_2$ decay: Normalized MRI signal in the transverse plane $S_0$ that fluctuates with the precession frequency $\gamma B_0$ and decreases exponentially. . . . .	17
2.3	Diagram of spin echo (SE) sequence and associated spatial encoding. $G_{sl}$ , $G_{pe}$ , and $G_{ro}$ represent the gradient fields used for slice selection, phase encoding, and frequency encoding, respectively. . . . .	19
2.4	(a) Classic MRI Pulsed Gradient Spin-Echo (PGSE) sequence [4] with a diffusion duration $\Delta$ , and a diffusion gradient pulse of duration $\delta$ and strength $G_d$ . (b) $T_2$ signal decay $S_0$ vs diffusion weighted signal decay $S$ . . . . .	22
2.5	Illustration of different diffusion coding schemes applied in cardiac dMRI. Image from Mekkaoui et al. [5]. . . . .	24
2.6	Analytical model of dMRI signal for a cylinder with diameter $d = 20\mu m$ according to Equation 2.22. (a) $\frac{S}{S_0}$ vs $q$ . (b) $\log \frac{S}{S_0}$ vs $q$ . . . . .	32
3.1	Simulated cylindrical cell (myocyte). Definition of elevation angle $\alpha$ and azimuth angle $\beta$ . . . . .	38
3.2	Simulated models of cardiac tissues: (a) Model I: periodic arrangement of parallel identical cells. Model II: parallel cells with heterogeneous diameters. Model III: identical cells with heterogeneous orientations. Model IV: cells with heterogeneous diameters and orientations. The cubic box represents one layer of cells. (b) Cross-sectional views, showing spatial restrictions: $d$ (green arrow) in the intracellular space (ICS); $a_l$ (red arrow) and $a_s$ (blue arrow) in the extracellular space (ECS). (c) Distribution of $d$ , $a_l$ , and $a_s$ within a voxel of size $Vb = 500 \times 500 \times 500\mu m^3$ . . . . .	39

3.3	(a) Global tissue model of size $2500 \times 3500 \times 500 \mu m^3$ . (b) Elevation angle $\alpha$ in Models III and IV: $\alpha$ varies only along the y axis while the azimuth angle $\beta$ remains equal to 0. . . . .	41
4.1	Generation of 3D direction of diffusion using two methods: Method 1 - (a) Elevation and azimuth angles $\alpha$ and $\beta$ , (b) Uniformly generated $\alpha$ and $\beta$ , (c) Distribution of x, y, and z-axis projections, and (d) Corresponding points generated on a sphere; Method 2 - (e) Uniformly generated x, y, z-axis projections, (f) Distribution of $\alpha$ and $\beta$ , and (g) Corresponding points generated on a sphere. .	47
4.2	Variation of the molecule density ratio between ICS and ECS with respect to $\Delta$ during Monte Carlo simulation of water diffusion in a permeable environment using Model IV with a mean cell diameter of $\mu_d = 20 \mu m$ . The Monte Carlo parameters employed are $N = 10^5$ and $\tau = 0.01 ms$ . . . . .	49
4.3	Virtual global tissue model with local change of orientation and three scales (voxel sizes). (a) Global tissue model of size $2500 \times 3500 \times 500 \mu m^3$ . (b) Digitized virtual model with $25 \times 35 \times 5$ voxels of size $V_s$ (c) $10 \times 14 \times 2$ voxels of size $V_m$ and (d) $5 \times 7 \times 1$ voxels of size $V_b$ . (a'-d') Elevation angle $\alpha$ in Models III and IV: $\alpha$ varies only along the y axis while the azimuth angle $\beta$ remains equal to 0.	52
4.4	2D section of a voxel and extended voxel containing cells (white disks) and water molecules (blue dots). (a) Voxel. (b) Extended voxel. The length $L_{ex}$ corresponds to the maximum length for which the water molecule can diffuse outside the voxel during $\Delta$ . (c) Extended voxel with water molecules limited to the inner voxel.	53
4.5	Single cell model- Optimization of $\tau$ and $N$ when $\Delta = 100 ms$ for two cell sizes. Simulation error $std_{\lambda_t^t}$ wrt $N$ . . . . .	56

4.6	Model IV - one voxel: Optimization of $\tau$ and $N$ within $Vb$ for two cell sizes. $std_{\lambda_3}$ wrt $N$ : a) ICS, $P = 0$ ; c) ECS, $P = 0$ ; e) whole voxel, $P = 0.2$ . Computation time $T$ wrt $N$ : (b,d,f) for (a,c,e) respectively. . . . .	58
4.7	Model IV - global model: Evolution of the eigenvalues $\lambda^t$ from a transient to a stationary regime according to the diffusion time $\Delta$ in ICS, ECS, and in the whole voxel, respectively. MC simulations were performed for model IV and voxels of size $Vs$ (first line) and $Vb$ (second line) with $D_{ICS}=1$ , $D_{ECS}= 2.5$ , $R_{ICS}=70\%$ , $\tau = 0.01ms$ , $\rho = 0.1/\mu m^3$ and $\rho = 8 \times 10^{-4}/\mu m^3$ for $Vs$ and $Vb$ respectively. . . . .	60
4.8	Models I-IV global models-Spatial representation of estimated values of $\lambda_3$ ( $\mu m^2/ms$ ) with three scales ( $Vs, Vm$ and $Vb$ ) when $\Delta = 100ms$ displayed using the colorbar given on the right. Normalized distribution of cell diameters displayed in one voxel in Models II and IV (the case of heterogeneous cell diameter) with $\mu_d = 20$ . . . . .	62
5.1	(a) Classic MRI Pulsed Gradient Spin-Echo (PGSE) sequence with diffusion duration $\Delta$ , pulse duration $\delta$ , and gradient strength $ \vec{G} $ [4]. (b) Water molecule moves in a free diffusion environment, $L1(\delta = 0)$ : displacement from start to end point; Bold lines: moves during diffusion gradient pulses; x: location of the centers of mass; $L2$ : displacement between consecutive centers of mass. (c) Simulated restricted (radial) and free (axial) diffusion MRI signals $E_{\vec{G}}(\Delta, \delta,  \vec{G} )$ (Eq. 5.2) of $N = 10^5$ water molecules diffusing in a cylindrical core of diameter $d = 20\mu m$ with $D = 1\mu m^2/ms$ , $\delta = 5ms$ , $ \vec{G}  = 80\mu T/mm$ . . . . .	70

5.2	Single cell model: (a) Exploring the <i>Conditions LDD</i> : Evolution of $\frac{S}{S_0}$ along radial direction vs $qr$ for $\Delta = 25 - 75ms$ when $\delta = 0.4ms$ . (b) Exploring the <i>Conditions SGP</i> : Evolution of $\frac{S}{S_0}$ along radial direction vs $qr$ for $\delta = 0.4 - 20ms$ when $\Delta = 100ms$ . Other MC parameters are set according to: $D = 1 \times 10^{-3}mm^2/s, \tau = 0.1ms$ and $N = 10^6$ . . . . .	74
5.3	(a-c) Cross sections (restricted planes) of three homogeneous models: (a) Case 1 where $d = 14\mu m, a_s = 2\mu m, a_l = 16\mu m, R_{ICS} = 69\%$ ; (b) Case 2 where $d = 20\mu m, a_s = 3\mu m, a_l = 20\mu m, R_{ICS} = 69\%$ ; (c) Case 3 where $d = 26\mu m, a_s = 4\mu m, a_l = 24\mu m, R_{ICS} = 69\%$ . (d) Cross section of the heterogeneous model where $\mu_d = 20\mu m, \mu_{a_s} = 3\mu m, \mu_{a_l} = 20\mu m, R_{ICS} = 69\%$ . . . . .	76
5.4	Model IV - one voxel: Exploring $\delta/\Delta$ condition: Evolution of $\lambda_3^t$ and $\lambda_3^o$ values wrt $\Delta$ for $\delta = 2 - 30ms$ . First line: $\lambda_3$ in ICS, second line: observation bias ( $\lambda_3^t - \lambda_3^o$ ) in ICS, third line: $\lambda_3$ in ECS. Conditions are not satisfied in hatched areas (e.g., for $\delta = 2ms$ ) bounded by critical values $\Delta^{critical}$ (vertical lines). Blue vertical line for $\delta = 2ms$ , orange for $\delta = 10ms$ , purple for $\delta = 30ms$ . Note that some curves may appear truncated due to the requirement that $\delta$ must always be smaller than $\Delta$ . MC parameters: $N = 10^5, \tau = 0.001ms$ . Observation parameter: $b = 500s/mm^2$ . . . . .	77

5.5 Models I and IV one voxel-Exploring LDD condition,  $\xi_{\Delta} = \Delta D / (s/2)^2 \geq 1$ : Evolution of  $\lambda_3^t$  and  $\lambda_3^o$  values wrt  $\Delta$ . First line:  $\lambda_3$  in ICS, second line: corresponding  $|L_{\lambda_3}|$  in ICS, third line:  $\lambda_3$  in ECS. Conditions are not satisfied hatched areas (e.g., for Model I case 1) bounded by critical values  $\Delta^{critical}$  (vertical lines) where  $\xi_{\Delta}(\Delta = \Delta^{critical}) = 1$ . Blue vertical line for Model I case 1, orange for Model I case 2, purple for Model I case 3. A horizontal arrow indicates the range of  $\Delta^{critical}$  for the heterogeneous model. Note that some curves may appear truncated due to the requirement that  $\delta$  must always be smaller than  $\Delta$ . MC parameters:  $N = 10^5, \tau = 0.001ms$ . Observation parameters:  $\delta = 30ms, b = 500s/mm^2$ . . . . . 79

5.6 Models I and IV one voxel-Exploring SGP condition,  $\xi_{\delta} = \delta D / (s/2)^2 \leq 0.3$ : Evolution of  $\lambda_3^t$  and  $\lambda_3^o$  values wrt  $\delta$  for  $\Delta = 170ms$ . First line:  $\lambda_3$  in ICS, second line: corresponding  $|L_{\lambda_3}|$  in ICS, third line:  $\lambda_3$  in ECS. Conditions are not satisfied in hatched areas (e.g., for Model I case 1) bounded by critical values  $\delta^{critical}$  (vertical lines) in ICS where  $\xi_{\delta}(\delta = \delta^{critical}) = 0.3$ . Blue vertical line for Model I case 1, orange for Model I case 2, purple for Model I case 3. A horizontal arrow indicates the range of  $\delta^{critical}$  for the heterogeneous model. MC parameters:  $N = 10^5, \tau = 0.001ms$ . Observation parameters:  $\Delta = 170ms, b = 500s/mm^2$ . . . . . 82

# List of Tables

1.1	Structural and physical cardiac tissue features. . . . .	9
3.1	Virtual tissue model parameters . . . . .	37
4.1	Virtual water diffusion : Monte Carlo simulation parameters . . . . .	44
4.2	Extended voxels: inner and outer voxels edges when $L_{ex} = 100\mu m$ with their corresponding water molecules density $\rho$ At the beginning of simulation when $N = 10^5$ . . . . .	53
4.3	Model IV - one voxel: <i>Condition l/s</i> . White cells satisfy the results of optimization of $\tau$ obtained from the analysis of Figure 4.6 . . . . .	59
4.4	Models I-IV - global model: Voxel size optimisation by reporting voxel size $V$ , mean cell diameter $\mu_d$ , cells number, cellular volume fraction, estimated $\lambda_1^t$ and $\lambda_3^t$ for two $d$ cases when $\Delta = 100ms$ . White cells correspond to a standard deviation of $\lambda_3^t$ less than 0.012. . . . .	64
5.1	Diffusion MRI : Clinical <sup>1</sup> vs Virtual MRI . . . . .	68
5.2	Micro-structural information obtained from MC simulation . . . . .	75

5.3	Critical values of $\Delta$ that satisfy the <i>LDD Condition</i> according to Figure 5.5, depending on the tissue model characteristics ( $d$ , $\mu_d$ , $a_l$ and $\mu_{a_l}$ ) and compartments (ICS and ECS). . . . .	80
5.4	Estimated $FWHM^t$ and $d^t$ from $ L_{\lambda_3^t} $ in ICS for different $\Delta$ ( $\xi_\Delta$ ) in the case of heter. model with $\mu_d = 20\mu m$ and $D = 1\mu m^2/ms$ . . . . .	81
5.5	Critical values of $\delta$ that satisfy the <i>SGP Condition</i> under <i>LDD Condition</i> , as determined by tissue model characteristics ( $d$ , $\mu_d$ , $a_l$ and $\mu_{a_l}$ ) in ICS. . . . .	84
5.6	Estimated $FWHM^o$ and $d^o$ from $ L_{\lambda_3^o} $ in ICS for different $\delta$ ( $\xi_\delta$ ) when <i>Condition LDD</i> is satisfied in the case of heter. model with $\mu_d = 20\mu m$ . . . . .	84

# General introduction

MRI is a powerful tool that detects the magnetic properties of hydrogen nuclei in water molecules using a strong magnetic field. It works by stimulating these magnetized nuclei with radiofrequency waves at a specific frequency, which makes them emit radiofrequency waves of their own. These emitted waves are then captured by a coil. By analyzing the subtle changes in the magnetic field and frequencies generated by the magnetic gradient field, MRI encodes spatial information and generates detailed images.

Diffusion MRI has emerged as a promising method for revealing the micro-tissue architecture. It monitors the displacements caused by the diffusion of water molecules at a resolution beyond the capabilities of traditional MRI. The overall signal observed in diffusion-weighted images at millimeter resolution is a result of statistically integrating all the distributions of microscopic displacements of water molecules present in a voxel. The diffusion process in biological tissues is typically described by the "apparent diffusion coefficient" (ADC), a statistical parameter reflecting the interaction between water molecules and tissue restrictions. ADC values significantly decrease during the early stages of acute brain ischemia, while higher ADC values can indicate conditions like edema, tumor cellularity, cystic astrocytoma, hydrocephalus, acute myocardial infarction, and hypertrophic cardiomyopathy.

To assess the anisotropy of diffusion in tissues, a tensor model was proposed, which considers the principal eigenvector of the diffusion tensor as parallel to the mean orientation of the tissue in the corresponding voxel. This concept has provided novel 3D information about fiber structures such as white matter tracts or myocardial fibers that were previously difficult to visualize using other imaging techniques.

Q-space imaging, which involves acquiring diffusion data for various values

of diffusion gradients, angular directions, and strength, offers a new way to accurately measure the size of cells. The free diffusion coefficient of water in a free environment at 37°C is approximately  $3.0\mu m^2/ms$  and follows a Gaussian distribution. In biological tissues, the "apparent diffusion coefficient" (ADC) is smaller (2 to 10 times) than that of free water diffusion due to factors such as high viscosity, macro-molecular crowding, and restriction in the intra-cellular space. Additionally, the ADC depends on MRI observation parameters such as diffusion duration, gradient pulse duration, overall diffusion weighting, observed direction, and voxel size. Understanding the relationship between ADC as observed in MRI and the microscopic characteristics of biological tissues is the subject of ongoing research.

Various models have been proposed to handle the non-Gaussian behavior of water diffusion in biological tissues, including the bi-exponential model, gamma model, truncated Gaussian model, Karger model, random permeable barrier model, and parallel series approximation. However, these models have limitations in assessing water diffusion in complex systems. The relative importance of different factors influencing water diffusion and their effects on MRI signals are still not fully understood and can sometimes be controversial.

Monte Carlo simulation, which dynamically simulates the movement of particles in space and time within tissue structures, offers the opportunity to study various models of interactions between molecules and tissue membranes. Previous Monte Carlo simulations using biological tissue models have revealed that physical and structural features such as cell shape, size, arrangement, volume fraction, membrane permeability, and diffusivity can influence the diffusion properties and modify the acquired dMRI signals. However, these simulations are complex and computationally intensive, often requiring simplifications to reduce the simulation load. Furthermore, choosing appropriate Monte Carlo simulation parameters is crucial to ensure accuracy, and conditions such as the "short gradient pulse" and "long diffusion duration limit" have been proposed to improve simulation reliability.

In this study, we propose simplified cardiac tissue models with realistic structural and physical parameters inspired by histological and physical measurements. These models are coupled with a multi-scale Monte Carlo water diffusion simulator to create a virtual ground truth, ranging from the cellular scale to the MRI observation scale. We then observe simulated water diffusion using a virtual MRI imaging device to study the impact of acquisition parameters on the accuracy of observed water diffusion characteristics compared to the simulated ground truth.

**Chapter 1** provides an overview of the anatomical structure and physical features of the heart. **Chapter 2** explains the principles of diffusion MRI, the theoretical aspects of dMRI modeling and simulation using Monte Carlo methods, and the existing state of the art. **Chapter 3** describes the construction of four cardiac tissue models of increasing realism. **Chapter 4** details the process of creating the ground truth by optimizing Monte Carlo simulation parameters and coupling the cardiac tissue models with Monte Carlo simulation. In **Chapter 5**, we analyze the results of different settings of the diffusion MRI sequence and their impact on the observed water diffusion characteristics compared to the ground truth. Finally, **Chapter 6** presents the general conclusions and future prospects of the study.

# Part I

## Background

# Chapter 1

## Structural and physical features of the cardiac tissue

The heart is one of the most important organs in the body, transporting blood, nutrients and oxygen to the rest of the body through powerful heart muscle contractions. Actually, the motion of heart is a highly complex system, with intrinsic different cell type distributions, complex electro-mechanical properties and an organized activity sequences. There is a close relationship between the local three-dimensional arrangement of Myocardial cells (myocytes) and the mechanical function [6], electrophysiology[7], and structural remodeling [8] of the heart. Some studies have also indicated that changes in physical and structural characteristics of cardiac tissue may be linked to cardiovascular disease [9, 10, 11, 12, 13, 14, 15, 16]. Heart tissue structure and physical feature research provides the theoretical basis and data support for the diagnosis and treatment of cardiovascular disease, which has great scientific significance.

In this chapter, we illustrate the structural and physical features of the heart tissue and introduce some cardiovascular diseases related to changes in physical and structural characteristics.

## 1.1 Heart structure at macroscopic scale

As we all know, the heart is the size of a fist and is located in the chest cavity. The base of the heart is the broad upper part of the heart from which the large blood vessels emerge, and the apex of the heart is the lower part pointing to the left. In general, as shown in Figure 1.1-a, the heart can be divided into three main distinct parts according to its physical characteristics and function: the chambers, the valves and the walls.

The whole heart has four chambers: the right atrium, the right ventricle, the left atrium and the left ventricle. The right atrium receives the de-oxygenated blood from the other parts of the body through two major veins and pumps blood through the tricuspid valve into the right ventricle situated below. The right ventricle pumps blood to the main pulmonary artery. The pulmonary artery extends to the lungs, here oxygen-poor blood picks up oxygen and is returned to the left atrium via the pulmonary veins and the left atrium pumps this oxygen-rich blood into the left ventricle through the bicuspid valve or mitral valve. The left ventricle pumps oxygen-rich blood through the aortic valve to be distributed throughout the entire body via the aorta, including the heart muscle itself through the coronary arteries. Most researches focus on the left ventricle (LV), whose wall is thicker and more powerful because of the requirement to pump blood throughout the body, as opposed to the right side pumping only through the lungs.

The valves that allow the blood to flow from the atria to the ventricles are called atrioventricular valves, which keep the blood from returning to the atria. The atrioventricular valves can be divided into two types: tricuspid valve and mitral valve. The tricuspid valve is located between the right atrium and the right ventricle and the function of this valve is to open the right atrium when it is in systole, thus forcing any additional deoxygenated blood into the ventricle. The mitral valve is located between the left atrium and the left ventricle, similar to the tricuspid valve, this valve is forced open during atrial systole to allow oxygenated blood from the lungs to enter the left ventricle. Two kinds of semilunar valves,

pulmonary valve and aortic valve, open and close to allow the unidirectional flow of blood out of the heart, while preventing the blood flowing back into the ventricles.

Generally, the cardiac wall consists of three tissues layers: epicardium, myocardium and endocardium as shown in Figure 1.1-b. Epicardium describes the outer layer of heart tissue. The endocardium is the innermost, thin and smooth layer of epithelial tissue. The myocardium is the basic muscle that makes up the heart and the cardiac muscle structure consists of basic units of cardiac muscle cells known as myocytes.

We focus on the structure of the myocardium in this chapter and describe the physical features of myocytes in detail.

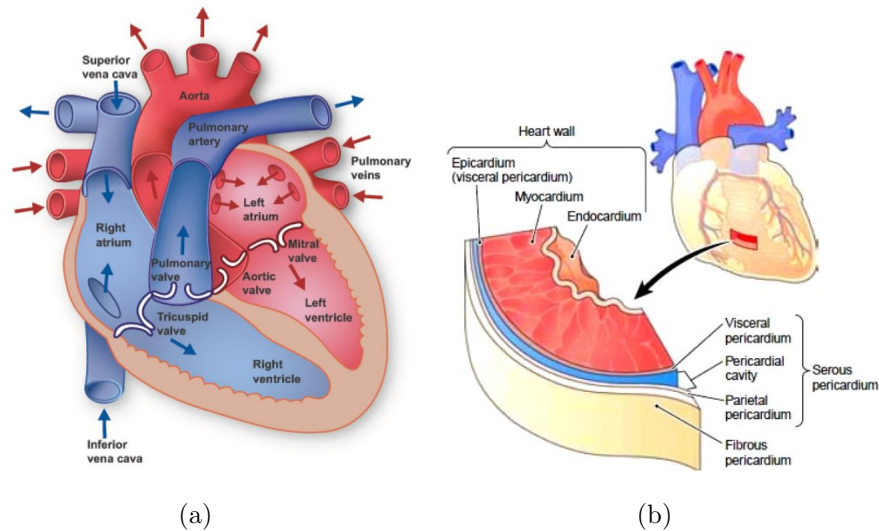


Figure 1.1: (a) Heart anatomical structure at macroscopic scale. <http://www.texasheartinstitute.org/hic/anatomy/anatomy2.cfm>. (b) Heart wall structure. <http://encyclopedia.lubopitko-bg.com/Structure of the Heart.html>.

## 1.2 Structure of the cardiac tissue

### 1.2.1 Cardio-myocyte

Morphometric and tissue engineering studies have shown that the cardiac tissue was composed of cells (myocytes) embedded in a complex mesh-work named extracellular matrix [17], as shown in Figure 1.2.

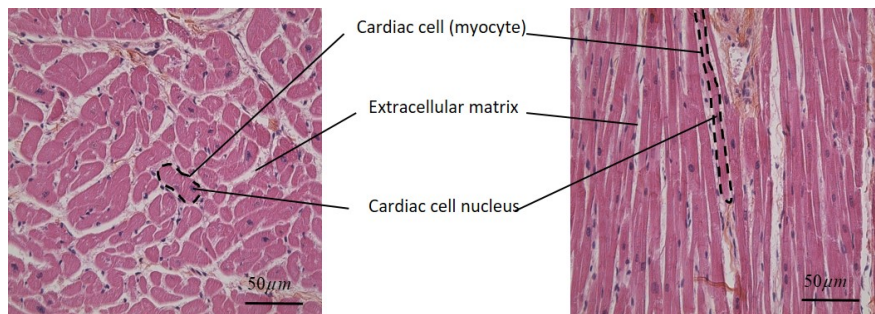


Figure 1.2: Histological cuts of human cardiac tissue ( $\times 20$ ) courtesy of TIMC, CNRS UMR 5525, France. Hematoxylin and Eosin staining. Cut perpendicular to cells (left) and cut parallel to cells (right).

The cardiac muscle cell or myocyte is the main structural component of the myocardium, occupying between 50% and 86% (mean 74%) of the ventricular wall volume under normal circumstances [18]. Cardiomyocytes are branched and connected end-to-end by the intercalated disk, a plasma membrane sarcolemma that acts as a boundary between the cardiomyocyte and extracellular matrix. Cardiomyocytes do not have a regular and consistent shape; they resemble ellipsoid cylinders [19]. The average width has been reported as 10 to 20  $\mu m$  and the average length as 50 to 150  $\mu m$  (Table 1.1).

The permeability of cardio-myocytes, defined as the exchange rate of water molecules through the sarcolemma or intercalated disk, is an important biophysical feature that may provide an indicator for cardiac disease diagnosis. The

permeability of intercalated disks is reported to be  $0.0005\mu m/ms$  [20]. The membrane permeability of biological tissue is around  $0.02\mu m/ms$  [21] (cf. Table 1.1).

High viscosity and macro-molecular hindrance explain the reduced diffusivity of water in the myocyte, which is much lower than the diffusion coefficient of free water at  $37^\circ$  [22, 23, 10, 24, 25]. The diffusivity  $D_{ICS}$  of water in the intracellular space (ICS) approximately equals  $1\mu m^2/ms$  [24]. The homogenizing effect of the collagen fiber in the extracellular space (ECS) is seen as an effective medium with a specific diffusivity of water  $D_{ECS}$  close to  $2.5\mu m^2/ms$  [24](see Table 1.1).

For the sake of simplicity, we will call the cardio-myocytes, "myocytes" in the rest of the text.

Table 1.1: Structural and physical cardiac tissue features.

Techniques	Ref. <sup>1</sup>	Tissue	Cell size <sup>2</sup> $w/d/A$ $\mu m/\mu m/\mu m^2$	Cell length $h$ $\mu m$	Cell volume $V_C$ $\times 10^3\mu m^3$	Cell volume <sup>3</sup> fraction $R_{ICS}$ %	Permeability $P$ $\mu m/ms$	Diffusivity $D$ $\mu m^2/ms$
Optical microscopy	[11]	N.H.	$w$ : 17.5-18.4	59.9-65.8	14.7-18	-	-	-
		P.H.	$w$ : 21.3-22.4	65.1-71.2	25.8-26.2	-	-	-
		N.R.	$w$ : 10-20	50-80	4-26	-	-	-
	[26]	N.R.	$A$ : 220-283	135	29-38	-	-	-
		P. R.	$A$ : 234-283	153-157	36-43	-	-	-
	[27]	N.R.	$w$ : 12.7	-	-	78	-	-
		P. R.	$w$ : 14.1	-	-	73	-	-
[18]	N.H.F.	-	-	1.1-1.3	50-86	-	-	
Electron micrography	[28]	N.R.	$A$ : 140-240	100-131	-	-	-	-
	[29]	N.P.	$w$ : 20-35	100-150	-	-	-	-
Confocal micrography	[30]	N.Rab.	$w$ : $32 \pm 10$	$143 \pm 30$	$30 \pm 7$	-	-	-
		N.F.	$w$ : $31 \pm 5$	$138 \pm 23$	$31 \pm 9$	-	-	-
		N.R.	$w$ : $32 \pm 5$	$142 \pm 15$	$34 \pm 7$	-	-	-
Video micrography	[21]	N.P.	$w$ : 15/23	120	63.5	-	0.02	-
MRI	[24]	N.R.	-	-	-	-	-	$D_{ICS} = 1$ $D_{ECS} = 2.5$
	[25]	N.R.	-	-	-	-	-	1.8-2.5
	[23]	Water	-	-	-	-	-	3.2

1. Normal Human = N.H.; Normal Human Fetus = N.H.F.; Pathological Human = P.H.; Normal Rat = N.R.;

Normal Pig = N.P.; Normal Rabbit = N. Rab; Normal Ferret = N.F.

2.  $w$ : cell width,  $d$ : cell diameter,  $A$ : cell cross section area.

3.  $R_{ICS} = 100 \times$  number of cells in a voxel  $\times$  cell volume / voxel volume.

## 1.2.2 Extra-cellular matrix

The dominant component of the extracellular matrix is collagen fiber. The thickness of the collagen fiber is at the nanoscale, and it is responsible for providing

structural support by transmitting forces, preventing overstretching and rupture, preserving the shape and thickness of the myocardium, and providing both active and passive stability to the myocardium [31].

### 1.2.3 Laminar structure

The micro-structure of cardiac tissue is highly organized and complex. The myocytes are arranged in aggregates of 3 to 5 myocytes thick in the form of a laminar micro-structure [1, 32, 33], also called fibers, as shown in Figure 1.3. Adjacent layers are separated by cleavage planes. These muscle layers run in an approximately radial circumferential direction, especially in the middle wall of the left ventricle (LV). They are represented as transmural sheets twisted to accommodate local muscle fiber orientation. Additionally, there are circumferential and tangential muscle branches between adjacent layers that play an important role in the assembly of such a structure [1]. The laminar organization of the ventricular myocardium permits the rearrangement of muscle fiber bundles when the wall thickness changes [34]. Cleavage planes in the ventricular wall may also affect the propagation of cardiac electrical activation [35].

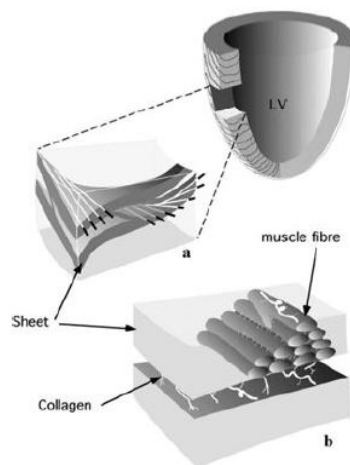


Figure 1.3: Schematic of laminar structure model for cardiac fiber. Image from LeGrice et al. [1].

## 1.2.4 Myocyte transmural orientation change

The myocyte aggregates are coherently aligned with a local average orientation that changes from the epicardium to the endocardium. Fiber orientation is commonly quantified using the helix angle and the transverse angle as shown in Figure 1.4-a. The helix angle is defined as the angle between the fiber long-axis projected onto a plane parallel to the epicardium (tangent plane) and the radial circumferential plane, and the transverse angle is defined as the angle between the fiber long-axis projected onto the radial circumferential plane and the tangent plane. The helix angle of fiber orientation varies from  $-90^\circ$  at the epicardial surface, to  $0^\circ$  at the middle wall, to  $90^\circ$  at the endocardial surface as shown in Figure 1.4-b [3, 36, 37]. Wang et al. [37] showed that the total helix angle in adults ranged from  $70^\circ$  to  $140^\circ$  in different areas of the heart, and the transmural transverse angle changed only slightly (the total range is  $20-40^\circ$  on average). The mean left ventricular (LV) wall thickness ranged from  $3.20 - 3.85\text{mm}$  [37]. The helix angle change rate is based on the ratio between the range of helix angles across the myocardium and the wall thickness, which is about  $20 - 40^\circ/\text{mm}$  [37].

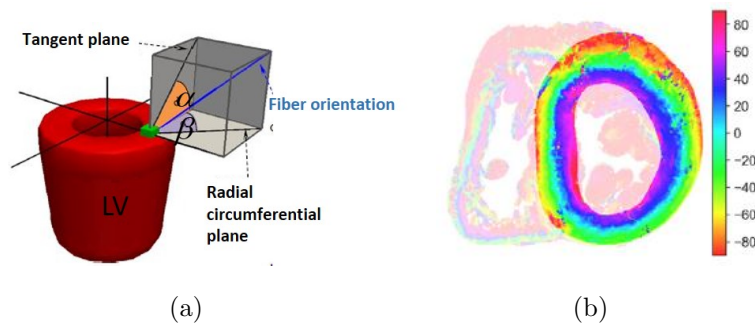


Figure 1.4: (a) Definition of helix angle  $\alpha$  and transverse angle  $\beta$ . Image from Bernus et al. [2]. (b) Helix angle of Myocardial fiber orientation in the short axis plane of the left ventricle for normal 2 months human infant hearts from polarized lighted imaging. Image from Wang et al. [3].

## 1.3 Cardiomyopathy

Cardiomyopathy refers to a group of disorders that directly damage the muscle of the heart walls.

After an acute myocardial infarction (MI), left ventricular (LV) remodeling is characterized by infarct expansion, hypertrophy of non-infarcted myocardium, increased collagen deposition in the infarcted and non-infarcted areas, progressive dilatation, geometric changes in chamber shape, and eventual progression to chronic heart failure [38, 39]. Some studies have shown in rats and a small group of humans that the key cellular change underlying the hypertrophy is progressive myocyte lengthening with no change in myocyte cross-sectional area [40]. A normal left ventricle had an ellipsoidal geometry that alters to a more spherical one following myocardial infarction [13]. The curvature values for different regions of the healthy and infarcted myocardium of rats were reported in [41, 42]. Finally, some works indicated that the change of the collagen (corresponding the change of diffusivity) in extracellular matrix may be linked to the infarcted tissue [14].

Local analysis of diffusion tensors in cardiac muscle had shown that there were larger angular deviations in infarcted regions than in healthy tissues and that these deviations were correlated with the disorder of myocytes [10, 9]. Similarly, the distribution of myocyte diameters was modified in the context of certain cardiac pathologies such as cell hypertrophy [11, 12]. It was shown that, during ischemic injury, the sarcolemma was ruptured, and myocyte membrane permeability increased [16]. Several studies have shown that gap junctions reduced in heart failure and could lead to fatal arrhythmia, leading to a decrease in the permeability of intercalated disks [33, 15].

**In this chapter**, we provided an overview of the structure of the heart at the macroscopic and microscopic levels. We focused more especially on the description of the arrangement patterns of myocytes and their physical characteristics. It has been demonstrated that most cardiomyopathies affect the structural and

physical characteristics of the cardiac tissue, especially in the left ventricle. Therefore the study of the structural and physical characteristics of the cardiac tissue before and after heart disease is of great importance for clinical diagnosis and treatment. The first understanding of cellular morphometry, including myocyte width, cut surface area, length, and volume, come from histological measurements of selected tissue regions [11, 10, 27, 18, 28, 29]. However, these techniques are known to suffer from distortion and misalignment, and while regional structural information was also extracted [43], they do not allow for three-dimensional (3D) reconstruction of fiber structures. To cope with these problems, polarized light imaging (PLI) was proposed to detect 3D fiber orientations of whole fetal human hearts with high spatial resolution ( $0.1 \text{ mm} \times 0.1 \text{ mm} \times 0.5 \text{ mm}$ ) [44]. Furthermore, synchrotron radiation phase-contrast micro-tomography (SR-PCT) was proposed to extract the local orientation of myocytes in the 3D myocardial laminar structure with a very high spatial resolution (micron level) [37, 44]. Compared to dissection and histological methods, these techniques are more objective because they do not involve any human operation during the measurement process. However, these techniques are *ex vivo* and cannot be used for *in vivo* studies of the human heart. More recently, diffusion magnetic resonance imaging (dMRI) has emerged as a new and promising technique for analyzing the 3D fiber structure of the heart [45, 46, 9]. While the spatial resolution of MRI scanners is currently limited, dMRI has the advantage of being able to detect the 3D structure in the *in vivo* heart despite the bulk motion during the heart cycle [47, 32]. In the next chapter, we will focus on the dMRI.

# Chapter 2

## Diffusion magnetic resonance imaging

It has been half a century since the invention of magnetic resonance imaging (MRI) [48]. Magnetic resonance imaging (MRI) is a non-invasive medical imaging technique that allows the interior of the human body to be viewed in detail. Its physical principle is based on the interaction between magnetic fields and atomic nuclei, in particular the protons present in body tissue. In the following paragraphs we will explain very briefly its physical principles, firstly for conventional MRI and then specifically for diffusion MRI.

### 2.1 Conventional MRI

#### 2.1.1 Principle

To understand the principles of MRI and their operational mechanisms, it is necessary to explore three fundamental phenomena: precession, excitation and relaxation.

**Precession** MRI is often used to image the distribution and behavior of water molecules in the body, as water is the most abundant chemical substance in most biological tissues. The protons (hydrogen nuclei  $^1\text{H}$ ) in water molecules have a relatively high magnetic moment, which makes them particularly suitable for detection by magnetic resonance techniques. In an MRI experiment, water protons are placed in a strong magnetic field, denoted as  $B_0$ , causing all the protons to align with the field direction and begin precessing in unison, as illustrated in Figure 2.1-a-b. The frequency of this precession is referred to as the Larmor frequency [49], which is determined by  $\omega_0 = \gamma B_0$  ( $\gamma$  the gyromagnetic ratio of  $^1\text{H}$ ). In the end we see that the sum of all magnetic fields of each proton, which is called magnetization  $M_0$ , pointing in the same direction as the main magnetic field  $B_0$ .  $M_0$  is related to the proton density which we are interested in, thus we intend to see what happens with  $M_0$  during the MRI experiments. However, compared with  $B_0$ ,  $M_0$  is too small to be detected if they share the same direction, thus in order to observe the variation of  $M_0$ , the scientific community came up with a brilliant idea to separate them with a resonance technique.

**Excitation** Then, the protons in the sample are excited by applying a radio frequency (RF) pulse with a frequency equal to the Larmor frequency of  $^1\text{H}$ . This excitation provides the protons with enough energy to move away from their equilibrium position along  $B_0$ . Typically, the RF pulse is applied at a flip angle of  $90^\circ$ , which completely transfers the longitudinal magnetization  $M_0$  into the transverse magnetization  $M$ . When the receiver coil is placed in the transverse plane, the strength of the received signal is proportional to the amount of water in the imaged region, resulting in a proton density image where regions with higher water content appear brighter.

**Relaxation** After the excitation pulse, each proton in the sample precesses at a slightly different speed due to local magnetic field inhomogeneities and random phase variations, which causes signal loss as shown in Figure 2.1-c-d. The signal oscillates at the Larmor frequency ( $\gamma B_0$ ) and decays exponentially, with the rate of decay being described by the T2 relaxation time, as shown in Figure 2.2. The faster the signal decays, the shorter the T2 relaxation. This relaxation time is generally longer in environments where water is less restricted (e.g., lower

viscosity or fewer macromolecules to interact with). Regions with longer T2 relaxation times appear brighter in the resulting image, while regions with shorter T2 relaxation times appear darker. This property can be used to diagnose certain diseases; for example, the formation of edema can significantly slow the T2 relaxation [50, 51].

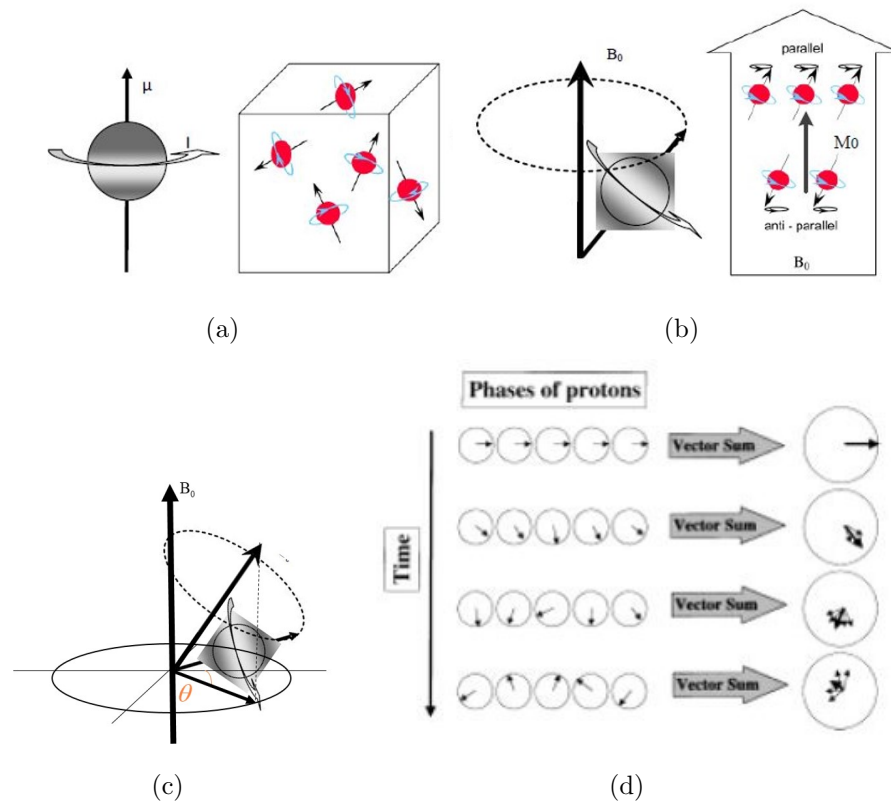


Figure 2.1: (a) Spinning protons. (b) Protons precessing around the field direction when placed in a strong magnetic field. (c) Definition of a proton's phase  $\theta$  as the projection of its precession vector in a transverse plane. (d) Randomized phase of each proton after excitation.

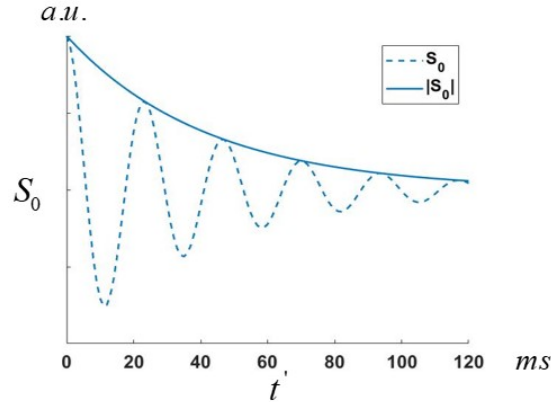


Figure 2.2:  $T_2$  decay: Normalized MRI signal in the transverse plane  $S_0$  that fluctuates with the precession frequency  $\gamma B_0$  and decreases exponentially.

### 2.1.2 Spatial encoding

Now that we understand how MRI works and how MRI signals are acquired, let's delve into the crucial MRI technique called k-space encoding. The MRI signal measured by the RF receive coils possesses its own amplitude, frequency, and phase, which are determined by RF excitation and resonance. The amplitude of the MRI signal is influenced by factors such as proton density, RF pulse frequency and phase, and magnetic field strength. To determine the spatial location of the MRI signal in three dimensions, a specific gradient pulse is applied, introducing spatial variation in the magnetic field. This process incorporates slice selection, phase encoding, and frequency encoding to collectively acquire multi-planar images in MRI. Figure 2.3 illustrates the spatial variation introduced in the magnetic field [52, 53].

**Slice selection:** Slice selection occurs when an RF pulse is activated simultaneously with the application of a magnetic gradient field  $\Delta B$ , allowing the selection of a specific slice along a perpendicular direction. The slice location can be adjusted by changing the frequency of the RF pulse. The slice thickness ( $th$ ) depends on the frequency bandwidth ( $\Delta\omega$ ) of the RF pulse and the strength of

the gradient field  $G_{sl}$  through the slice. It can be expressed as:

$$th = \frac{\Delta\omega}{\gamma G_{sl}} \quad (2.1)$$

**Phase encoding:** Prior to the application of the phase encoding gradient, all spins within the slice have the same frequency and are in phase. However, when the phase encoding gradient is activated, it alters the magnetic field strength, resulting in a change in the precessional frequency of spins along the phase gradient axis. This change in precessional speed leads to a change in the accumulated phase of the spins' magnetic moments along their precession path.

The spatial resolution ( $res_{pe}$ ) and field of view ( $FOV_{pe}$ ) along the phase encoding direction are determined by several factors: the number of phase encoding steps  $n_{pe}$ , the change in gradient strength between two steps ( $\Delta G_{pe}$ ), and the duration of the gradient ( $\delta_{G_{pe}}$ ). This can be expressed as:

$$res_{pe} = \frac{FOV_{pe}}{n_{pe}} = \frac{1}{\gamma \Delta G_{pe} \delta_{G_{pe}} n_{pe}} \quad (2.2)$$

**Frequency encoding:** Similar to phase encoding, the frequency encoding gradient alters the magnetic field strength, resulting in a difference in precessional frequency among spins. This frequency difference is used to encode spatial information. The frequency encoding gradient, also known as the readout gradient, is typically activated during signal reception.

The steepness of the slope of the frequency encoding gradient determines the size of the field of view in the frequency encoding direction ( $FOV_{ro}$ ) and the spatial resolution ( $res_{ro}$ ) in this dimension. The relationship can be expressed as:

$$res_{ro} = \frac{FOV_{ro}}{n_{ro}} = \frac{BW}{\gamma G_{ro} n_{ro}} \quad (2.3)$$

where  $BW$  is the bandwidth of the receive digitizer,  $G_{ro}$  is the strength of the frequency encoding gradient, and  $n_{ro}$  is the number of acquisitions.

Once the MRI signal is encoded, it is organized in a coordinate system called

k-space. After performing a Fourier transform, the MRI data in k-space is transformed into a position-encoded visual image [54]. Specific MRI pulse sequences combine RF pulses and encoding gradients in a predetermined order.

### 2.1.3 MRI Pulse Sequence

MRI pulse sequences allow us to control how the system applies pulses and gradients. The spin echo (SE) sequence is commonly used in MRI experiments due to its versatility and high-quality imaging. It involves a  $90^\circ$  excitation RF pulse followed by one or more  $180^\circ$  rephasing RF pulses to generate a spin echo. Figure 2.3 illustrates the SE sequence.

After the  $90^\circ$  excitation pulse, magnetization is flipped into the transverse plane, but immediately starts to dephase due to T2 relaxation. Some spins slow down while others speed up. A  $180^\circ$  pulse is then applied to flip the spin vectors, causing the previously slower vectors to effectively precess ahead of the previously faster ones. After a further time delay (equal to  $TE/2$ ), a spin echo is formed.

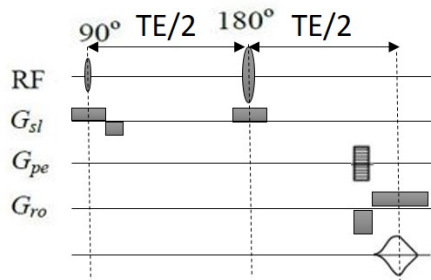


Figure 2.3: Diagram of spin echo (SE) sequence and associated spatial encoding.  $G_{sl}$ ,  $G_{pe}$ , and  $G_{ro}$  represent the gradient fields used for slice selection, phase encoding, and frequency encoding, respectively.

## 2.2 Diffusion MRI

Diffusion MRI is distinguished from conventional MRI by its ability to probe the diffusion of water molecules within biological tissues. Unlike conventional MRI, which primarily provides information about anatomical structures and tissue contrast, diffusion MRI captures the movement of water molecules and provides insights into the microstructural organization of tissues.

### 2.2.1 History and development

The first restricted diffusion acquisition scheme was proposed by Stejskal and Tanner in the form of a unipolar pulsed gradient spin echo sequence (PGSE) [4]. In the 1980s, diffusion imaging was introduced by combining diffusion measurement with MRI. This method makes it possible to track the diffusion of water molecules at the usual spatial resolution of MRI [55, 56]. In the early 1990s, it was discovered that dMRI more accurately reflected early-onset injury induced by acute cerebral ischemia than conventional MRI [57]. This technique also has provided a useful tool to detect acute myocardial infarction [58] and some hypertrophic cardiomyopathy [59, 60, 47].

Most clinical dMRI studies are performed at a low b-value with  $b \leq 1500s/mm^2$  [61]. In that condition, the decay of the dMRI signal conforms to a mono-exponential curve and the diffusion process is usually described by an overall statistical parameter, the “apparent diffusion coefficient” (ADC) [62]. ADC was applied to the heart as a marker after acute myocardial infarction [58, 63]. Lower ADC value regions are consistent with the location of the acute myocardial infarction then ADC increased as a function of time after infarction[58]. Molin et al demonstrated that ADC was markedly higher in regions of infarct than in remote regions [64]. A higher ADC could result from hypertrophy, common in hypertrophic cardiomyopathy, usually associated with an enlarged interstitial space arising from tissue disorganization or fibrosis [59, 60, 47]. Also in the 1990s, a tensor model (diffusion tensor imaging, DTI) was proposed to assess the

anisotropy of diffusion with the assumption of the diffusion displacement profile as a Gaussian distribution [65]. It provides new 3D information about fiber structures, which no other histological or optical imaging techniques were able to image under *in vivo* conditions. Then this concept was applied to prevail local voxel-wise fiber orientation both in healthy hearts [66, 67] and in diseased hearts such as myocardial infarction [68, 58] or hypertrophy [59]. DTI also facilitates the entirely 3D fiber tracking on white matter [50, 69, 70] or myocardial fibers [71, 46, 2]. It was validated with histological data [72, 73, 74]. Cardiac DTI has provided an important and suitable tool to assess the change of myocardial microstructure throughout the cardiac cycle [36, 75, 76, 77, 78]. *In vivo* dMRI of the heart remains a challenge because of the high cost of acquisition due to the very large amplitude of cardiac movements compared with the small movements of water molecules [79]. Heart movements reduce both signal intensity and signal-to-noise ratio (SNR) [80]. Several acquisition sequences have been proposed to compensate for this effect, such as the acceleration motion compensation (AMC) spin echo scheme [81] or the stimulated echo acquisition mode (STEAM) [82, 83]. In addition, DENSE (Displacement Encoding with Stimulated Echo) sequences [121] and the diaphragmatic navigator that precedes them [84] have also been developed for recording heart movement.

For high b-values, the dMRI signal can be decomposed in two components (bi-exponential model), with a fast and a slow diffusion phenomenon; it is suggested that the slow diffusion originates from the restricted diffusion [85]. Besides, the Karger model [86, 87, 88] was proposed to take into account the exchange between two compartments. However, the diffusion of water molecules in biological tissue is complex, and the two-compartment model is questioned [89]. This is one limitation of the conventional K-space (i.e Fourier) approach.

To overcome this limitation, q-space imaging [90] has been proposed to directly reconstruct the probability density function (PDF) of the protons displacements by acquiring a larger set of diffusion data for different values of the diffusion gradient in various angular directions and strength. The PDF can then be integrated radially to yield the orientation distribution function (ODF). Likewise, the shape of the PDF can be described by parameters such as the probability of

zero displacements, the full width at half-maximum, and kurtosis [91]. Due to the cumbersome nature of acquisition, DSI in the heart is currently limited to *ex vivo* samples [71].

## 2.2.2 Principle

A pair of gradient pulse  $G_d$  is set to remark the displacement of water diffusion during them as shown in Figure 2.4-a, the strength (slope) of the gradient, its direction, and the time period can be controlled showing the classic pulsed gradient spin echo (PGSE) sequence with the diffusion duration,  $\Delta$ , and the diffusion gradient pulse with the duration  $\delta$  and strength  $G_d$ . The precession speed is very homogeneous as the strength of the magnetic field is kept as homogeneous as possible across the magnet within one voxel. This homogeneity can be disturbed linearly by using the first pulsed field gradient. If another gradient pulse is subsequently applied with the same direction and time period but of opposite magnitude, such dispersion can be re-phased. However, this refocusing cannot be perfect because the protons moved between this pair of gradient pulses, which leads to the signal loss as shown in Figure 2.4-b. Thus, by applying a pair of gradient pulses after the excitation and before the data acquisition, we can sensitize the image to flow or diffusion of protons.

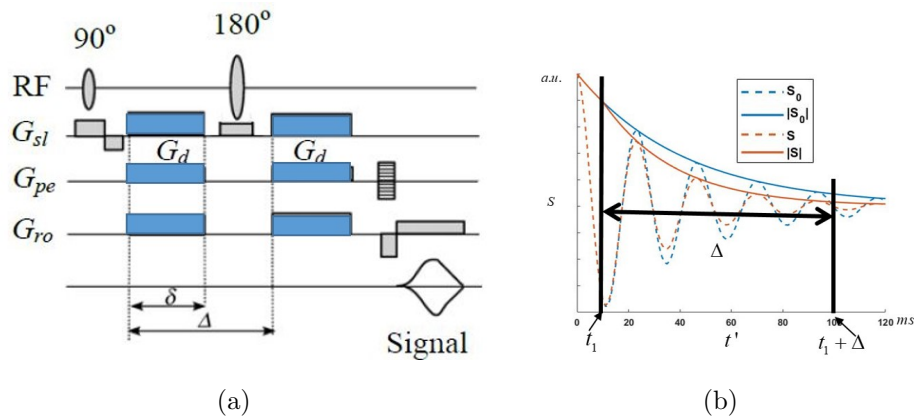


Figure 2.4: (a) Classic MRI Pulsed Gradient Spin-Echo (PGSE) sequence [4] with a diffusion duration  $\Delta$ , and a diffusion gradient pulse of duration  $\delta$  and strength  $G_d$ . (b)  $T_2$  signal decay  $S_0$  vs diffusion weighted signal decay  $S$ .

### 2.2.3 Diffusion encoding schemes used for the *in vivo* heart

The classic spin echo sequence with unipolar gradient pulse has been considered impractical for cardiac imaging due to its sensitivity to bulk motion. The spin echo sequence with bipolar gradient pulse, as proposed by [92] and shown in Figure 2.5, was designed to be insensitive to the first-order motion of the heart. Recent advancements include the acceleration motion compensation (AMC) spin echo scheme, which addresses signal attenuation caused by second-order motion [81]. The asymmetric bipolar diffusion encoding sequence using spin echo was introduced to minimize the effective encoding duration by employing a single bipolar gradient pulse instead of two single gradient pulses [93]. Another acquisition mode, the stimulated echo acquisition mode (STEAM), was developed to mitigate the impact of bulk motion on diffusion measurements. Initially proposed with unipolar diffusion gradients [82], STEAM runs over two cardiac beats, assuming that the myocardium returns to the same position at the same encoding times in consecutive cycles. However, it was found that such diffusion encoding is influenced by cardiac strain, leading to the suggestion of performing measurements in the "sweet spots" of the cardiac cycle with minimized strain effects, typically located in mid-systole and mid-diastole [82]. An alternative stimulated echo method using bipolar gradients was proposed in [83], which is insensitive to myocardial strain and bulk motion and allows diffusion encoding at any time point of the cardiac cycle as if the heart were immobilized during acquisition. Comparisons between these encoding schemes have shown that STEAM is the most effective method for avoiding the effects of myocardial strain and bulk motion [5]. However, it is limited by low scan efficiency as it requires two consecutive heartbeats to be at identical respiratory levels for successful encoding and decoding, which may not always hold true in patients with variable heart rates [93].

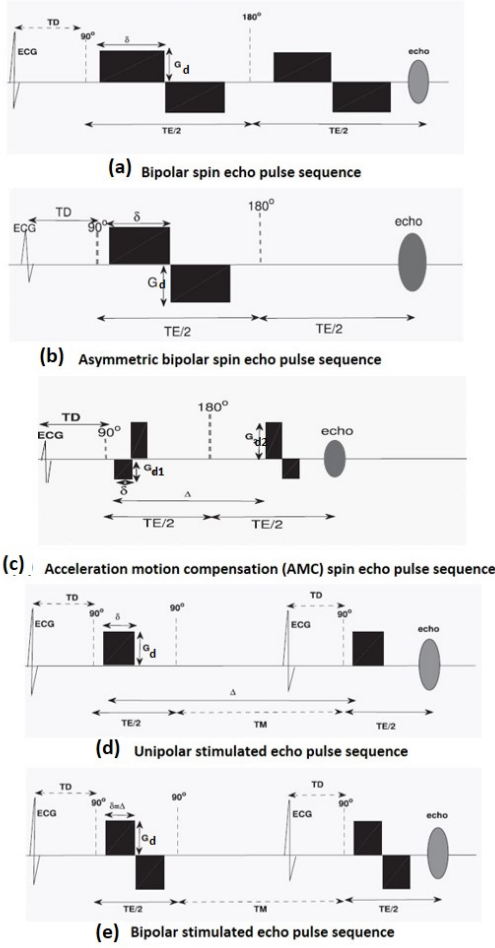


Figure 2.5: Illustration of different diffusion coding schemes applied in cardiac dMRI. Image from Mekkaoui et al. [5].

## 2.2.4 Q-space encoding

Q-space in dMRI is a concept analogous to k-space in conventional MRI and was introduced in the works of Stejskal and Tanner [4], Cory and Callaghan [94], and Callaghan [95]. Q-space is defined as a space used to represent the directions and strengths of diffusion weighting in dMRI. It is characterized by a diffusion wave vector  $\vec{q}$  given by the integral of the gradient waveform  $\vec{G}_d$  over time:

$$\vec{q} = \gamma \int_0^t \vec{G}_d dt \quad (2.4)$$

$\vec{q} = \gamma \vec{G}_d \delta / 2\pi$  for the rectangular gradient pulse as

$$G_d(t) = \begin{cases} G_d & t_1 \leq t \leq t_1 + \delta \\ -G_d & t_1 + \Delta \leq t \leq t_1 + \delta + \Delta \\ 0 & \text{otherwise} \end{cases} \quad (2.5)$$

By applying diffusion gradients with varying strengths and directions, dMRI signal acquisition is performed across q-space. Similar to the Fourier transform used in conventional MRI, a Fourier relationship exists between the dMRI signal and the underlying probability density function  $\bar{P}(\vec{L}, \Delta)$ , as described by Equation 2.6.

$$\bar{P}(\vec{L}, \Delta) = \frac{1}{S_0} \frac{1}{(2\pi)^3} \int_{R^3} |S_\Delta(\vec{q})| e^{-i\vec{q}\vec{L}} d^3\vec{q} \quad (2.6)$$

where  $S_0$  is the signal without diffusion weighting,  $S(\vec{q})$  is the diffusion-weighted signal,  $\vec{L}$  the averaged diffusion displacement of molecules in one voxel.

The probability density function can be further integrated radially to obtain the orientation distribution function (ODF) for a given point on the sphere. ODF is defined as follows:

$$ODF(\vec{k}) = \int_{\vec{q} \perp \vec{k}} P(\vec{q}) d\vec{q} \quad (2.7)$$

## 2.3 DMRI modeling and simulation

A way to understand the relationships between the physical phenomenon of water diffusion through a biological tissue and the diffusion-weighted MRI observation consists in developing adequate models. The mathematical diffusion distribution model, such as DTI model, is a helpful tool to extract the specific water diffusion properties through tissue from the diffusion signal under the assumption of the Gaussian diffusion profile. The phenomenological equations of Bloch-Torrey have been shown to give an excellent analytical description of magnetization resonance and diffusion on the basis of the simple restriction shape[96]. However, for the sake

of realism, the biological tissue turns out to be complex and the water diffusion through the biological tissue no longer conforms to Gaussian distribution so that the adequate analytical description and mathematical model do not exist [97]. In this context, numerical simulation models were developed. Its advantage is the ability to simulate the movement of molecules dynamically in space and time in any tissue structure. Here we focus on the Monte-Carlo (MC) methods. Actually, the Monte-Carlo simulation was validated by the analytical model in the case of simple shaped restriction [98]; And the virtual signal calculated by Monte Carlo simulation was always modeled in a statistical way to extract the specific diffusion property such as the diffusion tensor, mean diffusivity (MD), fraction anisotropy (FA) and main diffusion direction, which are commonly used in clinical dMRI analysis. Next we will demonstrate mathematical diffusion distribution models, Bloch-Torrey analytical models and Monte Carlo simulation models in details.

### 2.3.1 Mathematical models in dMRI

**Apparent diffusion coefficient:** Most studies performed with MRI hardware and limited gradient power ( $b < 1500s/mm^2$ ) report diffusion measurements in terms of a single, global parameter, the apparent diffusion coefficient (ADC), whereby the distribution of molecules' displacements is assumed to the Gaussian distribution, so the signal loss caused by diffusion in one certain direction can be calculated according to the Stejskal-Tanner equation [4],

$$\frac{S}{S_0} = e^{-bADC}, \quad (2.8)$$

where  $b$  is the diffusion weighting factor expressed by

$$b = \gamma^2 \int_0^{TE} \int_0^{t'} (G_d(s)ds)^2 dt'. \quad (2.9)$$

When the PGSE sequence is applied, for rectangular pulses,

$$b = (\gamma\delta G_d)^2 (\Delta - \frac{1}{3}\delta). \quad (2.10)$$

The equation indicates that the higher ADC and  $b$ -value, the more the signal loss. The measuring change in the ADC according to the gradient pulse orientation reflects the diffusion anisotropy and tissue orientation information [99].

**Diffusion tensor model:** In presence of diffusion anisotropy, diffusion can no longer be characterized by a single ADC, but requires other parameters able to fully describe the molecular diffusion along each spatial direction. Thus the concept of diffusion tensor  $\underline{ADC}$  was introduced into dMRI [99] and leading to diffusion tensor imaging (DTI).

$$\underline{ADC} = \begin{bmatrix} ADC_{xx} & ADC_{xy} & ADC_{xz} \\ ADC_{yx} & ADC_{yy} & ADC_{yz} \\ ADC_{zx} & ADC_{zy} & ADC_{zz} \end{bmatrix} \quad (2.11)$$

where ADC along a specific direction  $mn$ , noted  $ADC_{mn}$ , when  $m = n$ ,  $ADC_{xx}, ADC_{yy}, ADC_{zz}$  represent ADC along the x, y and z directions respectively; when  $m \neq n$ , they correspond to the correlation of ADC between pairs of axes. In order to get  $\underline{ADC}$ , at least six noncoplanar directions measurements are necessary. The meaning of this diffusion tensor can be more easily understood using so-called diffusion ellipsoids. The primal, secondary and tertiary eigenvalues represented by  $\lambda_1, \lambda_2$  and  $\lambda_3$  respectively, calculated from the diffusion tensor are three axes of a *diffusion ellipsoid*. This *diffusion ellipsoid* is spherical (three identical eigenvalues) when diffusion occurs in an isotropic environment whereas it is elongated ( $\lambda_1$  is the biggest) in an anisotropic environment. The mean diffusivity (MD) and fraction anisotropy (FA) are given by

$$MD = \lambda_1 + \lambda_2 + \lambda_3$$

$$FA = \sqrt{\frac{3}{2}} \sqrt{\frac{(\lambda_1 - MD)^2 + (\lambda_2 - MD)^2 + (\lambda_3 - MD)^2}{\lambda_1^2 + \lambda_2^2 + \lambda_3^2}} \quad (2.12)$$

Physically,  $MD$  represents the global diffusivity in a given voxel and  $FA$  describes the voxel-wise anisotropic property of diffusion.

**Two-compartments models:** High viscosity and restriction effects have been proposed to explain water diffusion in the intracellular space, while tortuosity effects have been described for water diffusion in the extracellular space. It is important to evaluate the contributions of the intra- and extracellular compartments in order to better understand the overall water diffusion characteristics of a tissue [85].

Bi-exponential models have been suggested to describe the diffusion-weighted MRI (dMRI) signal at high b-values ( $> 1500s/mm^2$ ) as a combination of two components: rapid diffusion in the extracellular compartment and slow restricted diffusion in the intracellular compartment [85, 100]:

$$\frac{S}{S_0} = R_{ICS}e^{-bADC_{ICS}} + (1 - R_{ICS})e^{-bADC_{ECS}} \quad (2.13)$$

Here,  $R_{ICS}$  represents the cellular volume fraction. This model assumes that the exchange between the two compartments is slow during the diffusion measurement time  $t_D$ .

Additionally, the gamma model [101] and the truncated Gaussian model [102] have been proposed to describe non-Gaussian diffusion when the apparent diffusion coefficient (ADC) is assumed to follow a gamma distribution and a truncated Gaussian distribution, respectively.

To account for membrane permeability, Karger developed a two-compartment model with exchange [86]. The Karger model (KM) has been modified to describe non-Gaussian diffusion by considering the effect of restricted diffusion in the intracellular space [87, 88], and it has been adapted to incorporate the effect of different T2 relaxation rates between the compartments [103].

The random permeable barrier model has been proposed, assuming that water molecules are restricted by randomly placed and oriented membranes. This model focuses on the disorder-averaged diffusion propagator using a scattering approach [104, 105]. The input arguments for the model are the radial diffusivity  $((\lambda_2 + \lambda_3)/2)$  and  $\lambda_{1,\Delta>100ms}$ . From this model, microstructure information such as the membrane surface-to-volume ratio  $S/V$  and fiber size can be derived [106]. In this context,  $S$  represents each surface facing the diffusing molecules (twice the surface area of all membranes), and  $V$  corresponds to the voxel volume. The inverse ratio  $V/S$  provides an estimate of the distance between restrictions. The fiber size represents the voxel-wise mean "cell" size, where a cell in this model refers to any region bordered by the membranes.

**Diffusion spectrum imaging model:** Diffusion spectrum imaging (DSI)

enables the direct reconstruction of the probability density function (PDF) of protons by acquiring data with varying diffusion gradient strengths and orientations, as described by Equation 2.6 [90]. The first and second cumulants of the PDF describe the Gaussian component of the distribution, while the fourth order describes the kurtosis or sharpening of the PDF. Further fitting of the PDF to various non-Gaussian models is possible, allowing access to additional parameters. Microstructural information, such as the size of compartment restrictions, can be extracted from diffraction patterns that may be apparent in the signal decay curves plotted against the q-value, as well as from the displacement distribution profile obtained through the Fourier transform of the signal decay [107].

The extraction of the diffusion principal direction is achieved by discretizing the q-space and searching for the maxima of the orientation distribution function (ODF). This step requires significant computational time, and the accuracy of the measurement depends on the quality of spatial sampling and quantification. DSI overcomes the limitations of diffusion tensor imaging (DTI) by its ability to distinguish intra-voxel fiber crossings and fiber kissing, which are crucial steps in fiber tracking.

### 2.3.2 Bloch-Torrey analytical model

**Bloch-Torrey equation:** The macroscopic magnetization vector  $\vec{M}(t) = (M_x(t), M_y(t), M_z(t))$  can be expressed by the Bloch equations [108] as:

$$\frac{d\vec{M}}{dt} = \gamma \vec{M} \times \vec{B} - \begin{bmatrix} M_x/T_2 \\ M_y/T_2 \\ M_z - M_z(0)/T_1 \end{bmatrix} \quad (2.14)$$

where  $M_z(0)$  is the thermal equilibrium magnetization under the constant magnetic field  $B_0$ , which is, by convention, along with the z axis, i.e.  $\vec{B} = (0, 0, B_0)$ . The parameters T1 and T2 are the longitudinal and transverse relaxation times respectively, and  $\gamma$  is the gyromagnetic ratio of  $^1H$ , which equals

$2.68 \times 10^8 \text{rad}/(T \cdot s)$ . Their resolution as

$$\begin{cases} M_{xy}(t) = M_{xy}(0)e^{-i\gamma B_0 t}e^{-t/T_2} \\ M_z(t) = M_z(0)(1 - e^{-t/T_1}) \end{cases} \quad (2.15)$$

As mentioned before, the transverse magnetization  $M_{xy}$  oscillates at the Larmor frequency  $\gamma B_0$  and decays exponentially with the rate  $-1/T_2$  and the longitudinal magnetization  $M_z$  increases exponentially with the rate  $1/T_1$ .

When considering the diffusion, the Bloch-Torrey equation is expressed as [96, 4]

$$\frac{d\vec{M}}{dt} = \gamma\vec{M} \times \vec{B} - \begin{bmatrix} M_x/T_2 \\ M_y/T_2 \\ M_z - M_z(0)/T_1 \end{bmatrix} - \nabla \cdot \vec{v}\vec{M} + \nabla \cdot \underline{ADC}\nabla \cdot \vec{M} \quad (2.16)$$

where  $\vec{B} = \int_0^{TE} \vec{A}(t)\vec{A}^T(t)$  and  $\vec{A}(t) = \gamma \int_0^t \vec{G}(t')dt'$ . We note that  $\vec{v}$  is the velocity of the protons due to the flow of the medium within which they are embedded and  $\underline{ADC}$  is the diffusion tensor.

The normalized diffusion weighted signal for transverse relaxation process (T2 decay) can be expressed as: [4, 95, 90]:

$$S = S_0 \int_{R^3} \bar{P}(\vec{L}, \Delta) e^{i\vec{q}\vec{L}} d^3\vec{L} \quad (2.17)$$

Where the normalized signal without the diffusion weighting  $S_0 = e^{-i(\gamma B_0 + 1/T_2)t}$ ,  $\bar{P}(\vec{L}, \Delta)$  is the probability density of protons' displacements during the diffusion duration  $\Delta$ , the diffusion wave vector  $\vec{q} = \gamma\vec{G}_d\delta/2\pi$ .

An analysis similar to that given earlier reveals that  $\bar{P}(\vec{L}, \Delta)$  will satisfy the equation:

$$\frac{d\bar{P}}{dt} = -\nabla \cdot \vec{v}\bar{P} + \nabla \cdot \underline{ADC}\nabla \cdot \bar{P} \quad (2.18)$$

The solution of Equation 2.18 may be easier than the direct solution of Equation 2.16. even for the pulsed gradient.

**Resolution on impermeable cylinder:** The resolution of Equation 2.18 on simple models of water diffusion involving impermeable planes, cylinders and

spheres have been proposed [95, 109]. In this part, we focus on the impermeable cylinder model. The signal  $S/S_0$  from radial diffusion and axial diffusion (perpendicular and along the cylinder's axis) within an impermeable cylinder of diameter  $d$  and length  $h$  can be modeled by the following analytical equation [110] under the *short gradient pulse (SGP) condition*, i.e.  $\delta \ll 1$ :

$$\frac{S}{S_{0\text{ radial}}} = 4(2\pi qd/2)^2 \times \sum_{p=1}^{\infty} \sum_{m=0}^{\infty} K_{0m} \alpha_{pm}^2 \frac{[J'_m(2\pi qd/2)]^2 \times \exp[-(\alpha_{pm}/(d/2))^2 D_{ICS} \Delta]}{[\alpha_{pm}^2 - (2\pi qd/2)^2]^2 (\alpha_{pm}^2 - m^2)}, \quad (2.19)$$

$$\frac{S}{S_{0\text{ axial}}} = \frac{2[1 - \cos(2\pi qh)]}{(2\pi qh)^2} + 2(2\pi qh)^2 \times \sum_{n=1}^{\infty} \frac{K_{n0} [1 - (-1)^n \cos(2\pi qh)] \times \exp[(-n\pi/h)^2 D_{ICS} \Delta]}{[(n\pi)^2 - (2\pi qh)^2]^2}, \quad (2.20)$$

where  $\alpha_{pm}$  is given by the roots of the Bessel equation  $J'_m(\alpha) = 0$  (with the convention that  $\alpha_{10} = 0$ ). The constant value of  $K_{nm}$  depends on  $m$  and  $n$  according to

$$\begin{cases} K_{nm} = 0 & n = m = 0 \\ K_{nm} = 2 & n = 0, m \neq 0 \quad \text{or} \quad m = 0, n \neq 0 \end{cases} \quad (2.21)$$

When the *long diffusion duration limit* is satisfied, i.e.  $\xi_{\Delta} = D\Delta/(d/2)^2 > 1$ , Equation 2.19 can be simplified according to:

$$\frac{S}{S_{0\text{ radial}}} = \frac{[2J_1(2\pi qd/2)]^2}{(2\pi qd/2)^2}. \quad (2.22)$$

Under *long diffusion duration limit*,  $\frac{S}{S_{0\text{ radial}}}$  only depends on the cylinder diameter,  $d$ , rather than diffusivity  $D_{ICS}$  and diffusion duration  $\Delta$ . As shown in Figure 2.6, we drawn the curves  $\frac{S}{S_0}$  when  $q$  varies. We can observe that  $\frac{S}{S_0}$  decreases when  $q$  increases.

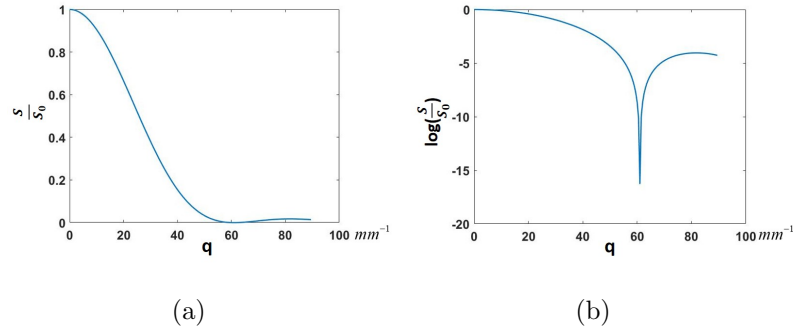


Figure 2.6: Analytical model of dMRI signal for a cylinder with diameter  $d = 20\mu m$  according to Equation 2.22. (a)  $\frac{S}{S_0}$  vs  $q$ . (b)  $\log\frac{S}{S_0}$  vs  $q$ .

The diffusion diffraction minimum pattern of  $\log\frac{S}{S_0}$  occurs when  $q = 61mm^{-1}$  (Figure 2.6-b). It is noted that  $q_{\text{diff}} \times d$  is always equal to 1.22 ( $q_{\text{diff}} = 61mm^{-1}$ ,  $d = 0.2mm$ ) according to [95, 110], where  $q_{\text{diff}}$  holds for q-value when the diffraction minimum pattern occurs.

### 2.3.3 Monte Carlo simulations

The pipeline of a Monte Carlo technique used for our purpose can be divided into 3 steps: (1) build geometrical models of biological tissue based on biological features,(2) create a simulator imitating the movement of water molecules diffusing through these models and (3) observe the simulated displacements of water molecules with a virtual diffusion-MRI imaging sequence and calculate the virtual dMRI signal and diffusion tensor. It thus offers the possibility of studying not only Brownian motion in an arbitrary environment but also all models of interactions between molecules and tissue membranes. Thus, data generated using a Monte Carlo approach makes it possible to study precise biological properties such as cell size, volume fraction, diffusivity, and membrane permeability and provide the ground truth.

The authors simulated diffusion signal distributions for one-dimensional restricted geometries, providing a theoretical basis for later studies [111]. Some

studies validated some mathematical models [112, 113, 106] and analytical models [114, 95, 110, 115] with the Monte Carlo simulations, so offering the ground truth for the study of the diffusion behavior in simple and complex tissues. Some researchers [116, 117, 3] validated the simulation results with real experiments, which showed that the MC simulation could be useful for the quantitative validation of diffusion imaging on clinical MRI devices. Previous works also revealed that some physical and structural features of tissue models could influence the diffusion property and consequently modify the dMRI acquired signals, such as the cell shape [118, 97, 119, 120, 121], cell size [106, 122, 117], membrane permeability [123, 113, 118], diffusivity [113, 117] and cellular volume fraction [106]. Besides, the previous works also provided some significant information about the effect of the diffusion imaging sequence parameters on dMRI signal, including the diffusion duration [107, 124, 125], the duration of gradient pulse [107, 126, 127], the strength of gradient pulse [125], the direction of gradient pulse [107] and b-value [124, 117].

However, these types of simulators are complex systems, which require the adjustment of different parameters and are costly in computing time. Thus, there is a tendency to simplify the geometrical and physical features of the biological tissue models to decrease the simulation burden [97]. Another source of error can come from an inappropriate choice of Monte Carlo parameters. There are attempts at the optimization of the parameters to ensure the accuracy and stability of Monte Carlo results [97, 98]. Besides, the choice of imaging sequence parameters is also a problem in order to ensure a valid estimate of structural information of the observed biological tissue [128, 94, 129].

**In this chapter**, we first presented the basic concepts of the magnetization process of  $^1H$ , including precession, excitation and relaxation. Then we described the spatial encoding technique and gave the common sequence used in conventional MRI. Next, combining the principles of conventional MRI and the process of water diffusion, we detailed the diffusion encoding schemes mandatory to address the challenge of the heart motion. Finally, we illustrated three regularly used dMRI modeling and simulation methods, each method having its own merits and drawbacks. The mathematical models are able to provide versatile parameters

such as MD, FA, PDF or ODF that help to describe the diffusion properties of the water molecules moving within biological tissues and to extract the main diffusion directions. These parameters are very useful for inferring the microstructure of tissues. However, in the absence of ground truth, the microstructure inferred from this kind of model is difficult to assess. The Bloch-Torrey model simulates the process of diffusion imaging, including RF pulse excitation, spatial encoding, diffusion weighting, and signal sampling. It is therefore capable of providing more realistic diffusion images. However, it can only simulate isotropic diffusion and simple restriction boundary. There is a need for further research to extend the analysis to complex anisotropic diffusion cases. The last model involving numerical simulation by using the Monte Carlo method has an obvious advantage in that it provides a perfect ground truth for evaluating the simulation results. Nevertheless, because numerical simulation often requires a long computing time, only simulations in simplified structures were validated until now.

It should be noted that the challenge associated with dMRI simulation by Monte Carlo method is that it requires realistic biological tissue models to mimic the structural and physical characteristics of the tissue; it also requires sufficient samples and updates to guarantee the stability and reliability of the simulation results. The calculation thus becomes more expensive when the virtual tissue model is more realistic and therefore more complex.

# Part II

## Contributions

# Chapter 3

## Virtual cardiac tissue models

In this chapter, we present the four cardiac tissue models of increasing realism that we built. Each cardiac tissue model is divided into two compartments, the intracellular space (ICS), idealized as a collection of cells represented by finite or infinite cylinders, and the extracellular space (ECS), simplified as a collection of interconnected corridors among the cylinders. We consider five physical and structural characteristics of tissue model that can influence the diffusion property, such as the cell size, heterogeneous cell arrangement, membrane permeability, diffusivity and cellular volume fraction.

### 3.1 State of the art

We provide a summary of the physical and structural parameters used in tissue models for simulation studies, which are listed in Table 3.1. In most simulations, myocytes are represented as simplified elongated cylinders. However, some studies have incorporated more realistic cell shapes based on regional histological sections [131]. It should be noted that these models are limited by the relatively small size of the histological sections. Furthermore, certain virtual models have accounted for heterogeneity in the microstructure, specifically in the diameter of myocytes

Table 3.1: Virtual tissue model parameters

References	Cell shape	Cell size $w/d/A$ $\mu\text{m}/\mu\text{m}/\mu\text{m}^2$	Cell length $h$ $\mu\text{m}$	Cell volume $V_C$ $\times 10^3 \mu\text{m}^3$	Cellular fraction $R_{ICS}$ %	Permeability  P $\mu\text{m}/\text{ms}$
<b>Muscle</b>						
[106]	hexa. cylinder <sup>1</sup>	$w:28.5-64.5$	-	-	55-95	0
[122]	cylinder	$d:37\pm 15$ <sup>3</sup>	infinite	-	60-70	0-0.05
<b>Heart</b>						
[123]	hexa. cylinder	$w: 15 \times 25$	90	33.7	66	0-0.1
[130]	cylinder	$d: 10-50$	50-100	3.9-19.6	20	0
[117]	cuboid	$A: 100-300$	90-150	9-45	75-90	0
[131]	polyhedron	$A: 14-320$	114-126	16.0-40.3	60-84	0
[132]	cylinder	$d: 10-40$	infinite	-	100	0
[133]	cylinder	$A : 120 \pm 40$ <sup>4</sup>	-	-	-	0-1
[3]	cylinder	$d: 6 - 10 \pm 1$ <sup>5</sup>	40-100	1.1-7.8	45-85	0
<b>Brain</b>						
[113]	cylinder	$d:1.25$	infinite	-	50	0.0016-4
[118]	cylinder	$d:8-10$	infinite	-	50	0.05-0.1
[97]	cylinder	$d:1.8\pm 0.9$ <sup>3</sup>	infinite	-	60	0
[98]	cylinder	$d:3.2\pm 2$ <sup>3</sup>	infinite	-	66 - 76	0
[119]	cylinder	$d:10$	infinite	-	-	0
[120]	un. cylinder <sup>2</sup>	$d:1-5$	infinite	-	-	0
[134]	un. cylinder <sup>2</sup>	$d:2\pm 0.4$ <sup>3</sup>	infinite	-	20	0

1. Hexagonal cylinder. 2. Undulation cylinder. 3. The cell diameters conform to the gamma distribution, the value is mean $\pm$ standard deviation. 4. The cell cross section areas conform to the normal distribution, the value is mean $\pm$ standard deviation. 5. The cell diameters conform to the log-normal distribution, the value is mean $\pm$ standard deviation.

[130, 3, 131, 133, 135] and their orientation [117, 3, 131, 135], in order to capture the statistics observed in histological data. The values of cell size, permeability, and cellular volume fraction have been derived from histological data and physical measurements, as detailed in Table 1.1. In our simulations, we consider all the aforementioned structural and physical features, which will be further discussed and demonstrated in the following sections.

## 3.2 Implementation

### 3.2.1 One myocyte model

To represent a unique myocyte in our simulations, we employed a simplified cylindrical model, as illustrated in Figure 3.1. This choice of model offers several advantages, including reduced computational complexity and the ability to control the size and orientation of the cell. The cylindrical approximation is suitable for

most regions of the cardiac wall, where the length of a myocyte is approximately 10 times its diameter. To define the three-dimensional orientation of the cell, we introduced the concepts of elevation angle  $\alpha$  and azimuth angle  $\beta$ . These angles provide a convenient way to describe the orientation of the cylindrical cell within the tissue model and are depicted in Figure 3.1.

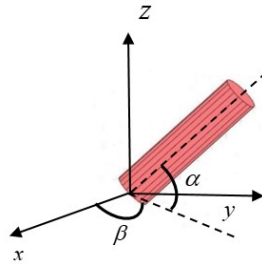


Figure 3.1: Simulated cylindrical cell (myocyte). Definition of elevation angle  $\alpha$  and azimuth angle  $\beta$ .

By using this simplified cylindrical model, we are able to effectively capture a general approximation of the characteristics of the cells while maintaining computational efficiency.

### 3.2.2 Multi-cell models

In our study, we developed four models (Models I, II, III, and IV) to simulate cardiac tissue, each representing different levels of realism. Figure 3.2 illustrates these models.

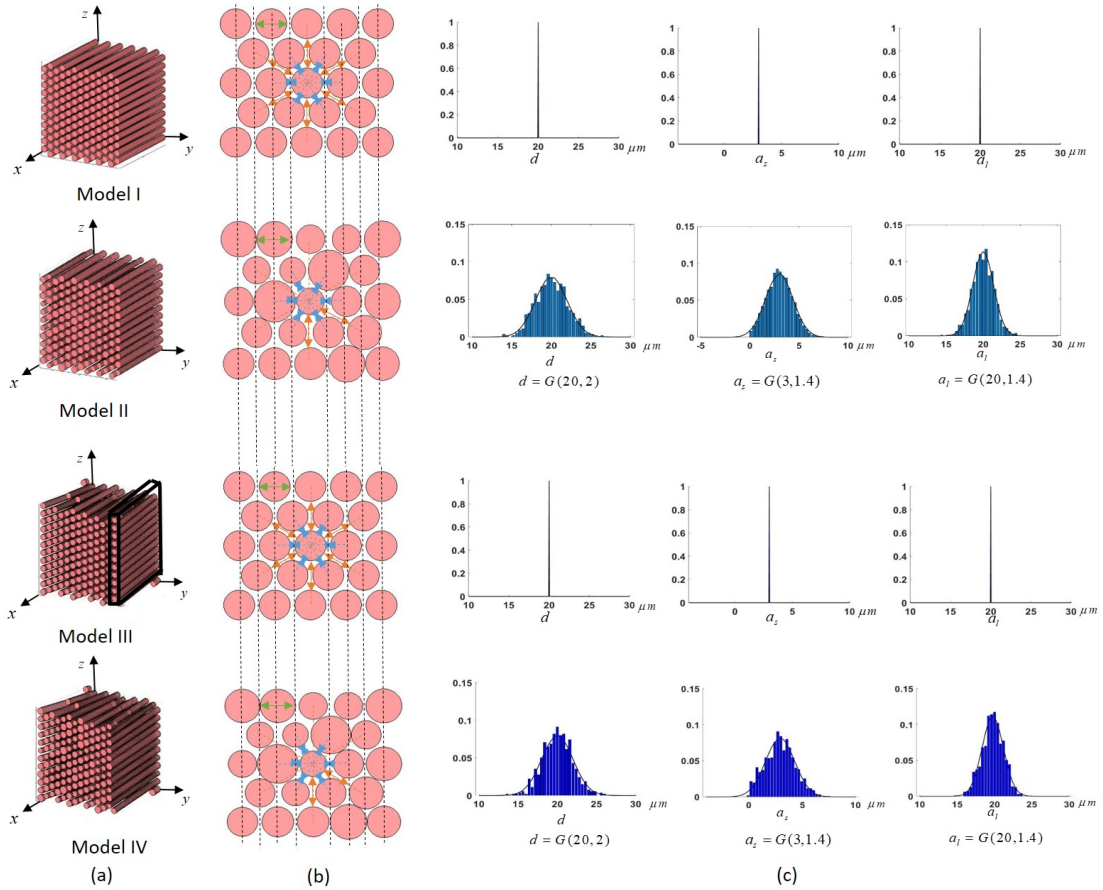


Figure 3.2: Simulated models of cardiac tissues: (a) Model I: periodic arrangement of parallel identical cells. Model II: parallel cells with heterogeneous diameters. Model III: identical cells with heterogeneous orientations. Model IV: cells with heterogeneous diameters and orientations. The cubic box represents one layer of cells. (b) Cross-sectional views, showing spatial restrictions:  $d$  (green arrow) in the intracellular space (ICS);  $a_l$  (red arrow) and  $a_s$  (blue arrow) in the extracellular space (ECS). (c) Distribution of  $d$ ,  $a_l$ , and  $a_s$  within a voxel of size  $Vb = 500 \times 500 \times 500 \mu m^3$ .

In **Model I**, we used a periodic arrangement of parallel identical cells, represented as cylinders. This simplified model allowed us to control the size and orientation of the cells.

**Model II** introduced heterogeneity by varying the diameters of the cells. We

modeled the cell diameter distribution using a gamma distribution with mean diameter  $\mu_d$  and standard deviation  $\sigma_d$  [97, 98]. Specifically, we simulated two scenarios with different mean diameters:  $\mu_d = 20\mu m$  and  $\mu_d = 10\mu m$ , both with a constant ratio  $\frac{\sigma_d}{\mu_d} = 0.1$  based on histological knowledge [11].

**Model III** aimed to mimic the continuous change in cell orientation observed in cardiac tissue. We achieved this by gradually varying the elevation angle  $\alpha$  of the cells from one layer to the next, while keeping the azimuth angle  $\beta$  constant. The rate of change in  $\alpha$  depended on the mean cell diameter:  $0.5^\circ$  per layer for  $\mu_d = 10\mu m$  and  $1^\circ$  per layer for  $\mu_d = 20\mu m$ .

Finally, **Model IV** combined the heterogeneity in cell diameters from Model II with the continuous change in cell orientations from Model III, providing a more realistic representation of cardiac tissue.

By considering both intracellular and extracellular spaces and incorporating heterogeneous information from histological data, these four models capture the statistical variability observed in cardiac tissue structure and provided a comprehensive understanding of its complex organization.

### 3.2.3 Global tissue model

To create the global tissue model, as depicted in Figure 3.3, we simulated the heart wall from endocardium to epicardium, considering the histologically observed left ventricular wall thickness. The model encompassed a size of  $2500 \times 3500 \times 500\mu m^3$ . The change in cell orientation along the  $y$  axis followed the histological data, with a rate of  $50^\circ/mm$  and a range of  $-87^\circ$  to  $87^\circ$  [97, 98], in agreement with Section 1.2.4.

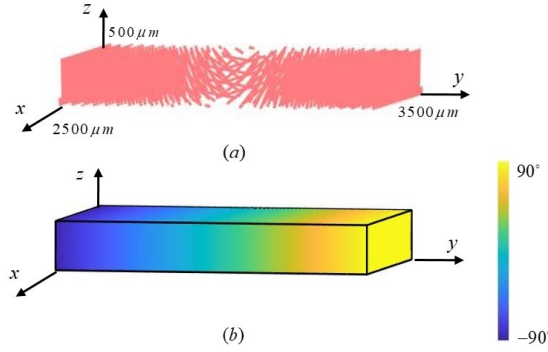


Figure 3.3: (a) Global tissue model of size  $2500 \times 3500 \times 500 \mu m^3$ . (b) Elevation angle  $\alpha$  in Models III and IV:  $\alpha$  varies only along the y axis while the azimuth angle  $\beta$  remains equal to 0.

### Algorithm for spatial arrangement

The algorithm used for placing the cylinders in the models proceeded as follows:

1. Firstly, we built a homogeneous model by placing  $M$  cells (cylinders) on a regular 2D grid. The distances  $a_l$  and  $a_s$  represent respectively the widest and narrowest spatial restriction of ECS.  $a_s$  was calculated as the distance between the walls of neighboring cells along the line of center locations, while  $a_l$  was calculated as the distance between the walls of non-neighboring cylinders along the line of center locations, as shown in Figure 3.2-b. The values of  $a_l$  and  $a_s$  are determined by the choice of  $d$  and  $R_{ICS}$ .
2. Next, we also choose  $M$  cylinders for the heterogeneous model and fixed their locations on the same 2D grid.
3. The  $M$  diameters were drawn from a normal distribution with the desired  $\mu_d$  and  $\sigma_d$ .
4. We sorted the diameters in descending order starting from the largest diameter and progressively placed all cylinders on the grid as follows: a) Choose a random position to place a cylinder; b) If the cylinder overlaps with any other already in place, discard it and return to step (a); c) Place a new cylinder until the  $M^{th}$  cylinders are placed.

## Physical characteristics of the cardiac tissue model

Regarding the physical characteristics of the cardiac tissue model, we considered diffusivity  $D$ , membrane permeability  $P$ , cellular volume fraction  $R_{ICS}$ , and diffusivity coefficients  $D_{ICS}$  and  $D_{ECS}$  for ICS and ECS, respectively. These parameters were set based on histological data (Table 1.1), with  $\mu_d = 10\mu m$  or  $\mu_d = 20\mu m$ ,  $R_{ICS} = 70\%$ ,  $D_{ICS} = 1\mu m^2/ms$ ,  $D_{ECS} = 2.5\mu m^2/ms$ , and two situations for permeability: one with impermeable compartments ICS and ECS separately and another with a permeable environment ( $P = 0.02\mu m/ms$ ).

## 3.3 Conclusion

**In this contribution**, we set out to create realistic models of cardiac tissue in order to model its microstructural properties and diffusion characteristics. We developed four models (models I, II, III and IV) with increasing levels of complexity, taking into account factors such as microstructural characteristics (cell arrangement, heterogeneity of cell diameters and variation in cell orientations) and physical characteristics (diffusivity, permeability and cell volume fraction). These models will be used in the next two chapters to better understand how diffusion MRI can measure the spatial restrictions and microstructural characteristics of tissue by simulating the diffusion behaviour of water molecules inside.

The realism of tissue models could be further improved by considering in particular information provided by high spatial resolution imaging techniques such as polarized illumination imaging (PLI) [3] or even morphological characteristics extracted from histological images [131, 121]. Local analysis of diffusion tensors in cardiac muscle has shown that there are larger angular deviations in infarcted regions than in healthy tissues and that these deviations are correlated with the disorder of cardiomyocytes [10, 9]. Similarly, the distribution of myocyte diameters is modified in the context of certain cardiac pathologies such as cell hypertrophy. [11, 12]. These pathological variations of cardiac cells as well as their organizations should be taken into account in future MC simulations.

# Chapter 4

## Water molecule diffusion simulation in cardiac tissue model

In this chapter, we present the application of the Monte Carlo strategy to simulate water diffusion molecules within a virtual cardiac tissue model. Our objective is to verify four critical conditions related to the Monte Carlo parameters: the number of simulated molecules  $N$ , the number of simulation steps  $K$ , and the voxel size  $V$  of the tissue model. These conditions are essential to ensure the accuracy and stability of our Monte Carlo simulation.

### 4.1 State of the art

The simulation of water molecule diffusion using the Monte Carlo method can be a time-consuming process. However, selecting inappropriate Monte Carlo parameters can lead to errors in the simulation results. Several studies have focused on optimizing these parameters, and Table 4.1 provides an overview of the relevant Monte Carlo simulation parameters employed in these studies.

Table 4.1: Virtual water diffusion : Monte Carlo simulation parameters

Ref.	Diffusivity $D_{ICS}/D_{ECS}$ $\mu m^2/ms$	Update duration $\tau$ $ms$	Update length $l$ $\mu m$	Update length ratio $l/d$	Updates number $K$	Molecules number $N$
<b>Muscle</b>						
[106]	1.8/2.2	-	-	-	-	$2 \times 10^5$
[122]	2/2	< 0.002	-	< 0.25	$10^5$	$10^4$
<b>Heart</b>						
[123]	1/1	0.17	1	< 0.07	300	1000
[130]	1/1	0.17	1	< 0.10	350	$4 \times 10^7$
[117]	0.5-2.5/0.5-2.5	0.002	< 0.17	< 0.03	$(3.5 - 20) \times 10^3$	$(1 - 125) \times 10^5$
[131]	1-2/2-3	0.1	< 1.4	-	1000	$10^4$
[136]	2-3/-	0.1-0.4	< 2.7	< 0.15	1000	$10^6$
[133]	0.5/2	0.01-1.5	< 4.3	-	-	$10^6$
[3]	0.5-3/0.5-3	0.005	0.3	< 0.075	5000	$3 \times 10^4$
<b>Brain</b>						
[113]	0.5-1/1-2	< 0.001	-	< 0.05	-	$4 \times 10^5$
[118]	2/2	0.1	1.1	< 0.14	10-1000	$10^5$
[97]	0.6/0.6	0.003-0.009	< 0.18	< 0.1	5000	$5 \times 10^3$
[98]	2/2	0.1	1.1	0.34	1000	$10^5$
[119]	2/2	0.01	0.35	0.035	7000	$10^4$
[120]	2/2	$9 \times 10^{-5}$	0.03	< 0.03	$300 - 10^6$	$(4 - 20) \times 10^4$
[134]	-/2	0.01	0.35	0.17	$10^4$	$10^6$

For instance, Landmans et al. [118] investigated the displacement distribution of water molecules for various values of  $\tau$  and  $\Delta$  in the case of free diffusion. Their results demonstrated that  $\Delta/\tau \geq 10$  is required to ensure the accuracy of the simulation.

Hall et al. [98] proposed a robust Monte Carlo simulator to ensure accurate simulations within a restricted environment, specifically a brain tissue model. They analyzed the simulation error of the Monte Carlo-simulated signal while varying the number of particles  $N$  and updates  $K$  for a fixed  $\Delta$ . These simulations were performed considering an impermeable environment composed of parallel cylinder-shaped cells. As a reference, they utilized an analytical model that approximated the tissue as a two-compartment system. Their findings revealed that  $K \geq 1000$  (corresponding to  $l/d \leq 0.34$ , as listed in Table 4.1) and  $N \geq 10^5$  are necessary for accurate simulations. Rafael-Patino et al. [97] employed a similar methodology but did not rely on an analytical model for the extracellular compartment. Instead, they used a high number of particles and updates as the reference for their Monte Carlo simulations, concluding that  $K = 5000$  (corresponding to  $l/d < 0.1$ ) and  $N \geq 5 \times 10^3$  are required.

Furthermore, Landmans et al. [118] investigated the impact of the duration  $\tau$  in the case of a permeable environment by comparing the displacement distribution of water molecules. Their results indicated that smaller  $\tau$  values were necessary for shorter  $\Delta$ , and  $l/d \leq 0.14$  was required for brain tissue with low permeability ( $P = 0.05 - 0.1 \mu m/ms$ ). Additionally, Fieremans et al. [113] recommended  $l/d < 0.05$  for brain tissue with high permeability ( $P = 4 \mu m/ms$ ).

To ensure the stability of the Monte Carlo simulation, Hall et al. [137] studied the mean cell diameter and mean volume fraction for different simulation scales. They demonstrated that the variation in these parameters around the mean decreases with increasing simulation scale size. For instance, in the case of a brain tissue model with a mean cell diameter of  $0.63 \mu m$  and a standard deviation of  $0.26 \mu m$ , employing 1000 or more cylinders resulted in a consistent mean volume fraction of around 0.7, and the variation around the mean decreased with an increasing number of cylinders. Similarly, Rafael-Patino et al. [97] investigated the radial anisotropy of the diffusion magnetic resonance imaging (dMRI) signal for different simulation scales. They demonstrated that a sufficiently large simulation scale, achieved by sampling a significant number of cylinders (e.g., 10,000 cylinders for a brain tissue model with a mean cell diameter of  $1.8 \mu m$  and a standard deviation of  $0.9 \mu m$ ), was necessary for the simulated signal to converge.

It is worth noting that most studies have optimized the Monte Carlo parameters within the brain tissue model. However, our focus will now shift to the cardiac tissue model, where we will explore the applicability of these parameters.

## 4.2 Monte Carlo strategy

The Monte Carlo strategy is employed to replicate the Brownian motion of water molecules within our simulation. It involves simulating the movement of a specified number,  $N$ , of molecules by performing  $K$  updates. This approach effectively emulates the continuous diffusion process of water over a diffusion duration,

$\Delta$ . Each individual displacement, or step, taken by a molecule has a duration  $\tau = \Delta/K$  and is randomly assigned a spatial orientation.

The Monte Carlo strategy for simulating water diffusion involves several key steps:

1. **Generation of a uniform 3D direction of diffusion:** In the simulation, each water molecule is assigned a uniform three-dimensional direction of diffusion, representing its random spatial orientation during displacement.
2. **Distribution of the length of each step:** The length of each step taken by a water molecule is determined using a distribution that captures the statistical characteristics of water diffusion, accommodating variations in step lengths and reflecting the stochastic nature of molecular motion.
3. **Transmission probability:** A transmission probability is assigned to each step of a molecule, assessing its ability to cross the membrane between tissue compartments, accounting for permeability and impacting diffusion efficiency.
4. **Property of simulated diffusion:** The Monte Carlo simulation generates a representation of water diffusion in the virtual tissue model, exhibiting properties including displacement patterns, spatial distribution, and diffusion rates, allowing for observation, analysis, and insights into the diffusion behavior within the cardiac tissue model.

Through these steps, the Monte Carlo strategy enables the modeling and analysis of water diffusion in the virtual cardiac tissue, offering valuable insights into the complex behavior of diffusion processes.

**Generation of a uniform 3D direction of diffusion:** In order to create a uniform 3D direction of diffusion in a unit sphere, Marsaglia et al. [138] devised a method involving the selection of  $x_1$  and  $x_2$  from independent uniform distributions between  $(-1, 1)$ , while rejecting points where  $x_1^2 + x_2^2 \geq 1$ . The remaining points can be transformed into 3D coordinates as follows:

$$\begin{cases} x = 2x_1\sqrt{1 - x_1^2 - x_2^2} \\ y = 2x_2\sqrt{1 - x_1^2 - x_2^2} \\ z = 1 - 2(x_1^2 + x_2^2) \end{cases} \quad (4.1)$$

When generating the 3D direction of diffusion by using uniform azimuth and elevation angles, it results in a concentration of directions along the z-axis, as depicted in Figure 4.1-a-b-c. By employing Marsaglia's method, the distributions of the x, y, and z-axis projections become uniform, and the corresponding distribution of the calculated elevation angle ( $\alpha$ ) exhibits fewer concentrations around  $\pm\pi/2$  (z-axis), as illustrated in Figure 4.1-d-e-f.

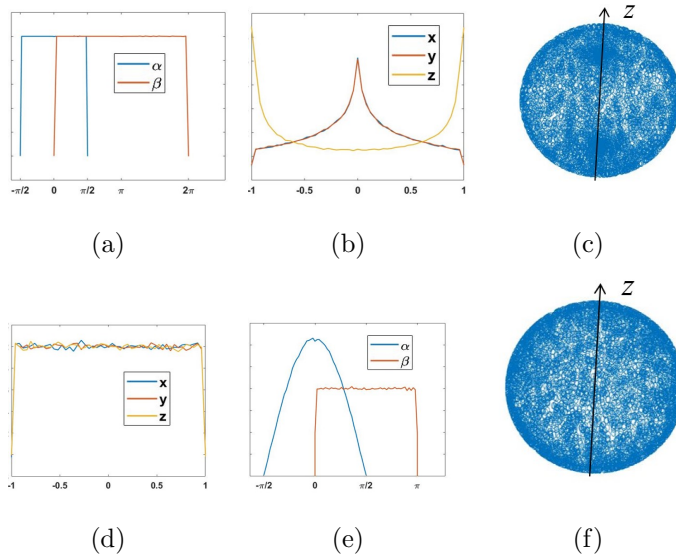


Figure 4.1: Generation of 3D direction of diffusion using two methods: Method 1 - (a) Elevation and azimuth angles  $\alpha$  and  $\beta$ , (b) Uniformly generated  $\alpha$  and  $\beta$ , (c) Distribution of x, y, and z-axis projections, and (d) Corresponding points generated on a sphere; Method 2 - (e) Uniformly generated x, y, z-axis projections, (f) Distribution of  $\alpha$  and  $\beta$ , and (g) Corresponding points generated on a sphere.

**Distribution of the length of each step:** The length  $l$  of each step is determined by the equation:

$$l = \sqrt{6D\tau}p(l) \quad (4.2)$$

where  $p(l)$  follows either a fixed distribution [123, 98] or a Gaussian distribution [117]. In our implementation, we opted for a fixed-length step, represented by  $p(l) \equiv 1$  [123, 98], as it is easier to generate and results in improved execution speed. Furthermore, studies have shown that using a fixed-length step reduces fluctuations in the mean-squared displacement of molecules over time, leading to improved convergence in the model [98].

**Transmission probability:** Molecules within the intracellular space (ICS) undergo diffusion inside virtual cells using steps of length  $l_{ICS}$  and diffusing with a diffusivity of  $D_{ICS}$ . Conversely, molecules in the extracellular space (ECS) diffuse outside the virtual cells using steps of length  $l_{ECS}$  and a diffusivity of  $D_{ECS}$ . When a simulated molecule encounters the virtual cell membrane, it either elastically reflects or crosses the membrane based on the membrane's permeability value, denoted as  $P$ . The transmission probabilities across the membrane from ICS to ECS and from ECS to ICS are given by  $p_{ICS-ECS}$  and  $p_{ECS-ICS}$ , respectively, and can be calculated using the membrane's permeability value  $P$  [118]:

$$\begin{cases} p_{ICS-ECS} = P \frac{4\tau}{l_{ICS}} \\ p_{ECS-ICS} = P \frac{4\tau}{l_{ECS}} \end{cases} \quad (4.3)$$

It is important to note that  $p_{ICS-ECS} \neq p_{ECS-ICS}$  when  $l_{ICS} \neq l_{ECS}$ , indicating a discrepancy between the diffusivities  $D_{ICS}$  and  $D_{ECS}$  as described by Equation 4.3. As mentioned in Table 1.1,  $D_{ICS} < D_{ECS}$ , resulting in  $p_{ICS-ECS} > p_{ECS-ICS}$ . This difference ensures that the equilibrium distribution can be uniform with  $\Delta$ , meaning the ratio of molecule density between ICS and ECS can be 1, as depicted in Figure 4.2. Otherwise, without this disparity, molecules would accumulate in ICS (a region with lower diffusivity) due to longer mean residence times.

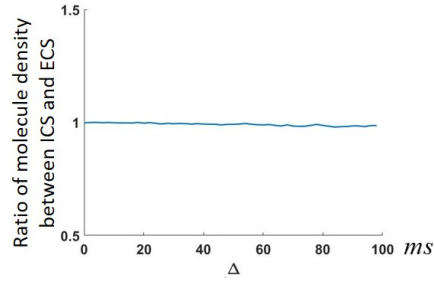


Figure 4.2: Variation of the molecule density ratio between ICS and ECS with respect to  $\Delta$  during Monte Carlo simulation of water diffusion in a permeable environment using Model IV with a mean cell diameter of  $\mu_d = 20\mu m$ . The Monte Carlo parameters employed are  $N = 10^5$  and  $\tau = 0.01ms$ .

**Property of simulated diffusion:** Water diffusion in biological tissues deviates from a Gaussian distribution and exhibits slower rates compared to free diffusion. To address this, the apparent diffusion coefficient (ADC) reflects the interaction between water molecules and the restrictions imposed by tissue microstructures, making it highly sensitive to physiological conditions encountered in tissues.

The apparent time-dependent diffusion coefficient along a specific direction  $mn$ , noted  $ADC_{mn}$  from Equation 2.11, is calculated according to:

$$ADC_{mn}(\Delta) = \frac{1}{2\Delta} p(L_m(\Delta)) L_m(\Delta) \times p(L_n(\Delta)) L_n(\Delta), \quad (4.4)$$

where  $p(L_m(\Delta))$  is the probability associated with the displacement of molecules along  $m$  direction during diffusion duration  $\Delta$ ,  $L_m(\Delta)$ . The probability  $p(L_m(\Delta))$  is a Gaussian distribution in the case of free diffusion. The theoretical value  $ADC_{mn}^t(\Delta)$  can be approximated by  $N$  simulated molecules from Monte-Carlo simulation according to the following expression [112]:

$$ADC_{mn}^t(\Delta) = \frac{1}{2\Delta} \lim_{N \rightarrow \infty} \frac{1}{N} \sum_{i=1}^N L_{i,m}(\Delta) \lim_{N \rightarrow \infty} \frac{1}{N} \sum_{i=1}^N L_{i,n}(\Delta), \quad (4.5)$$

where  $L_{i,m}(\Delta)$  holds for the displacement of molecule  $i$  along  $m$  direction during  $\Delta$ .

The diffusion tensor computed from Equation 2.11 gives us the theoretical eigenvalues  $\lambda^t$  as well as  $MD^t$  and  $FA^t$  (cf. from Equation 2.12).

### 4.2.1 Conditions on the Monte Carlo parameters

To be valid and lead to robust results, Monte Carlo-type methods simulating the diffusion of water through a cell model and a tissue model (multi-cell model) must meet three fundamental conditions:

- *Condition K.* According to Einstein’s theory [139], *the duration  $\tau$  of each update must be very small compared to the whole diffusion duration  $\Delta$*  in order to ensure the independence of every update, i.e. the number of updates  $K = \Delta/\tau$  must be large enough.
- *Condition  $l/s$ .* This condition concerns *the ratio between the length of the path  $l$  traveled by a water molecule during an update  $\tau$  and the spatial restriction  $s$  of a compartment in the most restricted diffusion direction,  $l/s \ll 1$* , where  $s = d$  in ICS [114, 113] and  $s = a_l$  in ECS.
- *Condition N.* This condition concerns the *number of molecules  $N$* . The simulation process must consider a large number of water molecules  $N$  to ensure the accuracy and realism of the results in terms of biology [98, 97].

Furthermore, when simulating water molecules diffusing through a tissue model, an additional condition should be met:

- *Condition V.* This condition concerns *the scale of the MC simulation  $V$* . According to [137], in the case of tissue models with heterogeneous cells diameters, a too small simulation scale leads to an unstable distribution of

statistical moments associated with the cell diameter as well as with the cellular volume fraction and diffusion characteristics. Thus, a sufficiently large simulation scale associated to a sufficiently large number of cells is necessary to build a stable diffusion environment.

## 4.2.2 Specific implementation for tissue model

The practical implementation of the Monte Carlo method is crucial to ensure the reliability and accuracy of the obtained results. In our case, the simulation focuses on the diffusion of water molecules within a localized, finite-dimensional region of interest, represented by a voxel. This approach allows for a detailed analysis of water diffusion dynamics within the tissue model.

In the context of multi-cell models, an additional condition, known as Condition V, comes into play. Condition V emphasizes the significance of the simulation scale in achieving stable diffusion environments, particularly when considering tissue models with heterogeneous cell diameters. Insufficient simulation scale can lead to unstable distributions of statistical moments associated with cell diameter, cellular volume fraction, and diffusion characteristics. Consequently, it becomes crucial to employ a simulation scale that is sufficiently large, coupled with an ample number of cells, to ensure the stability and reliability of the diffusion environment within the multi-cell model.

- *Voxel sizes:* For our study, we used three different voxel sizes: small  $V_s = 100 \times 100 \times 100 \mu m^3$ , medium  $V_m = 250 \times 250 \times 250 \mu m^3$ , and large  $V_b = 500 \times 500 \times 500 \mu m^3$  respectively (Figure 4.3).
- *Extended Voxels:* Whatever the size of the voxel, it is necessary to cope with the edge effects when simulating the diffusion of water molecules. Different approaches have been considered in the literature, as depicted in Figure 4.4.

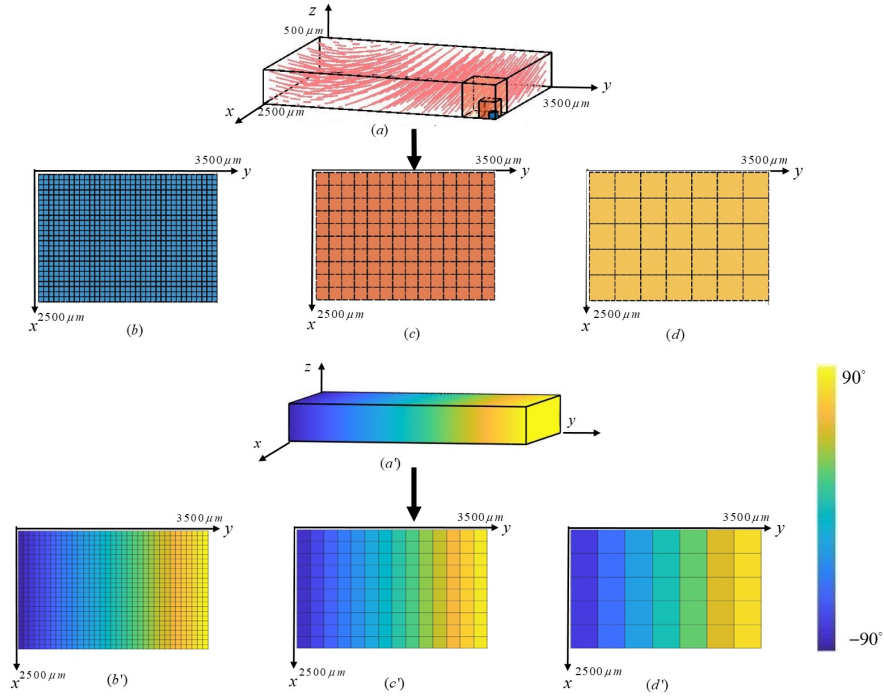


Figure 4.3: Virtual global tissue model with local change of orientation and three scales (voxel sizes). (a) Global tissue model of size  $2500 \times 3500 \times 500 \mu m^3$ . (b) Digitized virtual model with  $25 \times 35 \times 5$  voxels of size  $V_s$  (c)  $10 \times 14 \times 2$  voxels of size  $V_m$  and (d)  $5 \times 7 \times 1$  voxels of size  $V_b$ . (a'-d') Elevation angle  $\alpha$  in Models III and IV:  $\alpha$  varies only along the  $y$  axis while the azimuth angle  $\beta$  remains equal to 0.

In [98] the authors proposed, when a cylinder (a cell) overlaps the edges of the voxel (Figure 4.4-a), to create a copy of the cell overlapping on the opposite edge while keeping the same number of molecules in the voxel. This allows molecules to diffuse in an environment of similar spatial restriction but requires a particular arrangement (parallel organization) which cannot allow cells with various orientations to be considered. In [117] the authors proposed to extend the edge of the voxel (Figure 4.4-b) to ensure that none of the cells gets truncated and to distribute the simulated molecules randomly in the extended voxel. This allows to consider non-parallel geometries while ensuring that the molecules diffuse in a similar restricted environment.

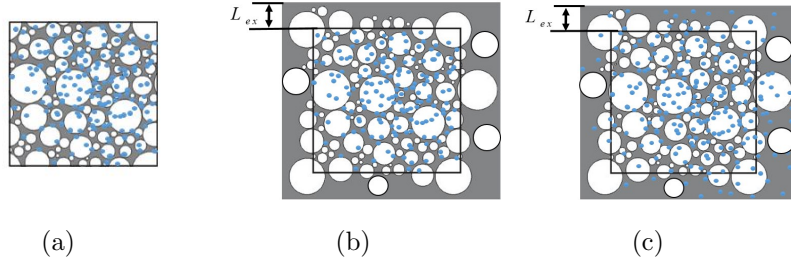


Figure 4.4: 2D section of a voxel and extended voxel containing cells (white disks) and water molecules (blue dots). (a) Voxel. (b) Extended voxel. The length  $L_{ex}$  corresponds to the maximum length for which the water molecule can diffuse outside the voxel during  $\Delta$ . (c) Extended voxel with water molecules limited to the inner voxel.

In our simulation, we defined an extended voxel with an edge  $L_{ex}$  larger than the edge of the voxel related to the scale of observation (Figure 4.4-c). At the beginning of the simulation, molecules were placed randomly in the voxel to ensure that only a very limited number of molecules will escape from the extended voxel (contrary to Figure 4.4-b). We determined the length of  $L_{ex}$  based on water molecules diffusing in a free environment, with a normal probability distribution of displacements  $L$  in a given direction during  $t$ , and a standard deviation of  $\sigma = \sqrt{2Dt}$ . For  $t = 100ms$ , over 99.9992% of water molecules remain within  $L = 4.5\sigma$  (i.e.,  $L = 100\mu m$ ). Therefore, if  $L_{ex} = 100\mu m$  when  $t = \Delta = 100ms$  (as in our simulations), all water molecules' movements, whether inside or outside the voxel, will remain within the extended voxel at this scale.

The size of extended voxels and the related density of water molecules used are listed in Table 4.2.

Table 4.2: Extended voxels: inner and outer voxels edges when  $L_{ex} = 100\mu m$  with their corresponding water molecules density  $\rho$  At the beginning of simulation when  $N = 10^5$ .

	$V_s$	$V_m$	$V_b$
Inner voxel	100 $\mu m$	250 $\mu m$	500 $\mu m$
Extended voxel	300 $\mu m$	450 $\mu m$	700 $\mu m$
$\rho$	0.1 / $\mu m^3$	$6 \times 10^{-3} / \mu m^3$	$8 \times 10^{-4} / \mu m^3$

### 4.2.3 Evaluation

In this section, we will discuss the evaluation metrics used to optimize MC parameters for accurate water diffusion simulations in cardiac tissue. By selecting the appropriate step duration ( $\tau$ ) and number of simulated molecules ( $N$ ), we ensure reliable and efficient simulations. Additionally, we will explore the significance of voxel size in achieving stable diffusion simulations, striking a balance between computational efficiency and accurate representation of cardiac tissue microstructure. Lastly, we will examine the critical role of diffusion duration ( $\Delta$ ). Understanding these factors will help us optimize MC parameters, voxel size, and diffusion duration for improved water diffusion measurements in cardiac tissue.

**Optimization of  $\tau$  and  $N$ :** In order to satisfy *Condition K*, *Condition l/s* and *Condition N*, we optimized the MC water diffusion simulation parameters  $\tau$  and  $N$  in an extended voxel with big voxel size  $Vb$  (more stable result according to the *Condition V*) for the four tissue models. We extracted the eigenvalues and analyzed their behavior when the values of  $\tau$  and  $N$  vary. The simulation error of eigenvalues [97, 98] was given by the normalized standard deviation defined by:

$$std_{\lambda_i} = \frac{\sqrt{\frac{1}{n-1} \sum_{j=1}^n (\lambda_i^j - \overline{\lambda_i^{ref}})^2}}{\overline{\lambda_i^{ref}}}, \quad (4.6)$$

for  $i=\{1,2,3\}$  corresponding to the three eigenvalues respectively. The averaged reference  $\overline{\lambda_i^{ref}}$  is the average value of 30 repetitions of  $\lambda_i$  obtained with the finest parameter values of the range of values tested *i.e.*  $\tau = 0.001$  ms and  $N=10^5$  in the whole voxel,  $N = 7 \times 10^4$  in ICS and  $N = 3 \times 10^4$  in ECS. We considered separately the two compartments ICS and ECS contained in the voxel (impermeable environment with  $P = 0 \mu m/ms$ ) and calculated the limitation ratio between  $l$  and  $s$  respectively in ICS and ECS according to the *Condition l/s*, which must be applied for any compartment spatial restriction size and diffusivity.

**Optimal voxel size for a stable water diffusion simulation:** To satisfy *Condition V*, we controlled the stability of eigenvalues across the virtual global

tissue models, successively for the three voxel sizes  $Vs$ ,  $Vm$  and  $Vb$  (see Figure 4.3) by observing the values of eigenvalues through the different voxels constituting the global virtual tissue and by calculating their average value as well as their standard deviation. We performed the analysis for both impermeable (separated ICS and ECS) and permeable environments. The number of voxels contained in the global tissue models was respectively equal to  $5 \times 35$ ,  $5 \times 14$  and  $5 \times 7$ .

**Critical diffusion duration  $\Delta$ :** We optimized the value of  $\Delta$  to satisfy the condition of *long diffusion duration*: this ensures that micro-structural information can be detected when a long diffusion duration  $\Delta$  is applied where most molecules can reach the edges of the cell and therefore testify to the spatial restriction. To do so the following condition must be fulfilled [128, 132]:

$$\begin{cases} \xi_{\Delta,ICS} = \Delta \times D_{ICS}/(d/2)^2 \geq 1, \\ \xi_{\Delta,ECS} = \Delta \times D_{ECS}/(a_l/2)^2 \geq 1. \end{cases} \quad (4.7)$$

$\Delta^{critical}$  is calculated when  $\xi_{\Delta} = 1$ . The value of  $\Delta^{critical}$  increases with  $d$  and  $a_l$  and when  $D$  decreases.  $\Delta_{whole}^{critical} = \max(\Delta_{ICS}^{critical}, \Delta_{ECS}^{critical})$ ,  $\Delta_{whole}^{critical} = 100ms$  for  $d = 20\mu m$ ,  $a_l = 20\mu m$ ,  $D_{ICS} = 1\mu m^2/ms$  and  $D_{ECS} = 2.5\mu m^2/ms$ ;  $\Delta_{whole}^{critical} = 25ms$  for  $d = 10\mu m$ ,  $a_l = 10\mu m$ .

This was also confirmed by following the evolution of the different eigenvalues as a function of the  $\Delta$  value.

### 4.3 Optimization of MC parameters

The optimization of Monte Carlo parameters can be approached in two steps. Firstly, water molecules were simulated within a single cell model (infinite cylinder) to optimize the values of  $\tau$  and  $N$ , ensuring compliance with the conditions outlined as *Conditions K*, *l/s*, and *N*. Subsequently, simulations were conducted within a multi-cell model incorporating the intracellular space (ICS) and extracellular space (ECS). In this step, the optimization of  $\tau$  and  $N$  was carried out

using an extended voxel with a larger voxel size ( $V_b = 500 \times 500 \times 500 \mu m^3$ ). Additionally, voxel size optimization was performed to satisfy *Condition V*, considering simulations within the global tissue model with various voxel sizes. It is important to note that all simulations within the multi-cell model were executed under equilibrium conditions, ensuring that the density of water molecules ( $\rho$ ) remained consistent across ICS and ECS compartments.

### 4.3.1 Single-cell scale

Figure 4.5 presents the simulation error ( $std_{\lambda_3^t}$ ) of  $\lambda_3^t$  for different values of  $\tau$  and  $N$  when  $\Delta = 100ms$  (satisfying the condition *LDD* as described in Section 5.2.3). When  $d = 20\mu m$ , it can be observed that  $std_{\lambda_3^t}$  decreases in an approximately linear manner as  $N$  increases, particularly when  $\tau \leq 0.1ms$ . However, in the case of  $d = 10\mu m$ ,  $std_{\lambda_3^t}$  exhibits a linear decrease only for  $\tau \leq 0.01ms$ , whereas for larger values of  $\tau$ , the curves tend to rise. Consequently, the boundary condition of  $l/d = \sqrt{6D\tau}/d \leq 0.04$  can be identified.

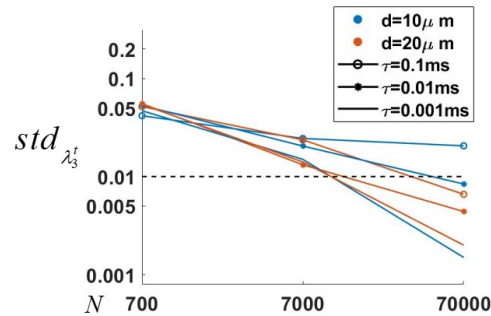


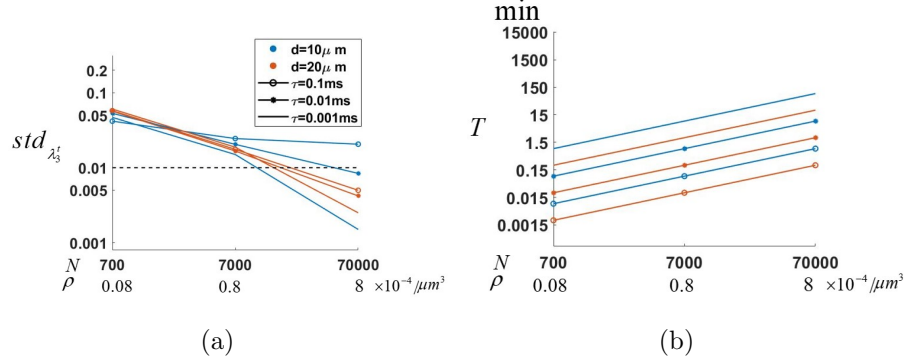
Figure 4.5: Single cell model- Optimization of  $\tau$  and  $N$  when  $\Delta = 100ms$  for two cell sizes. Simulation error  $std_{\lambda_3^t}$  wrt  $N$ .

## 4.3.2 Multi-cell scale

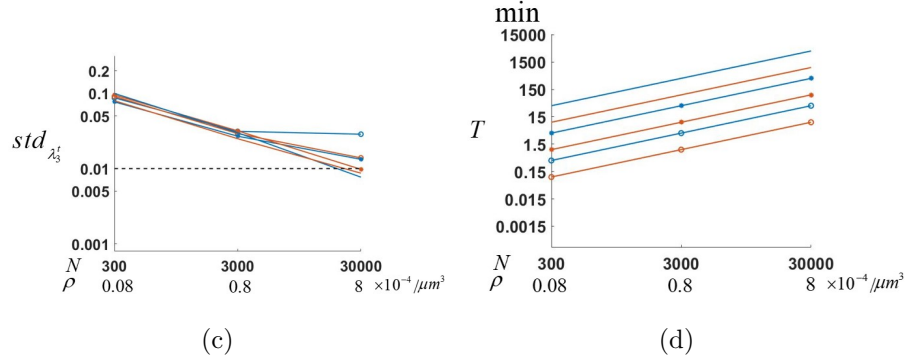
### 4.3.2.1 Optimization of $\tau$ and $N$

We examined the simulation error of  $\lambda_3$  ( $std_{\lambda_3}$ ) for different combinations of  $\tau$  and  $N$  under a long diffusion duration ( $\Delta = 100ms$ ) condition. The results are presented in Figure 4.6-a-c-e.

$$ICS, D_{ICS} = 1, P = 0$$



$$ECS, D_{ECS} = 2.5, P = 0$$



$$\text{Whole voxel}, D_{ICS} = 1, D_{ECS} = 2.5, P = 0.2$$

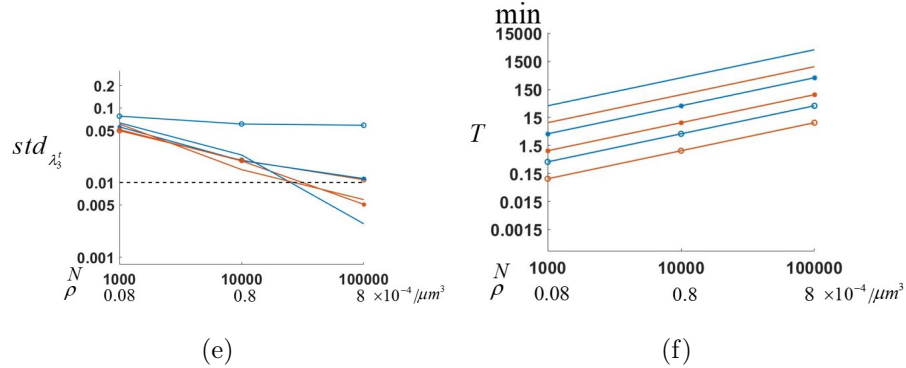


Figure 4.6: Model IV - one voxel: Optimization of  $\tau$  and  $N$  within  $Vb$  for two cell sizes.  $std_{\lambda_3}$  wrt  $N$  : a) ICS,  $P = 0$ ; c) ECS,  $P = 0$ ; e) whole voxel,  $P = 0.2$ . Computation time  $T$  wrt  $N$  : (b,d,f) for (a,c,e) respectively.

In the case of  $\mu_d = 20\mu m$  in the intracellular space (ICS) (Figure 4.6-a),  $std_{\lambda_3}$  exhibited a nearly linear decrease with increasing  $N$  when  $\tau \leq 0.1ms$ . For the extracellular space (ECS) (Figure 4.6-c),  $std_{\lambda_3}$  decreased linearly only when  $\tau \leq 0.01ms$ , while for larger values of  $\tau$ , the curves increased. The simulation

results from the whole voxel with a permeability of  $P = 0.02\mu m/ms$  (Figure 4.6-e) were identical to those from ECS.

For  $\mu_d = 10\mu m$ ,  $\tau \leq 0.01ms$  was selected for ICS (Figure 4.6-a), and for  $\mu_d = 20\mu m$ ,  $\tau \leq 0.001ms$  was chosen for ECS (Figure 4.6-c) and the whole voxel with  $P = 0.02\mu m/ms$  (Figure 4.6-e). These selected values of  $\tau$  are summarized in Table 4.3 and satisfy the *Condition l/s*. Specifically, for ICS,  $\tau \leq 0.01ms$  is selected for  $\mu_d = 10\mu m$  and  $\tau \leq 0.1ms$  for  $\mu_d = 20\mu m$ , ensuring  $l_{ICS}/\mu_d \leq 0.04$  – which is same with the result from one cell model. For ECS,  $\tau \leq 0.001ms$  is chosen for  $\mu_d = 10\mu m$  and  $\tau \leq 0.01ms$  for  $\mu_d = 20\mu m$ , ensuring  $l_{ECS}/\mu_{a_s} \leq 0.13$ .

Table 4.3: Model IV - one voxel: *Condition l/s*. White cells satisfy the results of optimization of  $\tau$  obtained from the analysis of Figure 4.6

$\tau$	$l_{ICS}$	$l_{ECS}$	$\mu_d$	$l_{ICS}/\mu_d$	$\mu_{a_s}$	$\mu_{a_l}$	$l_{ECS}/\mu_{a_s}$	$l_{ECS}/\mu_{a_l}$	$\frac{l_{ECS}}{(\mu_{a_l} + \mu_{a_s})/2}$
ms	$\mu m$	$\mu m$	$\mu m$		$\mu m$	$\mu m$			
0.1	0.77	1.22	10	0.08	1.5	10	0.83	0.12	0.21
			20	0.04	3	20	0.41	0.06	0.11
0.01	0.24	0.39	10	0.02	1.5	10	0.26	0.04	0.07
			20	0.01	3	20	0.13	0.02	0.03
0.001	0.08	0.12	10	0.008	1.5	10	0.08	0.01	0.02
			20	0.004	3	20	0.04	0.006	0.01

Furthermore, we evaluated the computation time ( $T$ ) for the Monte Carlo simulations presented in Figure 4.6-a-c-e, as shown in Figure 4.6-b-d-f. The computation time increased linearly with  $N$  and decreased  $\tau$  ( $K$  increasing). The simulation in ECS took longer due to tasks such as checking water molecule collisions with cell membranes and calculating new positions after reflection. Considering the simulation speed, we set the threshold of  $std_{\lambda_3}$  to 0.01, with a consistent density  $\rho$  in all compartments. This corresponds to selecting  $N = 10^5$  in the whole voxel,  $N = 7 \times 10^4$  in the ICS, and  $N = 3 \times 10^4$  in ECS. These threshold-based values of  $N$  are valid for both  $\mu_d$  values of cell diameters. The obtained  $\tau$  values are applicable to Models I, II, III, and IV, for diffusion durations ( $\Delta$ ) ranging from 10 to 100ms.

### 4.3.2.2 Recommended diffusion duration $\Delta$

To validate the critical values of diffusion duration ( $\Delta$ ) discussed in Section 4.2.3, we examined the mean and standard deviation of  $\lambda_1$  and  $\lambda_3$  for Monte Carlo (MC) simulations of global model IV with heterogeneous cell diameter and orientation ( $\mu_d = 20\mu m$ ). The simulations were conducted using small ( $V_s$ ) and large ( $V_b$ ) voxel sizes, as depicted in Figure 4.7.

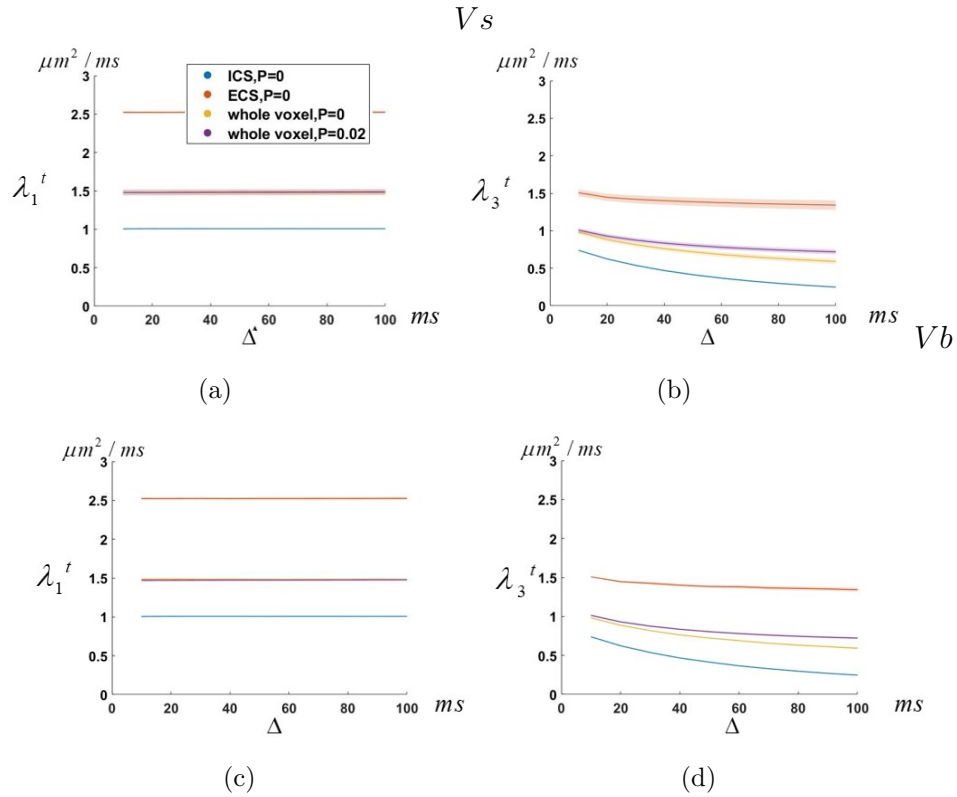


Figure 4.7: Model IV - global model: Evolution of the eigenvalues  $\lambda^t$  from a transient to a stationary regime according to the diffusion time  $\Delta$  in ICS, ECS, and in the whole voxel, respectively. MC simulations were performed for model IV and voxels of size  $V_s$  (first line) and  $V_b$  (second line) with  $D_{ICS}=1$ ,  $D_{ECS}=2.5$ ,  $R_{ICS}=70\%$ ,  $\tau = 0.01ms$ ,  $\rho = 0.1/\mu m^3$  and  $\rho = 8 \times 10^{-4}/\mu m^3$  for  $V_s$  and  $V_b$  respectively.

We calculated the mean and standard deviation of  $\lambda_1$  and  $\lambda_3$  for  $25 \times 35 \times 5$  and  $5 \times 7 \times 1$  constituent voxels of the global model, corresponding to  $V_s$  and  $V_b$ ,

respectively. We analyzed the intracellular space (ICS) and extracellular space (ECS) independently (in an impermeable environment) as well as the entire voxel (with permeability values of  $P = 0$  and  $0.02\mu m/ms$ ).

The eigenvalues in Figure 4.7 provide insights into the nature of the diffusion phenomenon.  $\lambda_1$  measures the apparent diffusion coefficient (ADC) along the long axis of the virtual cell and remains similar to the free diffusion coefficient, regardless of  $\Delta$ . On the other hand,  $\lambda_2$  and  $\lambda_3$  measure ADC in a circular section of the cell perpendicular to the long axis and decrease similarly with increasing  $\Delta$ , indicating restricted diffusion. The eigenvalues decrease until they reach a stationary point, in accordance with the condition of a *long duration of diffusion* mentioned in Section 4.2.3. However, if  $\Delta$  is too small compared to the size of the spatial restriction, the diffusion may still be in a transient regime. For instance, a  $\Delta$  value of 40 ms corresponds to a transient state for  $d = 20\mu m$ , whereas a  $\Delta$  value of 100 ms represents a convergent state where the diffusion phenomenon is stationary.

Under the impermeable environment, the eigenvalues from the entire voxel closely approximate the volumetric average of the results from ICS and ECS [98]. This relationship can be expressed as:

$$\lambda_{\text{whole},P=0} = \lambda_{ICS} \times R_{ICS} + \lambda_{ECS} \times (1 - R_{ICS}). \quad (4.8)$$

In ICS and ECS,  $\lambda_1$  equals the free diffusivity, while the values in the entire voxel vary due to the presence of local restricted intracellular space ( $R_{ICS}$ ) for  $P = 0$  and  $P = 0.02$ . In model IV,  $R_{ICS}$  has a standard deviation of approximately 2.3% and 0.5% for  $Vs$  and  $Vb$ , respectively (as shown in Table 4.4). Variations in  $\lambda_3$  among voxels are mainly caused by the local differences in  $d$ , as well as the discrepancy in diffusivity between ICS and ECS ( $D_{ICS}$  and  $D_{ECS}$ ). This variability is less pronounced in ICS due to the relatively limited variation in  $d$  ( $\mu_d$ ) among voxels (standard deviation of approximately  $0.35\mu m$  and  $0.07\mu m$  for  $Vs$  and  $Vb$ , respectively, as shown in Table 4.4 for model IV). However, it

becomes more pronounced in ECS, owing to the greater variability in cell arrangement, resulting in locally distinct spatial restriction values. This phenomenon is observed throughout the entire voxel, regardless of  $P = 0$  or  $P = 0.02$  [112].

### 4.3.2.3 Optimal voxel size

As depicted in Figure 4.8, the estimated value of  $\lambda_3$  exhibits fluctuations among different voxels in the various global models under a permeable diffusion environment with  $P = 0.02 \mu m/ms$  and  $\Delta = 100ms$ .

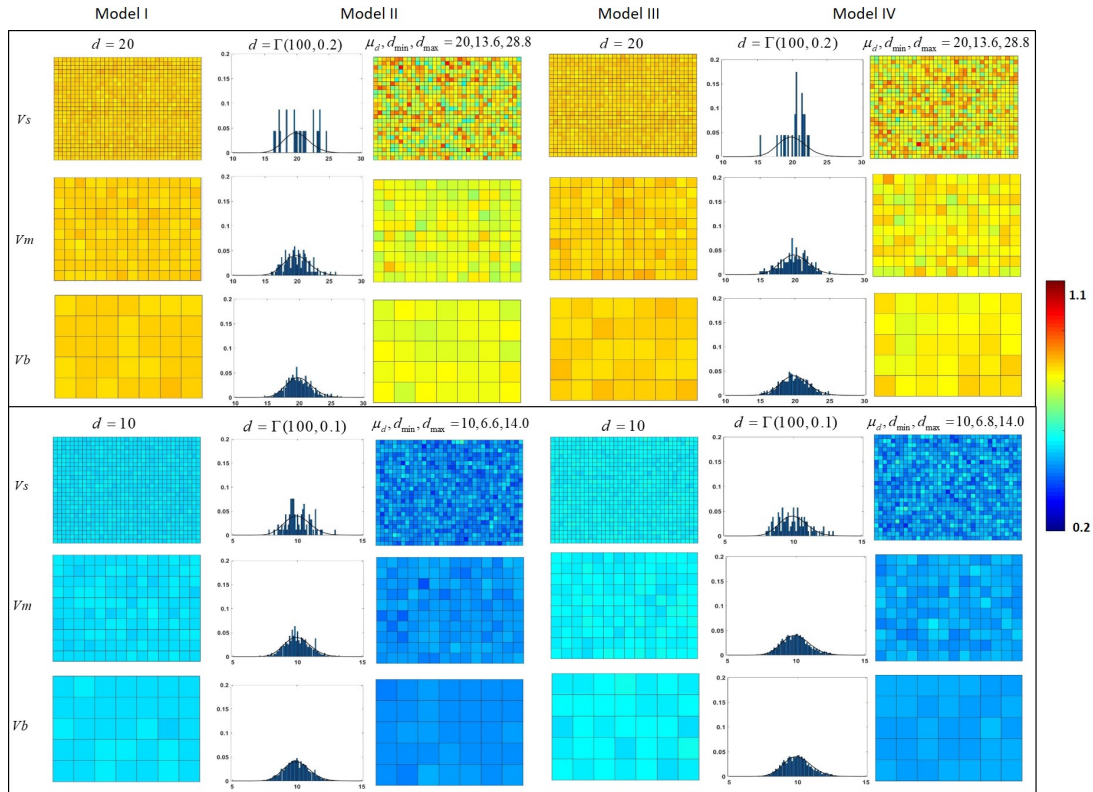


Figure 4.8: Models I-IV global models-Spatial representation of estimated values of  $\lambda_3$  ( $\mu m^2/ms$ ) with three scales ( $V_s$ ,  $V_m$  and  $V_b$ ) when  $\Delta = 100ms$  displayed using the colorbar given on the right. Normalized distribution of cell diameters displayed in one voxel in Models II and IV (the case of heterogeneous cell diameter) with  $\mu_d = 20$ .

For models I and III (homogeneous diameters),  $\lambda_3$  remains relatively stable even at the smallest voxel size ( $V_s$ ) for both cell diameters ( $d$ ). In contrast, for

models II and IV (heterogeneous diameters),  $\lambda_3$  becomes highly unstable at the smallest scale  $Vs$ , consistent with the findings in Figure 4.7. This phenomenon can be explained by examining the normalized diameter distribution within a voxel. The diameter distribution in Figure 4.8 deviates from the ideal distribution for  $Vs$  and poorly matches the theoretical distribution described in Section 3.2.2. However, as the scale increases, the diameter distribution becomes closer to the theoretical distribution, which helps reduce the spatial variability of  $\lambda_3$ . The variability is lower for  $\mu_d = 10\mu m$  due to the inclusion of more cylinders within the same voxel.

Table 4.4 provides the number of cells, average cell diameter, local  $R_{ICS}$ , and estimated eigenvalues for three voxel sizes across the global tissue models (I, II, III, and IV). To ensure stability of the local  $R_{ICS}$  and accurate estimation of eigenvalues, we impose a limit on the standard deviation of  $\lambda_1$  and  $\lambda_3$ , which must be less than  $0.015\mu m^2/ms$  and  $0.012\mu m^2/ms$ , respectively. This leads to the conclusion that, for Models II and IV, the largest voxel size  $Vb$  ( $500 \times 500 \times 500\mu m^3$ ), encompassing over 500 cylinders, is required when  $\mu_d = 20\mu m$ , whereas the voxel size  $Vm$  ( $250 \times 250 \times 250\mu m^3$ ), also encompassing over 500 cylinders, suffices for  $\mu_d = 10\mu m$ .

Table 4.4: Models I-IV - global model: Voxel size optimisation by reporting voxel size  $V$ , mean cell diameter  $\mu_d$ , cells number, cellular volume fraction, estimated  $\lambda_1^t$  and  $\lambda_3^t$  for two  $d$  cases when  $\Delta = 100ms$ . White cells correspond to a standard deviation of  $\lambda_3^t$  less than 0.012.

Size	$\mu_d$	Cells number	$R_{ICS}(\%)$	$\lambda_1(\mu m^2/ms)$	$\lambda_3(\mu m^2/ms)$
<b>Model I</b>					
Vs	20	23	68	1.49±0.011	0.73±0.004
Vm	20	137	70	1.49±0.010	0.73±0.005
Vb	20	537	69	1.49±0.010	0.73±0.004
Vs	10	93	69	1.50±0.009	0.58±0.005
Vm	10	537	69	1.49±0.009	0.58±0.004
Vb	10	2219	70	1.49±0.009	0.58±0.004
<b>Model II</b>					
Vs	20 ± 0.37	23	69±2.7	1.49±0.039	0.71±0.035
Vm	20 ± 0.14	137	70±1.1	1.48±0.018	0.71±0.015
Vb	20 ± 0.06	537	70±0.5	1.48±0.013	0.71±0.010
Vs	10 ± 0.09	93	69±1.4	1.49±0.022	0.54±0.020
Vm	10 ± 0.03	537	69±0.5	1.49±0.013	0.54±0.010
Vb	10 ± 0.01	2219	70±0.3	1.49±0.005	0.54±0.004
<b>Model III</b>					
Vs	20	28±4	68±0.2	1.50±0.009	0.74±0.005
Vm	20	181±17	70±0.1	1.50±0.008	0.74±0.005
Vb	20	695±57	69±0.02	1.50±0.008	0.74±0.005
Vs	10	123±12	69±0.2	1.50±0.008	0.59±0.005
Vm	10	695±57	69±0.02	1.50±0.008	0.59±0.005
Vb	10	2831±148	70±0.005	1.50±0.008	0.59±0.005
<b>Model IV</b>					
Vs	20 ± 0.35	28±4	69±2.3	1.49±0.037	0.72±0.032
Vm	20 ± 0.14	181±17	70±1.2	1.48±0.019	0.72±0.016
Vb	20 ± 0.07	695±57	70±0.5	1.48±0.014	0.72±0.012
Vs	10 ± 0.09	123±12	69±1.5	1.50±0.024	0.55±0.020
Vm	10 ± 0.04	695±57	69±0.5	1.48±0.014	0.55±0.012
Vb	10 ± 0.01	2831±148	70±0.3	1.49±0.007	0.55±0.005

## 4.4 Conclusion

**In this contribution**, our main focus was on analyzing the virtual cardiac tissue models we developed, incorporating realistic physiological parameters based on histological data. The goal was to optimize key parameters, namely the duration of each update ( $\tau$ ) and the number of simulated molecules ( $N$ ), in order to ensure accurate and efficient Monte Carlo simulations.

Our simulation results, shown in Figure 4.6, revealed that the same optimal parameters can be applied to all four cardiac tissue models. In particular, we found that the choice of  $\tau$  and the length of the update step ( $l$ ) in the Monte Carlo simulation were influenced by the diameter of the cells. To meet the criteria of *condition*  $l/s$ , an optimal ratio of  $l_{ICS}/\mu_d \leq 0.04$  was identified for impermeable intracellular space (ICS) (Table 4.3), consistent with previous findings in brain tissue modeling [113]. Similarly, for impermeable extracellular space (ECS), an optimal ratio of  $l_{ECS}/((\mu_{a_s} + \mu_{a_l})/2) < 0.05$  was determined.

The number of cylinders (cells) used in Monte Carlo simulations has been found to be a crucial factor in other studies. While previous works on white matter axonal structures suggested using 10,000 cylinders [97, 137], our simulations involved larger cylinders and lower heterogeneity in diameter to mimic heart tissue. We found that using a voxel size of  $500 \times 500 \times 500 \mu m^3$  (containing 500 cylinders) achieved stable simulations for  $\mu_d = 20 \mu m$ , while a voxel size of  $250 \times 250 \times 250 \mu m^3$  (also containing 500 cylinders) was sufficient for  $\mu_d = 10 \mu m$  (Table 4.2). This aligns with clinical studies indicating that a voxel size of approximately 1 – 2 mm can effectively capture local geometrical heterogeneity [121].

The density of water molecules ( $\rho$ ) used in Monte Carlo simulations is typically much lower than the observed density in biological tissues. Our simulations considered a large enough number of water molecules ( $N$ ) to ensure reasonable simulation errors and reliable estimation of the diffusion tensor. For example, we set  $N = 10^5$  in a voxel size of  $500 \times 500 \times 500 \mu m^3$ , resulting in a density of

$\rho = 8 \times 10^{-4}$  molecules per  $\mu m^3$ . However, when using a smaller voxel size ( $Vs$ ), the density increased to 0.1 per  $\mu m^3$  (Table 4.2).

Analyzing the effect of cell orientation heterogeneity in the virtual tissue models, we observed that the choice of voxel size had a significant impact. Models I and III (with homogeneous diameters) showed relatively stable  $\lambda_3$  values even at the smallest voxel size, while Models II and IV (with heterogeneous diameters) exhibited high instability at the same scale, consistent with the findings in Figure 4.8. Analyzing the normalized diameter distribution within a voxel helped explain these observations (Figure 4.8). As the voxel size increased, the diameter distribution approached the theoretical distribution, reducing the spatial variability of  $\lambda_3$ . This variability was more pronounced in ECS due to the greater flexibility in cell arrangement. These findings were consistent across the entire voxel, regardless of permeability conditions [112].

Additionally, our results highlighted the sensitivity of radial diffusion to cell diameter in the virtual model, while  $\lambda_1^t$  remained stable.  $\lambda_3^t$  exhibited a decrease with decreasing diameter, as shown in Table 4.4, consistent with previous simulations [3]. This can be attributed to the absolute displacements of simulated molecules along the most restricted direction (associated with  $\lambda_3^t$  and  $\lambda_2^t$ ), which reach a constant value in ICS once the *long diffusion duration* condition is met [132]. This constant value is directly influenced by the size of the spatial restriction, i.e., the cell diameter. On the other hand,  $\lambda_3^t$  and  $\lambda_2^t$  in ECS reach a constant value when the *Condition LDD* is satisfied, determined by  $R_{ICS}$ ,  $D_{ECS}$ , and the cell arrangement, rather than the cell diameter [112].

# Chapter 5

## dMRI observation of water diffusion in cardiac tissue

In this chapter, we present the development of a virtual MRI device that mimics the typical observation parameters of a diffusion MRI sequence known as Pulsed Gradient Spin-Echo (PGSE). Our aim is to use this virtual MRI device to observe and analyze the simulated diffusion of water molecules within a cardiac tissue model. We specifically investigate the influence of key sequence parameters, including the diffusion duration ( $\Delta$ ) and the gradient pulse duration ( $\delta$ ), on the estimation of structural characteristics in the observed water diffusion patterns. By comparing the results obtained from the virtual MRI observations with the reference data produced by Monte Carlo simulations, we gain insights into the impact of sequence parameters on the observed water diffusion behavior within the cardiac tissue model.

### 5.1 State of the art

As reported in Table 5.1, numerous studies have focused on assessing the estimation of diffusion properties, such as the three eigenvalues of the diffusion tensor,

mean diffusivity (MD), and fractional anisotropy (FA), using diffusion MRI experiments. These studies have been complemented by virtual observations conducted using Monte Carlo methods, both in brain tissue [140, 107, 141, 142, 126, 143, 127] and heart tissue [117, 3]. However, when aiming to detect microstructural information in biological tissue, the selection of observation sequence parameters is constrained by certain conditions.

Table 5.1: Diffusion MRI : Clinical<sup>1</sup> vs Virtual MRI

Ref.	Echo time TE ms	Diffusion duration $\Delta$ ms	Gradient duration $\delta$ ms	Gradient strength $G_d$ $10^{-6}T/mm$	q-value $mm^{-1}$	b-value $s/mm^2$	Scale $V_V$ $\mu m^3$
<b>Clinics: Heart</b>							
[5]	23	12	9	80	-	340	-
[63]	51	-	-	40	-	50-100	$2600^2 \times 6000$
[144]	38-62	-	-	-	-	15-400	-
[64]	43	30	15/20	-	-	200	$2700^2 \times 6000$
[93]	61	-	-	80	-	500	$1600^2 \times 2000$
[81]	45-115	-	-	40	-	50-450	$1600^2 \times 10000$
[92]	61-65	-	8.3	87	-	340	$2200^2 \times 6000$
<b>Clinics: Brain</b>							
[142]	-	40-70	30	9.8-27.6	12-35	250-2000	$2500^3$
<b>Simulation: Muscle</b>							
[106]	-	20-750	2	-	-	500	$200^3$
[122]	-	40-200	20	10-120	9-120	96-80000	$2500^3$
<b>Simulation: Heart</b>							
[123]	-	50	0.2	2000	17	572	$8^3$
[130]	-	60	0.2	3000	17	689	$2000^3$
[117]	-	9-40	2.5-5	150-880	-	400-7500	$100^3 - 500^3$
[131]	39/31	20/17	10/4	40/80	-	450	$2800^2 \times 8000$
[136]	-	25-100	0.4-50	-	0-90	-	-
[133]	-	50-1000	0.01-1.5	-	-	1	-
[3]	-	26	2	-	-	700	$1380^2 \times 1400$
<b>Simulation: Brain</b>							
[113]	-	0-15	-	-	-	-	$125^3$
[118]	-	1-100	-	-	-	-	$10^3$
[97]	-	16-45	7-10	131-140	42-56	1930-13190	$230^3$
[98]	-	100	5-80	10-100	2-341	-	$36.5^3$
[119]	-	37.7	31.7	40	54	2600	$150^3$
[120]	-	0.03-100	0.2-20	-	-	0-1000	$125^3$
[134]	-	116	-	0-80	-	200	$2000^3$

1. 1.5T/3T MRI scanners.

Most clinical diffusion MRI studies utilize a low b-value (typically below  $550 s/mm^2$ ) with a relatively short diffusion duration ( $\Delta$ ) ranging from 10 to 50 ms, as shown in Table 5.1. However, these parameters do not fulfill the requirements of the *Long Diffusion Duration (LDD)* condition when applied to cardiac tissue. Additionally, the gradient pulse duration ( $\delta$ ) used in clinical settings is often several or tens of milliseconds, thereby violating the *Short Gradient Pulse (SGP)* condition.

Moreover, in clinical practice, diffusion MRI tends to average out the diffusion properties over large observation scales, represented by the voxel size. Consequently, the local distribution of myocyte diameters and variations in the cell volume fraction remain undetectable. Notably, a study by Hall et al. [145] demonstrated that the error in diffusion MR signal for two observation scales followed a line of constant b-value, indicating the existence of an optimal b-value that is more sensitive to the distribution of cylinder radii within the tissue.

In our work, we thoroughly analyze the impact of the diffusion duration ( $\Delta$ ) and gradient pulse duration ( $\delta$ ) on the estimation of diffusion properties, as well as the characterization of spatial restriction sizes within the cardiac tissue model. We aim to verify the specific conditions that should be satisfied to ensure accurate diffusion measurements in the context of our study.

## 5.2 Virtual dMRI device

In the context of MRI, the measurement of water molecule diffusion within biological tissues is achieved through the utilization of an appropriate imaging sequence, such as the widely used Pulsed Gradient Spin-Echo (PGSE) sequence. As described in Chapter 2.2.2, this sequence involves the application of a pair of gradient pulses positioned between the  $90^\circ$  RF pulse and the  $180^\circ$  RF pulse. To illustrate this sequence in relation to Monte Carlo simulations, we have provided a revised depiction in Figure 5.1-a, where the corresponding update steps in the Monte Carlo simulation are also illustrated.

The PGSE sequence is composed of two diffusion-sensitizing gradients characterized by their duration ( $\delta$ ), strength ( $G_d$ ), and direction ( $\vec{G}_d$ ). These gradients are employed to encode the diffusion behavior of water molecules during the interval denoted as  $\Delta$ , commonly referred to as the diffusion duration [4]. This interval captures the time during which the diffusion of water molecules is probed and quantified by the MRI sequence.

## 5.2.1 Water diffusion displacements during two gradient pulses

During the  $\delta$  interval within the PGSE sequence, the movement of water molecules deviates from their theoretical path, as depicted in Figure 5.1-b.

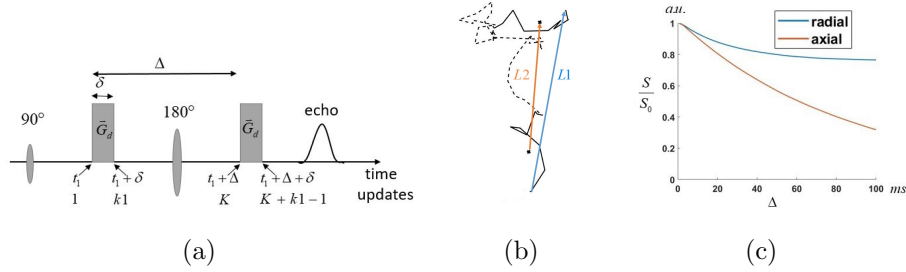


Figure 5.1: (a) Classic MRI Pulsed Gradient Spin-Echo (PGSE) sequence with diffusion duration  $\Delta$ , pulse duration  $\delta$ , and gradient strength  $|\vec{G}|$  [4]. (b) Water molecule moves in a free diffusion environment,  $L1(\delta = 0)$ : displacement from start to end point; Bold lines: moves during diffusion gradient pulses; x: location of the centers of mass;  $L2$ : displacement between consecutive centers of mass. (c) Simulated restricted (radial) and free (axial) diffusion MRI signals  $E_{\vec{G}}(\Delta, \delta, |\vec{G}|)$  (Eq. 5.2) of  $N = 10^5$  water molecules diffusing in a cylindrical core of diameter  $d = 20\mu\text{m}$  with  $D = 1\mu\text{m}^2/\text{ms}$ ,  $\delta = 5\text{ms}$ ,  $|\vec{G}| = 80\mu\text{T}/\text{mm}$ .

The displacement of an individual molecule  $i$  can be expressed mathematically as:

$$L_i(\Delta, \delta) = \frac{1}{k1} \left( \sum_{k=1}^{k1} r_i(k, x, y, z) - \sum_{k=K}^{K+k1-1} r_i(k, x, y, z) \right), \quad (5.1)$$

In Equation 5.1, the term  $r_i(k, x, y, z)$  represents the three-dimensional location  $(x, y, z)$  of molecule  $i$  at the  $k^{\text{th}}$  update. Here,  $k1$  represents the number of updates that occur during the  $\delta$  interval, while  $K$  (as shown in Figure 5.1-a) represents the starting point of the updates during the  $\Delta$  interval.

## 5.2.2 Physical versus Virtual observation

In our simulation, we utilize diffusion MRI (dMRI) to measure the diffusion of the simulated moving water molecules and calculate the virtual MRI signal  $E_{\vec{G}}(\Delta, \delta, G)$ . This allows us to assess the amplitude loss of the MRI signal due to the displacement of water molecules, which results in a phase shift. The virtual MRI signal  $E_{\vec{G}}(\Delta, \delta, |\vec{G}|)$  is given by:

$$E_{\vec{G}}(\Delta, \delta, |\vec{G}|) = \lim_{N \rightarrow \infty} \frac{1}{N} \sum_{i=1}^N \cos(\phi_{i,\vec{G}}(\Delta, \delta, |\vec{G}|)), \quad (5.2)$$

where  $\phi_{i,\vec{G}}(\Delta, \delta, |\vec{G}|)$  represents the phase shift of molecule  $i$  during the PGSE sequence. For rectangular diffusion gradient pulses, its expression is:

$$\phi_{i,\vec{G}}(\Delta, \delta, |\vec{G}|) = 2\pi q \times L_{i,\vec{G}}(\Delta, \delta), \quad (5.3)$$

where,  $\gamma$  denotes the gyromagnetic ratio of the proton,  $q = \frac{\gamma\delta|\vec{G}|}{2\pi}$ , and  $L_{i,\vec{G}}(\Delta, \delta)$  represents the projection of  $L_i(\Delta, \delta)$  along the direction  $\vec{G}$  of the gradient. Figure 5.1-c demonstrates that in a cylindrical core simulation, the axial signal along the core's axis decreases faster compared to the radial signal perpendicular to the axial direction. This is due to slower radial diffusion caused by cellular wall restrictions.

The apparent diffusion coefficient along  $\vec{G}$ , denoted as  $ADC_{\vec{G}}(\Delta, \delta, |\vec{G}|)$ , is calculated from the MRI signal attenuation using the Stejskal–Tanner equation, assuming a Gaussian distribution of molecule displacements [4]:

$$E_{\vec{G}}(\Delta, \delta, |\vec{G}|) = e^{-bADC_{\vec{G}}(\Delta, \delta, |\vec{G}|)}, \quad (5.4)$$

where  $b = (\gamma\delta|\vec{G}|)^2(\Delta - \frac{1}{3}\delta)$  for rectangular pulses. This factor reflects the strength and timing of the gradients and translates into the overall diffusion

weighting. At least six non-coplanar direction measurements are necessary to evaluate the voxel-wise diffusion tensor  $\underline{ADC}$  since it is a symmetric matrix ( $ADC_{mn} = ADC_{nm}$ ) according to Equation 2.11. In our calculations, we employ 21 gradient pulse directions  $\vec{G}$  to compute the observed values as it is widely used in clinical settings [146]. Furthermore, for a more precise characterization of water molecule diffusion, the observed eigenvalues  $\lambda^o(\Delta, \delta, |\vec{G}|)$  can be inferred from the diffusion tensor calculated from the signal, as indicated in Equation 2.11.

### 5.2.3 Conditions on the MR observation parameters

In order to ensure that a diffusion MRI sequence (as shown in Figure 5.1-a) gives a valid estimate of the structural characteristics of the observed biological tissue, three basic conditions must be met:

- *Condition  $\delta/\Delta$* : The gradient pulse duration  $\delta$  should be significantly smaller than the diffusion duration  $\Delta$ . This assumption treats the movements of molecules within two  $\delta$  intervals as independent processes [139].
- *Condition LDD*: A long diffusion duration  $\Delta$  allows molecules to reach cell edges and capture microstructural information. In ICS, this condition results in a stable distribution of simulated molecules' displacements on the restricted diffusion plane. ADC in ICS follows an inverse relationship with  $\Delta$ , providing valuable insights into microstructure. However, in ECS, ADC on the restricted diffusion plane no longer decreases with increasing  $\Delta$ , indicating relatively unrestricted diffusion and minimal impact of tissue microstructure on observed ADC values [112, 113].
- *Condition SGP*: The gradient pulse duration  $\delta$  should be short enough for molecules to travel shorter distances compared to the spatial dimension of the compartment. This condition ensures that the diffusion gradient pulse does not significantly affect the observed diffusion behavior in a cylinder model with a given diameter and diffusivity in ICS [94, 129, 91, 147].

## 5.2.4 Evaluation

Our study began by investigating the impact of diffusion duration ( $\Delta$ ) and gradient pulse duration ( $\delta$ ) on specific conditions (*Conditions LDD, SGP*) using a single cell model (infinite cylinder). We compared the acquired diffusion MRI (dMRI) signal with the analytical model discussed in Chapter 2.3.2.

Subsequently, we extended our analysis to a larger voxel size and examined the conditions (*Conditions  $\delta/\Delta$ , LDD, SGP*). Due to the lack of a reliable analytical model, we compared the eigenvalues obtained from theoretical results ( $\lambda^t$ ) with the observed results ( $\lambda^o$ ). We explored a wider range of  $\Delta$  and  $\delta$  values, specifically ranging from  $\Delta = 10$  to 150 ms and  $\delta = 2$  to 50 ms, surpassing the typical values used in clinical settings (refer to Table 5.1).

Here are the key evaluation metrics for each condition:

- *Condition  $\delta/\Delta$* : We determined the optimal ratio between  $\delta$  and  $\Delta$  by minimizing the bias in the observed value of  $\lambda_3^o$  ( $\lambda_3^t - \lambda_3^o$ ) with a bias threshold set at  $0.05\mu m^2/ms$ .
- *Condition LDD*: Critical values of  $\Delta$  were identified where the mean displacement of simulated molecules,  $|L_{\lambda_3}|$ , reached a constant value in the intracellular space (ICS) while  $\lambda_3$  no longer decreased in the extracellular space (ECS). We calculated  $|L_{\lambda_3}|$  using  $|L_{\lambda_3}| = \sqrt{2\Delta\lambda_3}$  (refer to Eq. 4.5). Additionally, the full width at half maximum of the displacement distribution (*FWHM*) and the cell diameter ( $d$ ) were estimated from  $|L_{\lambda_3}|$  using  $FWHM = \sqrt{8 \ln 2} |L_{\lambda_3^o}|$  and  $d = 1.22FWHM$  [107, 91].
- *Condition SGP*: Critical values of  $\delta$  were identified by minimizing the normalized bias of the observed value  $\lambda_3^o$  compared to the theoretical value ( $(\lambda_3^t - \lambda_3^o)/\lambda_3^t$ ), following the approach used in similar studies [91, 147]. The threshold for the normalized bias of  $\lambda_3$  was set at 20%. Estimation of the cell diameter was also performed using  $|L_{\lambda_3}|$  and compared to the actual value.

## 5.3 Optimization of observation parameters

### 5.3.1 Single-cell scale

We conducted first experiments using a single-cell model to investigate the influence of diffusion duration ( $\Delta$ ) and gradient pulse duration ( $\delta$ ) on the signal decay of Monte Carlo simulations. The results were compared with the analytical model, as depicted in Figure 5.2.

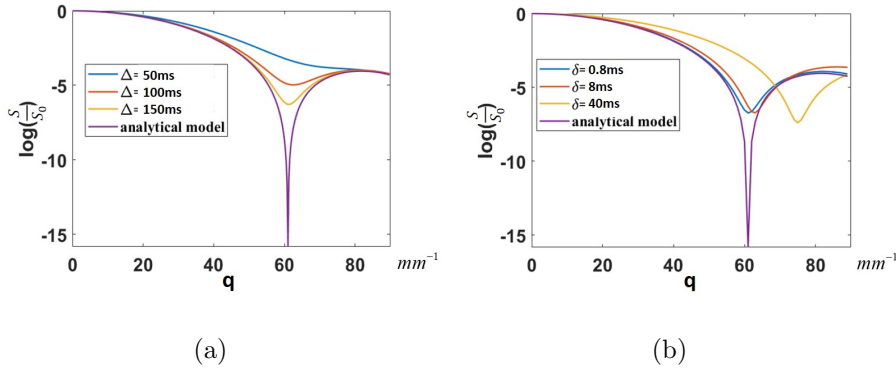


Figure 5.2: Single cell model: (a) Exploring the *Conditions LDD*: Evolution of  $\frac{S}{S_0}$  along radial direction vs  $qr$  for  $\Delta = 25 - 75ms$  when  $\delta = 0.4ms$ . (b) Exploring the *Conditions SGP*: Evolution of  $\frac{S}{S_0}$  along radial direction vs  $qr$  for  $\delta = 0.4 - 20ms$  when  $\Delta = 100ms$ . Other MC parameters are set according to:  $D = 1 \times 10^{-3}mm^2/s$ ,  $\tau = 0.1ms$  and  $N = 10^6$ .

From a qualitative perspective, we observed that as  $\Delta$  increased from 50 ms to 150 ms, the first diffraction pattern gradually emerged, particularly when  $\Delta \geq 100$  ms. Notably, at  $\Delta = 100$  ms, the first diffraction pattern appeared at  $q = 62.5 mm^{-1}$ , slightly deviating from the analytical model's value of  $q = 61 mm^{-1}$ . On the other hand, when  $\delta$  increased from 0.8 ms to 40 ms, the first diffraction pattern shifted to higher  $q$ -values.

From a quantitative perspective, we compared the microstructural information obtained from the diffusion diffraction pattern. The parameters  $q_{diff}$  and  $d_q$  were examined, where  $q_{diff}$  represents the  $q$ -value when the first diffraction pattern

occurs, and  $d_q$  is the diameter calculated using  $d_q \times q_{\text{diff}} = 1.22$  [110, 95]. In our simulations, the diameter of the cylindrical core was  $20\mu\text{m}$ , thus the expected values for these parameters are known and correspond to  $d_{\text{real}} = 20\mu\text{m}$  and  $q_{\text{real}} = 61\text{ mm}^{-1}$ .

Analyzing the results obtained for varying  $\Delta$ , as summarized in Table 5.2, we observed that  $d_q$  remained relatively stable and aligned well with the expected value when  $\Delta \geq 100\text{ ms}$  and  $\xi_\Delta \geq 1$ . On the other hand, when examining the results for varying  $\delta$ ,  $d_q$  decreased from  $20\mu\text{m}$  to  $11.6\mu\text{m}$ . The bias remained below 15% for  $\delta \leq 30\text{ ms}$  and  $\xi_\delta \leq 0.3$ . These findings highlight the impact of  $\Delta$  and  $\delta$  on the diffusion diffraction pattern and the estimation of microstructural parameters.

Table 5.2: Micro-structural information obtained from MC simulation

		Diffusion duration				
Param.	unit	$\Delta = 50$	$\Delta = 100$	$\Delta = 150$	$\Delta = 200$	
$q_{\text{diff}}$	$mm^{-1}$	-	62.5	61	61	
$d_q$	$\mu m$	-	19.6	20	20	
$ d_q - d_{\text{real}} /d_{\text{real}}$	-	-	0.02	0	0	
		Gradient pulse duration				
Param.	unit	$\delta = 0.8$	$\delta = 8$	$\delta = 30$	$\delta = 40$	$\delta = 100$
$q_{\text{diff}}$	$mm^{-1}$	61	63	71	75	105
$d_q$	$\mu m$	20	19.4	17.6	16.2	11.6
$ d_q - d_{\text{real}} /d_{\text{real}}$	-	0	0.03	0.12	0.19	0.42

### 5.3.2 Multi-cell scale

In this section, we conducted experiments in the intracellular (ICS) and extra-cellular (ECS) compartments using two types of models: Model I and Model IV.

In Model I, the parameters  $d$ ,  $a_l$ , and  $a_s$  were uniform throughout the tissue. On the other hand, in the heterogeneous model (Model IV), these parameters followed a Gaussian distribution, as illustrated in Figure 5.3.

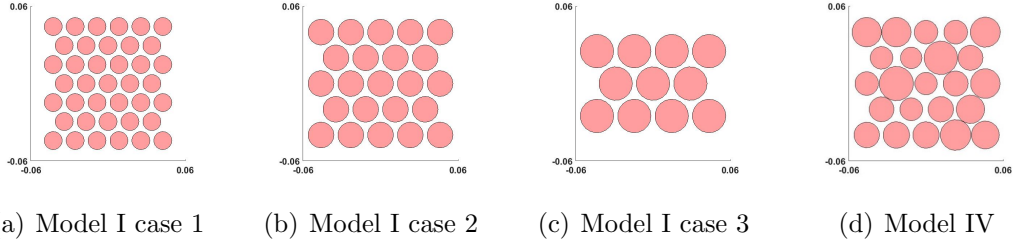


Figure 5.3: (a-c) Cross sections (restricted planes) of three homogeneous models: (a) Case 1 where  $d = 14\mu m$ ,  $a_s = 2\mu m$ ,  $a_l = 16\mu m$ ,  $R_{ICS} = 69\%$ ; (b) Case 2 where  $d = 20\mu m$ ,  $a_s = 3\mu m$ ,  $a_l = 20\mu m$ ,  $R_{ICS} = 69\%$ ; (c) Case 3 where  $d = 26\mu m$ ,  $a_s = 4\mu m$ ,  $a_l = 24\mu m$ ,  $R_{ICS} = 69\%$ . (d) Cross section of the heterogeneous model where  $\mu_d = 20\mu m$ ,  $\mu_{a_s} = 3\mu m$ ,  $\mu_{a_l} = 20\mu m$ ,  $R_{ICS} = 69\%$ .

For Model IV, we specifically considered  $\mu_d = 20\mu m$  and  $\sigma_d = 2\mu m$ , resulting in a range of diameters from  $d_{min} = 14\mu m$  to  $d_{max} = 26\mu m$ , and a range of lengths from  $a_{l,min} = 16\mu m$  to  $a_{l,max} = 24\mu m$ .

Furthermore, we introduced three variations of Model I, where we kept the same intracellular space ratio ( $R_{ICS}$ ) but modified the values of  $d$  and  $a_l$ , as shown in Figure 5.3.

### 5.3.2.1 Condition $\delta/\Delta$

We examined the relationship between the observed results  $\lambda_3^o$  and  $\Delta$ , considering various values of  $\delta$  (ranging from 2 to 30 ms) and  $D$  (ranging from 1 to  $2.5\mu m^2/ms$ ) using the Model IV. The results, presented in Figure 5.4, reveal a significant deviation between the observed and theoretical values in ICS, particularly with shorter  $\Delta$  and larger  $D$  (Figure 5.4-c-d).

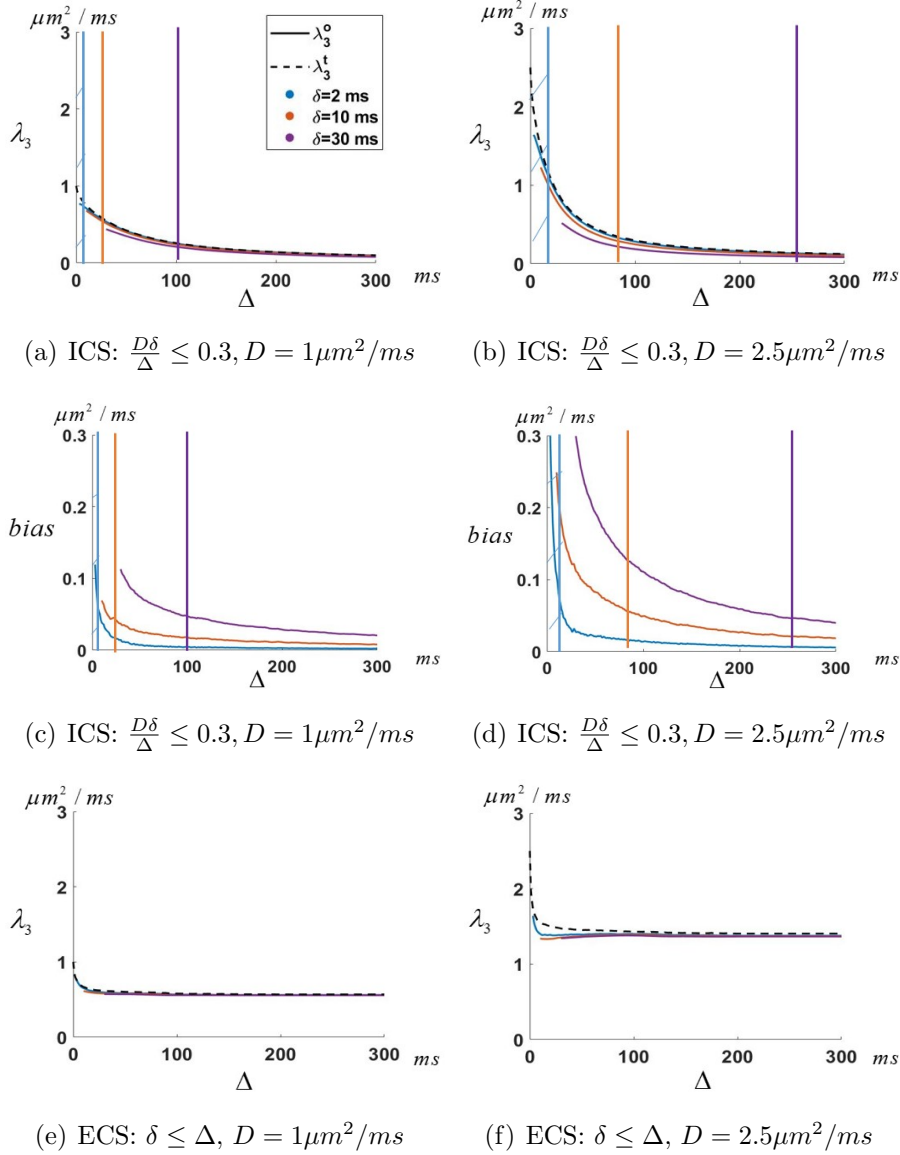


Figure 5.4: Model IV - one voxel: Exploring  $\delta/\Delta$  condition: Evolution of  $\lambda_3^t$  and  $\lambda_3^o$  values wrt  $\Delta$  for  $\delta = 2 - 30\text{ms}$ . First line:  $\lambda_3$  in ICS, second line: observation bias ( $\lambda_3^t - \lambda_3^o$ ) in ICS, third line:  $\lambda_3$  in ECS. Conditions are not satisfied in hatched areas (e.g., for  $\delta = 2\text{ms}$ ) bounded by critical values  $\Delta^{\text{critical}}$  (vertical lines). Blue vertical line for  $\delta = 2\text{ms}$ , orange for  $\delta = 10\text{ms}$ , purple for  $\delta = 30\text{ms}$ . Note that some curves may appear truncated due to the requirement that  $\delta$  must always be smaller than  $\Delta$ . MC parameters:  $N = 10^5, \tau = 0.001\text{ms}$ . Observation parameter:  $b = 500\text{s}/\text{mm}^2$ .

The observed values consistently underestimated the theoretical value, and this bias was more pronounced with larger  $\delta$  in the intracellular space (ICS). However, for  $D_{ICS} = 1\mu m^2/ms$ , as  $\Delta$  increased to 6, 30, and 100 ms for  $\delta$  values of 2, 10, and 30 ms respectively, the observed values gradually approached the theoretical value with a bias smaller than  $0.05\mu m^2/ms$  (Figure 5.4-c). Similar trends were observed for  $D_{ICS} = 2.5\mu m^2/ms$  with specific  $\Delta$  values (Figure 5.4-d). In the extracellular space (ECS),  $\lambda^o$  reached a stable state more rapidly and the curves corresponding to different  $\delta$  values were nearly identical (Figure 5.4-e-f).

Hence, in ICS, this condition depends on  $D$ , whereas in ECS it is independent of  $D$  and only requires compliance with the fact that  $\delta$  should always be smaller than  $\Delta$ . *Condition*  $\frac{\delta}{\Delta}$  can be summarized as follows:

$$\begin{cases} \frac{D\delta}{\Delta} \leq 0.3 & ICS \\ \delta \leq \Delta & ECS \end{cases} \quad (5.5)$$

and when this condition is met, the observed decrease in  $\lambda_o^3$  can be assessed to less than  $0.05\mu m^2/ms$  compared to the theoretical value.

### 5.3.2.2 Condition LDD

The analysis of the theoretical and observed values of  $\lambda_3$  and  $|L_{\lambda_3}|$  with respect to  $\Delta$  was performed in both Models I and Model IV, as shown in Figure 5.5.

Regarding the theoretical values, in ICS,  $|L_{\lambda_3^t}|$  initially increased and then stabilized when satisfying *Condition LDD* (Figure 5.5-c-d), while  $\lambda_3^t$  decreased inversely with  $\Delta$  and depended on the size of  $d$  (Figure 5.5-a-b). Determining the optimal  $\Delta$  in the Model IV was more complex due to the distribution of  $d$ . However, a range of values for  $\Delta$  was identified, highlighting constraints imposed by the smallest and largest restrictions (Figure 5.5, orange arrow). The behavior of  $\lambda_2$  was similar to  $\lambda_3$ .

Considering the observed results, the satisfaction of *Condition LDD* was also based on the theoretical value of  $\Delta^{critical}$ . However, reaching this value was not

Condition LDD:  $\xi_{\Delta} = D\Delta/(s/2)^2 \geq 1$

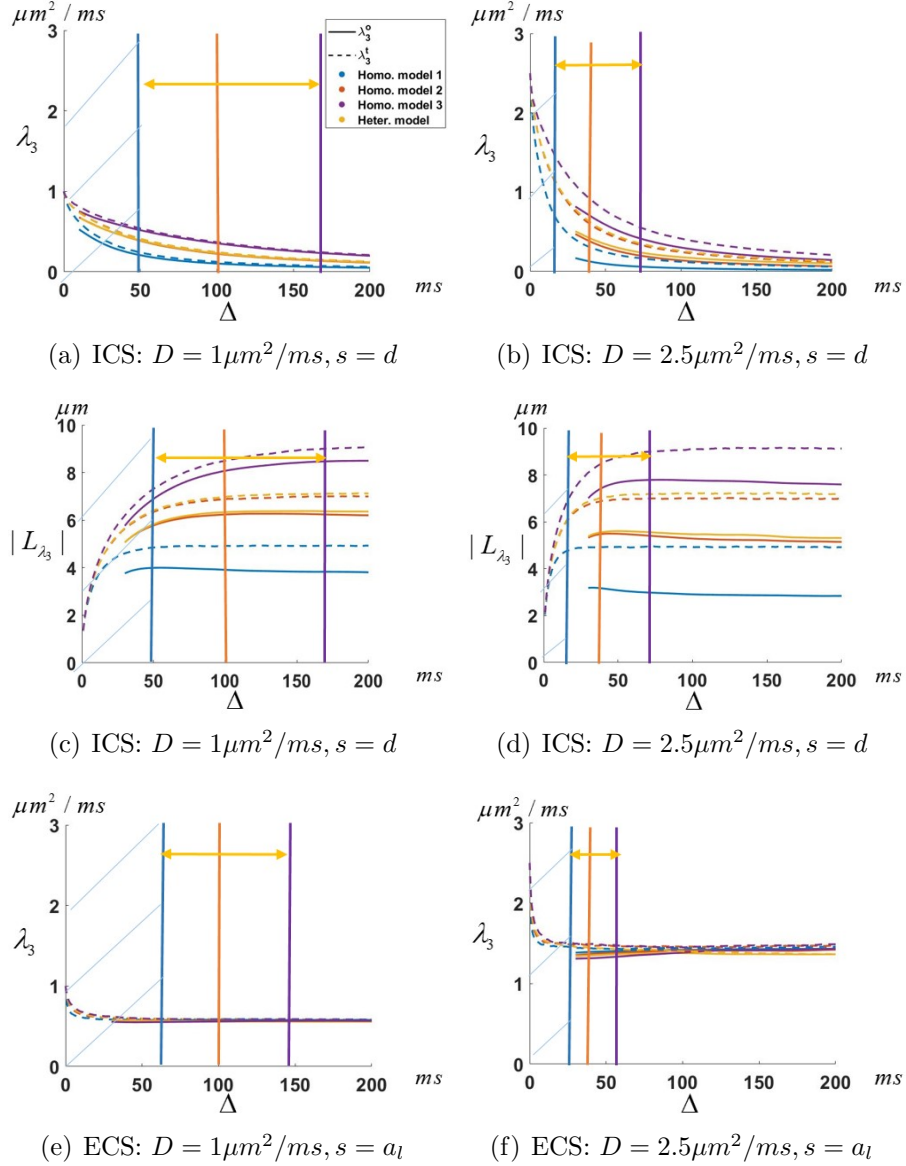


Figure 5.5: Models I and IV one voxel-Exploring LDD condition,  $\xi_{\Delta} = \Delta D/(s/2)^2 \geq 1$ : Evolution of  $\lambda_3^t$  and  $\lambda_3^o$  values wrt  $\Delta$ . First line:  $\lambda_3$  in ICS, second line: corresponding  $|L_{\lambda_3}|$  in ICS, third line:  $\lambda_3$  in ECS. Conditions are not satisfied hatched areas (e.g., for Model I case 1) bounded by critical values  $\Delta^{\text{critical}}$  (vertical lines) where  $\xi_{\Delta}(\Delta = \Delta^{\text{critical}}) = 1$ . Blue vertical line for Model I case 1, orange for Model I case 2, purple for Model I case 3. A horizontal arrow indicates the range of  $\Delta^{\text{critical}}$  for the heterogeneous model. Note that some curves may appear truncated due to the requirement that  $\delta$  must always be smaller than  $\Delta$ . MC parameters:  $N = 10^5, \tau = 0.001\text{ms}$ . Observation parameters:  $\delta = 30\text{ms}, b = 500\text{s}/\text{mm}^2$ .

always possible due to the constraint that  $\Delta$  must be greater than  $\delta$  (values provided in Table 5.3). Notably, a bias existed between the theoretical and observed values, particularly evident in the curves of  $|L_{\lambda_3^t}|$ . This bias is attributed to the discrepancy in the estimation of displacement between the theoretical and observed values (see Figure 5.1-b).

Table 5.3: Critical values of  $\Delta$  that satisfy the *LDD Condition* according to Figure 5.5, depending on the tissue model characteristics ( $d$ ,  $\mu_d$ ,  $a_l$  and  $\mu_{a_l}$ ) and compartments (ICS and ECS).

Theoretical $\Delta$ values				
Diffusivity ( $\mu m^2/ms$ )	ICS			
	Homogeneous			Hetero.
	$d = 14\mu m$	$d = 20\mu m$	$d = 26\mu m$	$\mu_d = 20\mu m$
$D = 1$	49 ms	100 ms	169 ms	[49,169] ms
$D = 2.5$	20 ms	40 ms	68 ms	[20,68] ms
Observed $\Delta$ values ( $\delta = 30ms$ )				
$D = 1$	49 ms	100 ms	169 ms	[49,169] ms
$D = 2.5$	30 ms	40 ms	68 ms	[30,68] ms

Theoretical $\Delta$ values				
Diffusivity ( $\mu m^2/ms$ )	ECS			
	Homogeneous			Hetero.
	$a_l = 16\mu m$	$a_l = 20\mu m$	$a_l = 24\mu m$	$\mu_{a_l} = 20\mu m$
$D = 1$	64 ms	100 ms	144 ms	[64,144] ms
$D = 2.5$	26 ms	40 ms	58 ms	[26,58] ms
Observed $\Delta$ values ( $\delta = 30ms$ )				
$D = 1$	64 ms	100 ms	144 ms	[64,144] ms
$D = 2.5$	30 ms	40 ms	58 ms	[30,58] ms

In ECS, the theoretical values of  $\lambda_3^t$  demonstrated a decrease and stabilization (Figure 5.5-e-f), indicating the fulfillment of *Condition LDD*. The curves reached a stable state more rapidly for smaller  $a_l$  and larger  $D$ . Interestingly, the curves from different models converged to the same stable state due to shared  $R_{ICS}$ , and higher diffusivity led to higher  $\lambda_3^t$ . The constant value of  $ADC_{radial}$  was solely determined by  $R_{ICS}$  and  $D_{ECS}$ . Similar results were observed between the Model

IV with  $\mu_{a_l} = 20\mu m$  and Model I with  $a_l = 20\mu m$ . To detect most restrictions in the Model IV with  $a_{l,max} = 24\mu m$ , the longest  $\Delta$  (corresponding to the largest  $a_l$ ) should be chosen.

In summary, *Condition LDD* is expressed by Equation 5.6, where  $s_{ICS} = d$  and  $s_{ECS} = a_l$ . The critical value  $\Delta^{critical}$  is calculated when  $\xi_\Delta$  equals 1, with values provided in Table 5.3.  $\Delta^{critical}$  increases as  $D$  decreases and either  $d$  (in ICS) or  $a_l$  (in ECS) increases.

$$\xi_\Delta = \frac{\Delta \times D}{(s/2)^2} \geq 1. \quad (5.6)$$

Additionally, we estimated  $FWHM^t$  and cell diameter  $d^t$  from  $L_{\lambda_3^t}$  in ICS for the heterogeneous model, as listed in Table 5.4. When  $\xi_\Delta \geq 1$ ,  $FWHM^t$  and  $d^t$  showed minimal increase with  $\Delta$ , and there was little difference between the estimated  $d^t$  and the real value when  $\xi_\delta \geq 0.5$  ( $18.4\mu m$  vs  $20\mu m$ ).

Table 5.4: Estimated  $FWHM^t$  and  $d^t$  from  $|L_{\lambda_3^t}|$  in ICS for different  $\Delta$  ( $\xi_\Delta$ ) in the case of heter. model with  $\mu_d = 20\mu m$  and  $D = 1\mu m^2/ms$ .

$\Delta$ (ms)	20	40	50	100	150
$\xi_\Delta$	0.2	0.4	0.5	1	1.5
$ L_{\lambda_3^t} (\mu m)$	5.0	6.1	6.4	7.0	7.1
$FWHM^t(\mu m)$	11.8	14.4	15.1	16.4	16.7
$d^t(\mu m)$	14.4	17.5	18.4	20.0	20.4

### 5.3.2.3 Condition SGP

Figure 5.6-a-b presents the evolution of  $\lambda_3^o$  with varying  $\delta$ , considering different  $d$  and  $D_{ICS}$  values, while satisfying the *Conditions LDD* with  $\Delta = 170ms$ .

Condition SGP:  $\xi_\delta = D\delta/(s/2)^2 \leq 0.3$

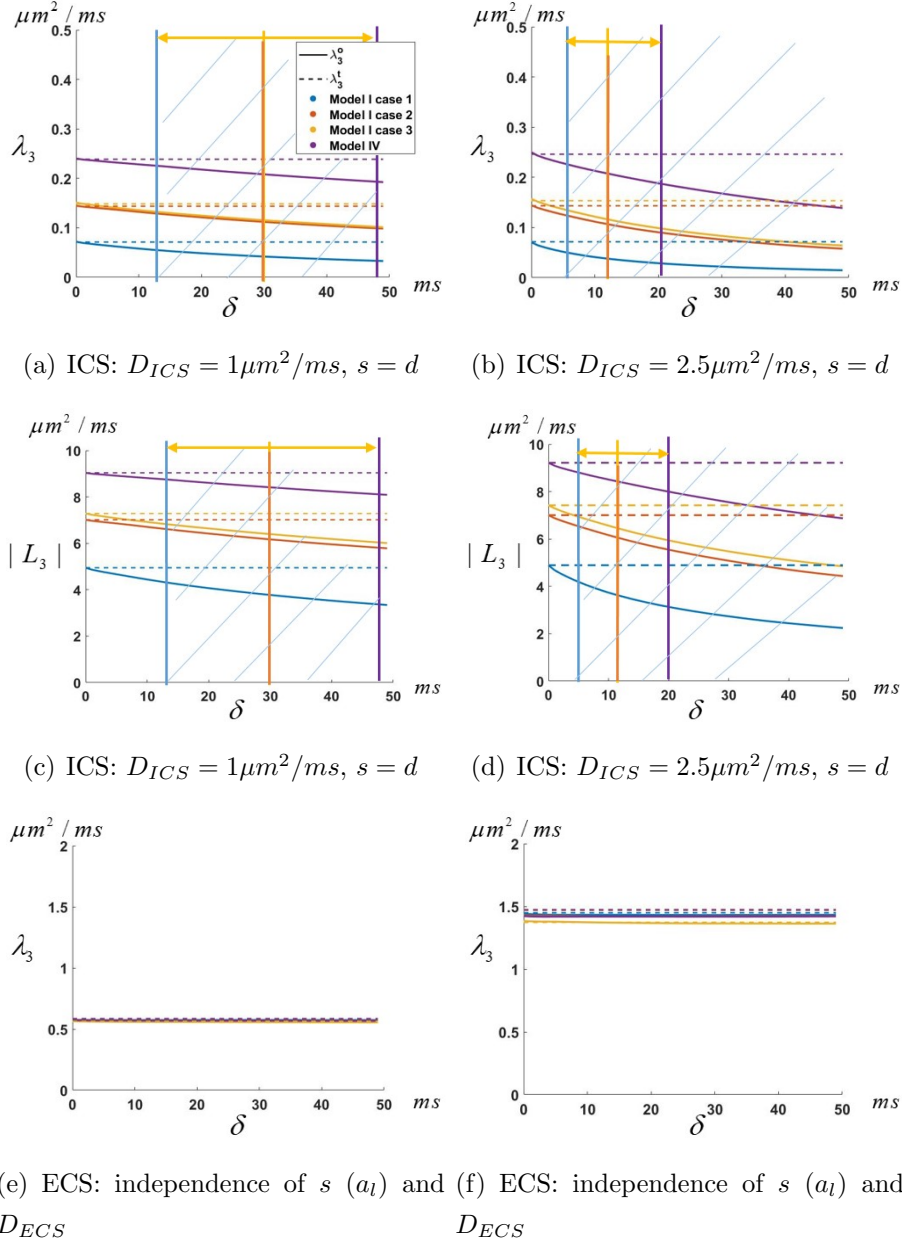


Figure 5.6: Models I and IV one voxel-Exploring *SGP* condition,  $\xi_\delta = \delta D/(s/2)^2 \leq 0.3$ : Evolution of  $\lambda_3^t$  and  $\lambda_3^o$  values wrt  $\delta$  for  $\Delta = 170ms$ . First line:  $\lambda_3$  in ICS, second line: corresponding  $|L_{\lambda_3}|$  in ICS, third line:  $\lambda_3$  in ECS. Conditions are not satisfied in hatched areas (e.g., for Model I case 1) bounded by critical values  $\delta^{critical}$  (vertical lines) in ICS where  $\xi_\delta(\delta = \delta^{critical}) = 0.3$ . Blue vertical line for Model I case 1, orange for Model I case 2, purple for Model I case 3. A horizontal arrow indicates the range of  $\delta^{critical}$  for the heterogeneous model. MC parameters:  $N = 10^5$ ,  $\tau = 0.001ms$ . Observation parameters:  $\Delta = 170ms$ ,  $b = 500s/mm^2$ .

Both the Models I and Model IV were employed to analyze the observed values of  $\lambda_3^o$ . As  $\delta$  increases, the rate of decrease in  $\lambda_3^o$  becomes progressively slower, with a more rapid decrease observed for larger values of  $D_{ICS}$  and  $d$ . Notably, the Model IV with  $\mu_d = 20\mu\text{m}$  closely aligns with the results of the Model I with  $d = 20\mu\text{m}$ . The behavior of  $|L_{\lambda_3^o}|$  corresponds to that of  $\lambda_3^o$ , as shown in Figure 5.6-c-d, and the bias in the observed values ( $L_{\lambda_3^o}$ ) is more pronounced for larger  $\delta$ ,  $D_{ICS}$ , and smaller cell diameter, consistent with Figure 5.5-c-d.

When a finite  $\delta$  is used, the spin is labeled with the position of its center of mass during the gradient pulse, as illustrated in Figure 5.1-b. Consequently, the estimated displacement represents the distance between the average positions of the spin during the gradient pulses. In restricted geometries, the average position tends to converge towards the centroid of the restricted compartment, leading to a decrease in the estimated displacement as  $\delta$  increases [127].

Moving on to Figure 5.6-e-f, the curves of  $\lambda_3^o$  are presented for different  $a_l$  and  $D_{ECS}$  values in ECS, while satisfying the *Conditions LDD* with  $\Delta = 170\text{ms}$ . Both Models I and Model IV are considered. It is observed that  $\lambda_3^o$  remains relatively stable with respect to  $\delta$ , indicating that the diffusion process in ECS is largely independent of  $a_l$ , approximating free diffusion with a certain diffusivity. Additionally, when the *Condition LDD* is satisfied,  $\lambda_3^o$  remains stable with respect to  $\Delta$ , as demonstrated in Figure 5.5-e-f. Furthermore, the heterogeneous case with  $\mu_d = 20\mu\text{m}$  exhibits results that closely resemble those of the homogeneous case with  $d = 20\mu\text{m}$ .

*Condition SGP* can be expressed as follows:

$$\begin{cases} \xi_{\delta,ICS} = \delta \times D_{ICS}/(d/2)^2 \leq 0.3 & ICS \\ \delta \leq \Delta & ECS \end{cases} \quad (5.7)$$

Under the condition  $\xi_{\delta} \leq 0.3$ , the normalized bias of  $\lambda_3^o$  in ICS can be reduced to less than 20%, and the corresponding bias for  $|L_{\lambda_3^o}|$  is approximately 12%. The critical value of  $\delta$  is provided in Table 5.5, and the results from ICS demonstrate that  $\delta^{critical}$  increases with larger values of  $d$  and smaller values of  $D_{ICS}$ . Furthermore, we estimated  $FWHM^o$  and the cell diameter  $d^o$  from  $L_{\lambda_3^o}$  in the

heterogeneous model, and the results are listed in Table 5.6. When  $\xi_\delta$  is up to 0.3,  $FWHM^o$  and  $d^o$  decrease by approximately 12%, from  $17.1\mu m$  to  $15.1\mu m$  and from  $20.9\mu m$  to  $18.4\mu m$ , respectively.

Table 5.5: Critical values of  $\delta$  that satisfy the *SGP Condition* under *LDD Condition*, as determined by tissue model characteristics ( $d$ ,  $\mu_d$ ,  $a_l$  and  $\mu_{a_l}$ ) in ICS.

Observed $\delta$ values				
$\Delta$ (ms)	ICS			
	Homogeneous			Hetero.
	$D_{ICS} = 1\mu m^2/ms$			
	d=14 $\mu m$	d=20 $\mu m$	d=26 $\mu m$	$\mu_d = 20\mu m$
$\Delta = 50$	15 ms	/	/	/
$\Delta = 100$	15 ms	30 ms	/	/
$\Delta = 169$	15 ms	30 ms	48 ms	[15,48] ms
	$D_{ICS} = 2.5\mu m^2/ms$			
	d=14 $\mu m$	d=20 $\mu m$	d=26 $\mu m$	$\mu_d = 20\mu m$
$\Delta = 20$	6 ms	/	/	/
$\Delta = 40$	6 ms	12 ms	/	/
$\Delta = 68$	6 ms	12 ms	19 ms	[6,19] ms

Table 5.6: Estimated  $FWHM^o$  and  $d^o$  from  $|L_{\lambda_3^o}|$  in ICS for different  $\delta$  ( $\xi_\delta$ ) when *Condition LDD* is satisfied in the case of heter. model with  $\mu_d = 20\mu m$ .

$\delta$ (ms)	0.1	5	10	20	30	50
$\xi_\delta$	0.001	0.05	0.1	0.2	0.3	0.5
$ L_{\lambda_3^o} (\mu m)$	7.3	7.1	7.0	6.7	6.4	6.0
$FWHM^o(\mu m)$	17.1	16.8	16.4	15.7	15.1	14.1
$d^o(\mu m)$	20.9	20.4	20.0	19.2	18.4	17.3

## 5.4 Conclusion

**In this contribution**, we investigated three conditions (*Conditions*  $\delta/\Delta$ , *LDD*, and *SGP*) in both the intracellular and extracellular compartments using the four tissue models proposed in Chapter 3 and the corresponding ground truth built in Chapter 4.

Previous studies have examined these conditions in single-cell models [128, 136] and collections of cell models (without studying the extra-cellular space)[129,

91, 147]. Our findings indicate that in ICS, the conditions for  $D\delta/\Delta \leq 0.3$ ,  $\xi_\Delta = D_{ICS}\Delta/(d/2)^2 \geq 1$ , and  $\xi_\delta = D_{ICS}\delta/(d/2)^2 \leq 0.3$  need to be satisfied. In ECS, the condition  $\xi_\Delta = D_{ECS}\Delta/(a_l/2)^2 \geq 1$  is relevant. It was observed that the effect of  $\delta$  in ECS was not significant, rendering the *Conditions*  $\delta/\Delta$  and *SGP* inapplicable in this compartment. Our results emphasize the challenge of parameterizing observations in ICS, where improper parameterization can lead to a systematic underestimation of diffusion.

The factor  $\xi_\Delta$  effectively describes the impact of restriction on molecule diffusion. When  $\xi_\Delta \ll 1$ , the molecules experience unrestricted diffusion, and the dMRI signal primarily depends on the intrinsic diffusion coefficient  $D$ . Achieving small values of  $\xi_\Delta$  in the restricted direction is challenging. Experimental measurements by Seland et al. [24] in rat myocardium tissue showed  $\xi_{\Delta,ICS} = 0.035$  and  $\xi_{\Delta,ECS} = 0.0875$  using specific imaging parameters and morphometric data [11]. Our simulations revealed a rapid decrease in  $\lambda_3^g$  in the initial diffusion stages (see Figure 5.4), particularly in ECS, with estimated errors of approximately 10% in ICS and 40% in ECS.

In the case of  $\xi_\Delta < 1$ , where some molecules experience restricted diffusion,  $\lambda_3$  becomes a function of  $\Delta$ , spatial restriction size ( $d$ ), and diffusivity according to the analytical resolution [110, 112]. For  $\xi_\Delta \geq 1$ , the majority of molecules experience restriction, and  $\lambda_3$  in ICS becomes solely dependent on the restriction size, while  $\lambda_3$  in ECS is primarily related to the size of the intracellular space ( $R_{ICS}$ ) and the extracellular diffusivity ( $D_{ECS}$ ) [110, 112]. These findings are consistent with the analytical resolution and are supported by our simulation results. Longer  $\Delta$  leads to a greater decrease in  $\lambda_3$  compared to  $\lambda_1$ , enhancing image contrast [125]. However, in practical dMRI acquisitions, longer  $\Delta$  can lead to undesired signal attenuation and increased acquisition time, compromising image quality [124, 142].

The *LDD Condition* states that the diffusion duration  $\Delta$  should be long enough to satisfy  $\xi_\Delta \geq 1$ . Our results further demonstrate that the critical value of  $\Delta$  is sensitive to changes in diameter. For cardiac tissue with a mean myocyte diameter of  $20\mu m$ ,  $\Delta \geq 100ms$  was required. Moreover, when  $\xi_\Delta \geq 0.5$ , the estimated cell

diameter approached the real value, corresponding to  $\Delta \geq 50ms$ . However, many clinical cardiac diffusion MRI studies utilize shorter  $\Delta$  values (e.g.,  $\Delta = 10-50ms$  as listed in Table 5.1), which fail to meet the *LDD Condition*.

The effect of the gradient pulse duration ( $\delta$ ) is limited when the condition  $\xi_\delta \leq 0.3$  specified by the *SGP Condition* is satisfied. In this case, the observed  $\lambda_3^g$  decreases by less than 20% when the *LDD Condition* is fulfilled. Similar trends are observed for the estimated  $|L^o|$ ,  $FWHM^o$ , and  $d^o$ . Our findings are consistent with previous studies that estimated spatial restriction size and analyzed the bias of the *SGP Condition*. For instance, a Monte Carlo simulation with a single  $20\mu m$  cylinder reported a decrease in estimated spatial restriction size to  $18.2\mu m$  when  $\xi_\delta = 0.5$  [147], which is consistent with our simulation result of  $17.3\mu m$ . The choice of  $\Delta$  and  $\delta$  is critical for accurate dMRI estimation. Insufficient diffusion time or excessively long gradient pulse duration may prevent the fulfillment of the *LDD* and *SGP conditions*, resulting in underestimation of cell diameters. Conversely, excessively long diffusion time or excessively short gradient pulse duration may compromise the sensitivity of diffusion measurements to changes in cell diameters. Our results also demonstrate that the critical value of  $\delta$  is sensitive to changes in diameter. In brain tissue, where the size of axons is typically several micrometers [98, 97], the bias can be substantial.

Hence, the careful selection of  $\Delta$  and  $\delta$  is crucial for accurate dMRI estimation. Insufficient diffusion time or excessively long gradient pulse duration may result in the failure to satisfy the *LDD* and *SGP conditions*, leading to the underestimation of cell diameters. Conversely, excessively long diffusion time or excessively short gradient pulse duration may limit the sensitivity of diffusion measurements to changes in cell diameters.

# Chapter 6

## General conclusion and prospects

### 6.1 Summary of contributions

In this work, we developed a robust Monte Carlo simulation pipeline to observe water molecule diffusion in cardiac tissue using dMRI. To do so, we addressed three main challenges. Firstly, realistic biological tissue models were required to accurately represent the structural and physical characteristics of the cardiac tissue. Secondly, the simulation required a sufficient number of simulated water molecules and simulation updates to ensure accuracy. As the size and complexity of the virtual tissue model increased, the computational cost also increased. Lastly, the detection of microstructural information in cardiac tissue was limited by the clinical imaging sequence settings.

To address these challenges, we made several contributions. Firstly, **in chapter 3**, we constructed a simplified cardiac tissue model that captured the essential structural and physical characteristics of the heart. We used a simplified cell model, cylinders, to control the heterogeneous size and orientation of cells. The model incorporated five key parameters: cell diameter, diffusivity, permeability, cellular volume fraction, and transmural cell orientation change.

Furthermore, **in chapter 4**, we investigated four conditions to optimize the Monte Carlo simulation parameters. These optimizations were performed on the cardiac tissue model with a cell diameter of  $20\mu m$ . We determined that the simulation updates duration ( $\tau$ ) should be less than or equal to 0.1 ms, the number of simulated molecules ( $N$ ) should be greater than or equal to  $10^5$ , and the voxel size should be larger than  $500 \times 500 \times 500\mu m^3$  to ensure stability and reliability of the simulation results. We also found that the ratio between the length of a simulation step ( $l$ ) and the size of the confinement ( $s$ ) should be limited to  $l/s < 0.05$ . The stability of the simulation results depended on the stable mean value of the cell model diameter ( $d$ ) and the stable cellular volume fraction ( $R_{ICS}$ ). These conditions can be applied to Monte Carlo simulations of other biological tissue models (e.g., brain, muscle, lung) with specific cell sizes and diffusivity values.

Lastly, **in chapter 5**, we generated virtual dMRI signals by applying the Pulsed Gradient Spin-Echo (PGSE) sequence and provided recommendations on sequence parameters for obtaining diffusion property and microstructural information of cardiac tissue. We validated three conditions (*Conditions*  $\delta/\Delta$ , *LDD*, and *SGP*) in both the intracellular and extracellular compartments for both homogeneous and heterogeneous models. Longer  $\Delta$  durations were required to satisfy *Condition LDD*, although this was limited by clinical settings, particularly in biological tissues with larger cell sizes. Longer  $\delta$  durations led to significant biases in *Condition SGP*. However, we quantitatively analyzed the bias using the factor  $\delta D_{ICS}/(d/2)^2$  when *Condition LDD* was satisfied.

## 6.2 Discussion and future research

To enhance the realism of tissue models, high spatial resolution imaging techniques such as polarized illumination imaging (PLI) or synchrotron radiation phase-contrast micro-tomography (SR-PCT) could be incorporated. These techniques provide additional information on the 3D fiber orientation and myocardial

laminar structure, improving the realism of the whole heart model. Furthermore, Monte Carlo simulations provide a ground truth for understanding the relationship between structural and physical characteristics and dMRI outputs. By exploring a wide range of parameter values found in the literature, we can determine which parameters critically influence the model output.

An extension of our research involves exploring the impact of pathologies on diffusion MRI measurements in cardiac tissue. Pathological conditions often result in altered cellular structure, such as changes in cell diameter. By incorporating different cell diameters into our cardiac tissue model, we can investigate how these variations affect diffusion properties and microstructural information. This extension allows us to better understand the relationship between pathological changes and diffusion MRI observations, providing valuable insights into the diagnostic potential of dMRI in detecting and characterizing cardiac pathologies.

Furthermore, studying the heart in motion is an essential aspect to consider in cardiac imaging. The beating motion of the heart introduces additional challenges for diffusion MRI analysis, as the tissue undergoes dynamic changes during the cardiac cycle. Incorporating a varying cell height parameter into our model enables the simulation of the heart's motion, mimicking the pulsatile nature of cardiac tissue. This extension allows us to investigate the influence of cardiac motion on diffusion measurements and evaluate the feasibility of capturing dynamic microstructural changes using dMRI. By considering the interplay between diffusion properties and motion-induced alterations, we can gain a deeper understanding of the cardiac microstructure and its relationship with functional dynamics.

These extensions to pathologies and the study of the heart in motion broaden the applicability of our research, offering insights into the diagnostic potential of diffusion MRI in pathological conditions and advancing our understanding of the complex interplay between cardiac microstructure and function.

## 6.3 Author's contributions

### 6.3.1 Journal articles

- Yuhan Jing, Isabelle E. Magnin, Carole Frindel, "Monte Carlo simulation of water diffusion through cardiac tissue models", *Medical Engineering & Physics*, pp. 104013, 2023.
- Yuhan Jing, Isabelle E. Magnin, Carole Frindel, "Optimizing observation parameters for accurate MRI measurement of water diffusion in a cardiac tissue model", **submitted to** *Computer Methods and Programs in Biomedicine*, July 2023.

### 6.3.2 International conference proceedings

- Yuhan Jing, Carole Frindel, Isabelle E. Magnin, "Simulation of water diffusion through a simple virtual cardiac cell model: optimization of Monte Carlo parameters and observation by simulated MRI", *15th IEEE International Conference on Signal Processing*, pp. 527-532, 2020.

# Bibliography

- [1] I. J. LeGrice, B. Smaill, L. Chai, S. Edgar, J. Gavin, and P. J. Hunter, “Laminar structure of the heart: ventricular myocyte arrangement and connective tissue architecture in the dog,” *American Journal of Physiology-Heart and Circulatory Physiology*, vol. 269, no. 2, pp. H571–H582, 1995.
- [2] O. Bernus, A. Radjenovic, M. L. Trew, I. J. LeGrice, G. B. Sands, D. R. Magee, B. H. Smaill, and S. H. Gilbert, “Comparison of diffusion tensor imaging by cardiovascular magnetic resonance and gadolinium enhanced 3d image intensity approaches to investigation of structural anisotropy in explanted rat hearts,” *Journal of Cardiovascular Magnetic Resonance*, vol. 17, no. 1, pp. 1–27, 2015.
- [3] L. Wang, Y. Hong, Y.-B. Qin, X.-Y. Cheng, F. Yang, J. Yang, and Y.-M. Zhu, “Connecting macroscopic diffusion metrics of cardiac diffusion tensor imaging and microscopic myocardial structures based on simulation,” *Medical Image Analysis*, vol. 77, p. 102325, 2022.
- [4] E. O. Stejskal and J. E. Tanner, “Spin diffusion measurements: spin echoes in the presence of a time-dependent field gradient,” *The journal of chemical physics*, vol. 42, no. 1, pp. 288–292, 1965.
- [5] I. Mekkaoui, K. Moulin, P. Croisille, J. Pousin, and M. Viallon, “Quantifying the effect of tissue deformation on diffusion-weighted mri: a mathematical model and an efficient simulation framework applied to cardiac diffusion imaging,” *Physics in Medicine & Biology*, vol. 61, no. 15, p. 5662, 2016.

- [6] K. D. Costa, Y. Takayama, A. D. McCulloch, and J. W. Covell, "Laminar fiber architecture and three-dimensional systolic mechanics in canine ventricular myocardium," *American Journal of Physiology-Heart and Circulatory Physiology*, vol. 276, no. 2, pp. H595–H607, 1999.
- [7] D. A. Hooks, K. A. Tomlinson, S. G. Marsden, I. J. LeGrice, B. H. Smaill, A. J. Pullan, and P. J. Hunter, "Cardiac microstructure: implications for electrical propagation and defibrillation in the heart," *Circulation research*, vol. 91, no. 4, pp. 331–338, 2002.
- [8] M.-T. Wu, W.-Y. I. Tseng, M.-Y. M. Su, C.-P. Liu, K.-R. Chiou, V. J. Wedeen, T. G. Reese, and C.-F. Yang, "Diffusion tensor magnetic resonance imaging mapping the fiber architecture remodeling in human myocardium after infarction: correlation with viability and wall motion," *Circulation*, vol. 114, no. 10, pp. 1036–1045, 2006.
- [9] S. Zhang, J. A. Crow, X. Yang, J. Chen, A. Borazjani, K. B. Mullins, W. Chen, R. C. Cooper, R. M. McLaughlin, and J. Liao, "The correlation of 3d dt-mri fiber disruption with structural and mechanical degeneration in porcine myocardium," *Annals of biomedical engineering*, vol. 38, no. 10, pp. 3084–3095, 2010.
- [10] J. Chen, S.-K. Song, W. Liu, M. McLean, J. S. Allen, J. Tan, S. A. Wickline, and X. Yu, "Remodeling of cardiac fiber structure after infarction in rats quantified with diffusion tensor mri," *American Journal of Physiology-Heart and Circulatory Physiology*, vol. 285, no. 3, pp. H946–H954, 2003.
- [11] H. Vliegen, A. v. d. LAARSE, J. Huysman, E. Wijnvoord, M. Mentar, C. Cornelisse, and F. Eulderink, "Morphometric quantification of myocyte dimensions validated in normal growing rat hearts and applied to hypertrophic human hearts," *Cardiovascular research*, vol. 21, no. 5, pp. 352–357, 1987.
- [12] C. Basso, K. Michaud, G. d'Amati, J. Banner, J. Lucena, K. Cunningham, O. Leone, A. Vink, A. C. van der Wal, and M. N. Sheppard, "Cardiac hypertrophy at autopsy," *Virchows Archiv*, vol. 479, no. 1, pp. 79–94, 2021.

- [13] Y. Su, L. Zhong, C.-W. Lim, D. Ghista, T. Chua, and R.-S. Tan, “A geometrical approach for evaluating left ventricular remodeling in myocardial infarct patients,” *Computer methods and programs in biomedicine*, vol. 108, no. 2, pp. 500–510, 2012.
- [14] S. M. Haddad and A. Samani, “A novel micro-to-macro approach for cardiac tissue mechanics,” *Computer methods in Biomechanics and Biomedical engineering*, vol. 20, no. 2, pp. 215–229, 2017.
- [15] M. Noorman, M. A. van der Heyden, T. A. van Veen, M. G. Cox, R. N. Hauer, J. M. de Bakker, and H. V. van Rijen, “Cardiac cell–cell junctions in health and disease: electrical versus mechanical coupling,” *Journal of molecular and cellular cardiology*, vol. 47, no. 1, pp. 23–31, 2009.
- [16] M. R. Celes, D. Torres-Dueñas, C. M. Prado, E. C. Campos, J. E. Moreira, F. Q. Cunha, and M. A. Rossi, “Increased sarcolemmal permeability as an early event in experimental septic cardiomyopathy: a potential role for oxidative damage to lipids and proteins,” *Shock*, vol. 33, no. 3, pp. 322–331, 2010.
- [17] M. Rienks, A.-P. Papageorgiou, N. G. Frangogiannis, and S. Heymans, “Myocardial extracellular matrix: an ever-changing and diverse entity,” *Circulation research*, vol. 114, no. 5, pp. 872–888, 2014.
- [18] T. Mayhew, A. Pharaoh, A. Austin, and D. Fagan, “Stereological estimates of nuclear number in human ventricular cardiomyocytes before and after birth obtained using physical disectors,” *The Journal of Anatomy*, vol. 191, no. 1, pp. 107–115, 1997.
- [19] R. Bolli, D. W. Losordo, and H. Ardehali, *Manual of Research Techniques in Cardiovascular Medicine*. John Wiley & Sons, 2013.
- [20] B. Bastide, T. Jarry-Guichard, J. Briand, J. Deleze, and D. Gros, “Effect of antipeptide antibodies directed against three domains of connexin43 on the gap junctional permeability of cultured heart cells,” *The Journal of membrane biology*, vol. 150, no. 3, pp. 243–253, 1996.

- [21] T. Ogura, S. Imanishi, and T. Shibamoto, “Osmometric and water-transporting properties of guinea pig cardiac myocytes,” *The Japanese journal of physiology*, vol. 52, no. 4, pp. 333–342, 2002.
- [22] L. KF, L. F, T. T, G. JH, S. CH, F. M, and F. JD, “Regional variations in the apparent diffusion coefficient and the intracellular distribution of water in rat brain during acute focal ischemia,” *Stroke*, vol. 32, no. 8, pp. 1897–1905, 2001.
- [23] P. Van Zijl, C. Moonen, P. Faustino, J. Pekar, O. Kaplan, and J. S. Cohen, “Complete separation of intracellular and extracellular information in nmr spectra of perfused cells by diffusion-weighted spectroscopy,” *Proceedings of the National Academy of Sciences*, vol. 88, no. 8, pp. 3228–3232, 1991.
- [24] J. G. Seland, M. Bruvold, H. Anthonsen, H. Brurok, W. Nordhøy, P. Jynge, and J. Krane, “Determination of water compartments in rat myocardium using combined d-t1 and t1-t2 experiments,” *Magnetic resonance imaging*, vol. 23, no. 2, pp. 353–354, 2005.
- [25] L. Garrido, V. J. Wedeen, K. K. Kwong, U. M. Spencer, and H. L. Kantor, “Anisotropy of water diffusion in the myocardium of the rat,” *Circulation research*, vol. 74, no. 5, pp. 789–793, 1994.
- [26] Y.-F. Chen, R. A. Redetzke, R. M. Sivertson, T. S. Coburn, L. R. Cypher, and A. M. Gerdes, “Post-myocardial infarction left ventricular myocyte remodeling: are there gender differences in rats?,” *Cardiovascular Pathology*, vol. 20, no. 5, pp. e189–e195, 2011.
- [27] M. A. Rossi and L. C. Peres, “Effect of captopril on the prevention and regression of myocardial cell hypertrophy and interstitial fibrosis in pressure overload cardiac hypertrophy,” *American Heart Journal*, vol. 124, no. 3, pp. 700–709, 1992.
- [28] A. M. Gerdes, J. A. Moore, J. M. Hines, P. Kirkland, and S. P. Bishop, “Regional differences in myocyte size in normal rat heart,” *The Anatomical Record*, vol. 215, no. 4, pp. 420–426, 1986.

- [29] N. J. Severs, “The cardiac muscle cell,” *Bioessays*, vol. 22, no. 2, pp. 188–199, 2000.
- [30] H. Satoh, L. Delbridge, L. A. Blatter, and D. M. Bers, “Surface: volume relationship in cardiac myocytes studied with confocal microscopy and membrane capacitance measurements: species-dependence and developmental effects,” *Biophysical journal*, vol. 70, no. 3, pp. 1494–1504, 1996.
- [31] H. G. Benedicto, P. P. Bombonato, G. Macchiarelli, G. Stifano, and I. M. Prado, “Structural arrangement of the cardiac collagen fibers of healthy and diabetic dogs,” *Microscopy Research and Technique*, vol. 74, no. 11, pp. 1018–1023, 2011.
- [32] L. Axel, V. J. Wedeen, and D. B. Ennis, “Probing dynamic myocardial microstructure with cardiac magnetic resonance diffusion tensor imaging,” 2014.
- [33] C. Pinali, H. J. Bennett, J. B. Davenport, J. L. Caldwell, T. Starborg, A. W. Trafford, and A. Kitmitto, “Three-dimensional structure of the intercalated disc reveals plicate domain and gap junction remodeling in heart failure,” *Biophysical journal*, vol. 108, no. 3, pp. 498–507, 2015.
- [34] A. Grimm, K. Katele, and H.-L. Lin, “Fiber bundle direction in the mammalian heart. an extension of the” nested shells” model,” *Basic research in cardiology*, vol. 71, no. 4, pp. 381–388, 1976.
- [35] M. Spach, P. Dolber, and J. Heidlage, “Influence of the passive anisotropic properties on directional differences in propagation following modification of the sodium conductance in human atrial muscle. a model of reentry based on anisotropic discontinuous propagation.,” *Circulation research*, vol. 62, no. 4, pp. 811–832, 1988.
- [36] P. W. Hales, J. E. Schneider, R. A. Burton, B. J. Wright, C. Bollensdorff, and P. Kohl, “Histo-anatomical structure of the living isolated rat heart in two contraction states assessed by diffusion tensor mri,” *Progress in biophysics and molecular biology*, vol. 110, no. 2-3, pp. 319–330, 2012.

- [37] S. Wang, F. Varray, W. Liu, P. Clarysse, and I. E. Magnin, “Measurement of local orientation of cardiomyocyte aggregates in human left ventricle free wall samples using x-ray phase-contrast microtomography,” *Medical Image Analysis*, vol. 75, p. 102269, 2022.
- [38] J. A. Erlebacher, J. L. Weiss, M. L. Weisfeldt, and B. H. Bulkley, “Early dilation of the infarcted segment in acute transmural myocardial infarction: role of infarct expansion in acute left ventricular enlargement,” *Journal of the American College of Cardiology*, vol. 4, no. 2, pp. 201–208, 1984.
- [39] M. A. Pfeffer and E. Braunwald, “Ventricular remodeling after myocardial infarction. experimental observations and clinical implications.,” *Circulation*, vol. 81, no. 4, pp. 1161–1172, 1990.
- [40] H.-G. Zimmer, A. M. Gerdes, S. Lortet, and G. Mall, “Changes in heart function and cardiac cell size in rats with chronic myocardial infarction,” *Journal of molecular and cellular cardiology*, vol. 22, no. 11, pp. 1231–1243, 1990.
- [41] H. F. Weisman, D. E. Bush, J. A. Mannisi, and B. H. Bulkley, “Global cardiac remodeling after acute myocardial infarction: a study in the rat model,” *Journal of the American College of Cardiology*, vol. 5, no. 6, pp. 1355–1362, 1985.
- [42] E. K. Espe, J. M. Aronsen, M. Eriksen, O. M. Sejersted, L. Zhang, and I. Sjaastad, “Regional dysfunction after myocardial infarction in rats,” *Circulation: Cardiovascular Imaging*, vol. 10, no. 9, p. e005997, 2017.
- [43] A. Ross and D. Streeter Jr, “Myocardial fiber disarray.,” *Circulation*, vol. 60, no. 6, pp. 1425–1426, 1979.
- [44] P.-S. Jouk, Y. Usson, G. Michalowicz, and F. Parazza, “Mapping of the orientation of myocardial cells by means of polarized light and confocal scanning laser microscopy,” *Microscopy research and technique*, vol. 30, no. 6, pp. 480–490, 1995.

- [45] C. Frindel, M. Robini, P. Croisille, and Y.-M. Zhu, “Comparison of regularization methods for human cardiac diffusion tensor mri,” *Medical image analysis*, vol. 13, no. 3, pp. 405–418, 2009.
- [46] C. Frindel, M. Robini, J. Schaerer, P. Croisille, and Y.-M. Zhu, “A graph-based approach for automatic cardiac tractography,” *Magnetic Resonance in Medicine*, vol. 64, no. 4, pp. 1215–1229, 2010.
- [47] P. F. Ferreira, P. J. Kilner, L.-A. McGill, S. Nielles-Vallespin, A. D. Scott, S. Y. Ho, K. P. McCarthy, M. M. Haba, T. F. Ismail, P. D. Gatehouse, *et al.*, “In vivo cardiovascular magnetic resonance diffusion tensor imaging shows evidence of abnormal myocardial laminar orientations and mobility in hypertrophic cardiomyopathy,” *Journal of Cardiovascular Magnetic Resonance*, vol. 16, no. 1, pp. 1–16, 2014.
- [48] P. C. Lauterbur, “Image formation by induced local interactions: examples employing nuclear magnetic resonance,” *nature*, vol. 242, no. 5394, pp. 190–191, 1973.
- [49] M. H. Levitt, *Spin dynamics: basics of nuclear magnetic resonance*. John Wiley & Sons, 2013.
- [50] S. Mori and P. B. Barker, “Diffusion magnetic resonance imaging: its principle and applications,” *The Anatomical Record: An Official Publication of the American Association of Anatomists*, vol. 257, no. 3, pp. 102–109, 1999.
- [51] J. J. Brown, T. M. Peterson, and R. A. Slutsky, “Regional myocardial blood flow, edema formation, and magnetic relaxation times during acute myocardial ischemia in the canine.” *Investigative Radiology*, vol. 20, no. 5, pp. 465–471, 1985.
- [52] M. A. Bernstein, K. F. King, and X. J. Zhou, *Handbook of MRI pulse sequences*. Elsevier, 2004.
- [53] C. Westbrook and J. Talbot, *MRI in Practice*. John Wiley & Sons, 2018.

- [54] D. Moratal, A. Vallés-Luch, L. Martí-Bonmatí, and M. E. Brummer, “k-space tutorial: an mri educational tool for a better understanding of k-space,” *Biomedical imaging and intervention journal*, vol. 4, no. 1, 2008.
- [55] D. Taylor and M. Bushell, “The spatial mapping of translational diffusion coefficients by the nmr imaging technique,” *Physics in medicine & biology*, vol. 30, no. 4, p. 345, 1985.
- [56] K.-D. Merboldt, W. Hanicke, and J. Frahm, “Self-diffusion nmr imaging using stimulated echoes,” *Journal of Magnetic Resonance (1969)*, vol. 64, no. 3, pp. 479–486, 1985.
- [57] M. Moseley, J. Kucharczyk, J. Mintorovitch, Y. Cohen, J. Kurhanewicz, N. Derugin, H. Asgari, and D. Norman, “Diffusion-weighted mr imaging of acute stroke: correlation with t2-weighted and magnetic susceptibility-enhanced mr imaging in cats.,” *American Journal of Neuroradiology*, vol. 11, no. 3, pp. 423–429, 1990.
- [58] G. J. Strijkers, A. Bouts, W. M. Blankesteyn, T. H. Peeters, A. Vilanova, M. C. van Prooijen, H. M. Sanders, E. Heijman, and K. Nicolay, “Diffusion tensor imaging of left ventricular remodeling in response to myocardial infarction in the mouse,” *NMR in Biomedicine: An International Journal Devoted to the Development and Application of Magnetic Resonance In vivo*, vol. 22, no. 2, pp. 182–190, 2009.
- [59] L.-A. McGill, T. F. Ismail, S. Nielles-Vallespin, P. Ferreira, A. D. Scott, M. Roughton, P. J. Kilner, S. Y. Ho, K. P. McCarthy, P. D. Gatehouse, *et al.*, “Reproducibility of in-vivo diffusion tensor cardiovascular magnetic resonance in hypertrophic cardiomyopathy,” *Journal of Cardiovascular Magnetic Resonance*, vol. 14, no. 1, pp. 1–15, 2012.
- [60] A. Das, A. Chowdhary, C. Kelly, I. Teh, C. T. Stoeck, S. Kozerke, N. Maxwell, T. P. Craven, N. J. Jex, C. E. Saunderson, *et al.*, “Insight into myocardial microstructure of athletes and hypertrophic cardiomyopathy patients using diffusion tensor imaging,” *Journal of Magnetic Resonance Imaging*, vol. 53, no. 1, pp. 73–82, 2021.

- [61] Y. Cohen and Y. Assaf, “High b-value q-space analyzed diffusion-weighted mrs and mri in neuronal tissues—a technical review,” *NMR in Biomedicine: An International Journal Devoted to the Development and Application of Magnetic Resonance In Vivo*, vol. 15, no. 7-8, pp. 516–542, 2002.
- [62] D. Le Bihan, E. Breton, D. Lallemand, P. Grenier, E. A. Cabanis, and M. Laval-Jeantet, “MR imaging of intravoxel incoherent motions: application to diffusion and perfusion in neurologic disorders.,” *Radiology*, vol. 161, no. 2, pp. 401–407, 1986.
- [63] S. Rapacchi, H. Wen, M. Viallon, D. Grenier, P. Kellman, P. Croisille, and V. M. Pai, “Low b-value diffusion-weighted cardiac magnetic resonance imaging: initial results in humans using an optimal time-window imaging approach,” *Investigative radiology*, vol. 46, no. 12, p. 751, 2011.
- [64] K. Moulin, M. Viallon, W. Romero, A. Chazot, N. Mewton, K. Isaaz, and P. Croisille, “Mri of reperfused acute myocardial infarction edema: Adc quantification versus t1 and t2 mapping,” *Radiology*, vol. 295, no. 3, pp. 542–549, 2020.
- [65] P. Basser, J. Mattiello, and D. LeBihan, “Estimation of the effective self-diffusion tensor from the nmr spin echo,” *Journal of Magnetic Resonance, Series B*, vol. 103, no. 3, pp. 247–254, 1994.
- [66] S. H. Gilbert, G. B. Sands, I. J. LeGrice, B. H. Smaill, O. Bernus, and M. L. Trew, “A framework for myoarchitecture analysis of high resolution cardiac mri and comparison with diffusion tensor mri,” in *2012 Annual International Conference of the IEEE Engineering in Medicine and Biology Society*, pp. 4063–4066, IEEE, 2012.
- [67] F. Poveda, D. Gil, E. Martí, A. Andaluz, M. Ballester, and F. Carreras, “Helical structure of the cardiac ventricular anatomy assessed by diffusion tensor magnetic resonance imaging with multiresolution tractography,” *Revista Española de Cardiología (English Edition)*, vol. 66, no. 10, pp. 782–790, 2013.

- [68] C. Mekkaoui, S. Huang, G. Dai, T. G. Reese, A. Thiagalingam, P. Maurovich-Horvat, J. Ruskin, U. Hoffmann, M. P. Jackowski, and D. E. Sosnovik, “Left ventricular remodeling following myocardial infarction revealed with a quantitative diffusion mri tractography framework,” *Journal of Cardiovascular Magnetic Resonance*, vol. 14, no. 1, pp. 1–2, 2012.
- [69] C. Lenglet, M. Rousson, R. Deriche, and O. Faugeras, “Statistics on the manifold of multivariate normal distributions: Theory and application to diffusion tensor mri processing,” *Journal of Mathematical Imaging and Vision*, vol. 25, no. 3, pp. 423–444, 2006.
- [70] Y. Assaf and O. Pasternak, “Diffusion tensor imaging (dti)-based white matter mapping in brain research: a review,” *Journal of molecular neuroscience*, vol. 34, no. 1, pp. 51–61, 2008.
- [71] D. E. Sosnovik, R. Wang, G. Dai, T. G. Reese, and V. J. Wedeen, “Diffusion mr tractography of the heart,” *Journal of Cardiovascular Magnetic Resonance*, vol. 11, no. 1, pp. 1–15, 2009.
- [72] L. L. Cooper, K. E. Odening, M.-S. Hwang, L. Chaves, L. Schofield, C. A. Taylor, A. S. Gemignani, G. F. Mitchell, J. R. Forder, B.-R. Choi, *et al.*, “Electromechanical and structural alterations in the aging rabbit heart and aorta,” *American Journal of Physiology-Heart and Circulatory Physiology*, vol. 302, no. 8, pp. H1625–H1635, 2012.
- [73] E. W. Hsu, A. Muzikant, S. Matulevicius, R. Penland, and C. Henriquez, “Magnetic resonance myocardial fiber-orientation mapping with direct histological correlation,” *American Journal of Physiology-Heart and Circulatory Physiology*, vol. 274, no. 5, pp. H1627–H1634, 1998.
- [74] D. F. Scollan, A. Holmes, R. Winslow, and J. Forder, “Histological validation of myocardial microstructure obtained from diffusion tensor magnetic resonance imaging,” *American Journal of Physiology-Heart and Circulatory Physiology*, vol. 275, no. 6, pp. H2308–H2318, 1998.
- [75] J. Chen, W. Liu, H. Zhang, L. Lacy, X. Yang, S.-K. Song, S. A. Wickline, and X. Yu, “Regional ventricular wall thickening reflects changes in cardiac

- fiber and sheet structure during contraction: quantification with diffusion tensor mri,” *American Journal of Physiology-Heart and Circulatory Physiology*, vol. 289, no. 5, pp. H1898–H1907, 2005.
- [76] S. Nielles-Vallespin, Z. Khalique, P. F. Ferreira, R. de Silva, A. D. Scott, P. Kilner, L.-A. McGill, A. Giannakidis, P. D. Gatehouse, D. Ennis, *et al.*, “Assessment of myocardial microstructural dynamics by in vivo diffusion tensor cardiac magnetic resonance,” *Journal of the American College of Cardiology*, vol. 69, no. 6, pp. 661–676, 2017.
- [77] M. Lohezic, I. Teh, C. Bollensdorff, R. Peyronnet, P. W. Hales, V. Grau, P. Kohl, and J. E. Schneider, “Interrogation of living myocardium in multiple static deformation states with diffusion tensor and diffusion spectrum imaging,” *Progress in biophysics and molecular biology*, vol. 115, no. 2-3, pp. 213–225, 2014.
- [78] H. Wei, M. Viallon, B. M. Delattre, L. Wang, V. M. Pai, H. Wen, H. Xue, C. Guetter, P. Croisille, and Y. Zhu, “Assessment of cardiac motion effects on the fiber architecture of the human heart in vivo,” *IEEE transactions on medical imaging*, vol. 32, no. 10, pp. 1928–1938, 2013.
- [79] D. Le Bihan, J.-F. Mangin, C. Poupon, C. A. Clark, S. Pappata, N. Molko, and H. Chabriat, “Diffusion tensor imaging: concepts and applications,” *Journal of Magnetic Resonance Imaging: An Official Journal of the International Society for Magnetic Resonance in Medicine*, vol. 13, no. 4, pp. 534–546, 2001.
- [80] B. M. Delattre, M. Viallon, H. Wei, Y. M. Zhu, T. Feiweier, V. M. Pai, H. Wen, and P. Croisille, “In vivo cardiac diffusion-weighted magnetic resonance imaging: quantification of normal perfusion and diffusion coefficients with intravoxel incoherent motion imaging,” *Investigative radiology*, vol. 47, no. 11, p. 662, 2012.

- [81] C. Nguyen, Z. Fan, B. Sharif, Y. He, R. Dharmakumar, D. S. Berman, and D. Li, “In vivo three-dimensional high resolution cardiac diffusion-weighted mri: a motion compensated diffusion-prepared balanced steady-state free precession approach,” *Magnetic resonance in medicine*, vol. 72, no. 5, pp. 1257–1267, 2014.
- [82] W.-Y. I. Tseng, T. G. Reese, R. M. Weisskoff, and V. J. Wedeen, “Cardiac diffusion tensor mri in vivo without strain correction,” *Magnetic Resonance in Medicine: An Official Journal of the International Society for Magnetic Resonance in Medicine*, vol. 42, no. 2, pp. 393–403, 1999.
- [83] J. Dou, T. G. Reese, W.-Y. I. Tseng, and V. J. Wedeen, “Cardiac diffusion mri without motion effects,” *Magnetic Resonance in Medicine: An Official Journal of the International Society for Magnetic Resonance in Medicine*, vol. 48, no. 1, pp. 105–114, 2002.
- [84] A. H. Aletras, S. Ding, R. S. Balaban, and H. Wen, “Dense: displacement encoding with stimulated echoes in cardiac functional mri,” *Journal of magnetic resonance (San Diego, Calif.: 1997)*, vol. 137, no. 1, p. 247, 1999.
- [85] C. A. Clark and D. Le Bihan, “Water diffusion compartmentation and anisotropy at high b values in the human brain.,” *Magnetic Resonance in Medicine*, vol. 44, no. 6, pp. 852–859, 2000.
- [86] J. Kärgler, “Nmr self-diffusion studies in heterogeneous systems,” *Advances in Colloid and Interface Science*, vol. 23, pp. 129–148, 1985.
- [87] W. S. Price, A. V. Barzykin, K. Hayamizu, and M. Tachiya, “A model for diffusive transport through a spherical interface probed by pulsed-field gradient nmr,” *Biophysical journal*, vol. 74, no. 5, pp. 2259–2271, 1998.
- [88] C. Meier, W. Dreher, and D. Leibfritz, “Diffusion in compartmental systems. i. a comparison of an analytical model with simulations,” *Magnetic Resonance in Medicine: An Official Journal of the International Society for Magnetic Resonance in Medicine*, vol. 50, no. 3, pp. 500–509, 2003.

- [89] T. Niendorf, R. M. Dijkhuizen, D. G. Norris, M. van Lookeren Campagne, and K. Nicolay, “Biexponential diffusion attenuation in various states of brain tissue: implications for diffusion-weighted imaging,” *Magnetic Resonance in Medicine*, vol. 36, no. 6, pp. 847–857, 1996.
- [90] V. J. Wedeen, P. Hagmann, W.-Y. I. Tseng, T. G. Reese, and R. M. Weisskoff, “Mapping complex tissue architecture with diffusion spectrum magnetic resonance imaging,” *Magnetic resonance in medicine*, vol. 54, no. 6, pp. 1377–1386, 2005.
- [91] J. Lätt, M. Nilsson, A. Rydhög, R. Wirestam, F. Ståhlberg, and S. Brockstedt, “Effects of restricted diffusion in a biological phantom: a q-space diffusion mri study of asparagus stems at a 3t clinical scanner,” *Magnetic Resonance Materials in Physics, Biology and Medicine*, vol. 20, no. 4, p. 213, 2007.
- [92] U. Gamper, P. Boesiger, and S. Kozerke, “Diffusion imaging of the in vivo heart using spin echoes—considerations on bulk motion sensitivity,” *Magnetic Resonance in Medicine: An Official Journal of the International Society for Magnetic Resonance in Medicine*, vol. 57, no. 2, pp. 331–337, 2007.
- [93] C. T. Stoeck, C. von Deuster, N. Toussaint, and S. Kozerke, “High-resolution single-shot dti of the in-vivo human heart using asymmetric diffusion encoding,” in *Proceedings of the 21st Annual Meeting of ISMRM, Salt Lake City, Utah, USA*, 2013.
- [94] D. Cory, “Measurement of translational displacement probabilities by nmr: an indicator of compartmentation,” *Magnetic resonance in medicine*, vol. 14, no. 3, pp. 435–444, 1990.
- [95] P. T. Callaghan, “Pulsed-gradient spin-echo nmr for planar, cylindrical, and spherical pores under conditions of wall relaxation,” *Journal of magnetic resonance, Series A*, vol. 113, no. 1, pp. 53–59, 1995.
- [96] H. C. Torrey, “Bloch equations with diffusion terms,” *Phys. Rev.*, vol. 104, pp. 563–565, 1956.

- [97] J. Rafael-Patino, D. Romascano, A. Ramirez-Manzanares, E. J. Canales-Rodríguez, G. Girard, and J.-P. Thiran, “Robust monte-carlo simulations in diffusion-mri: Effect of the substrate complexity and parameter choice on the reproducibility of results,” *Frontiers in neuroinformatics*, vol. 14, p. 8, 2020.
- [98] M. G. Hall and D. C. Alexander, “Convergence and parameter choice for monte-carlo simulations of diffusion mri,” *IEEE transactions on medical imaging*, vol. 28, no. 9, pp. 1354–1364, 2009.
- [99] P. J. Basser, J. Mattiello, and D. LeBihan, “Mr diffusion tensor spectroscopy and imaging,” *Biophysical journal*, vol. 66, no. 1, pp. 259–267, 1994.
- [100] S. E. Maier, S. Vajapeyam, H. Mamata, C.-F. Westin, F. A. Jolesz, and R. V. Mulkern, “Biexponential diffusion tensor analysis of human brain diffusion data,” *Magnetic Resonance in Medicine: An Official Journal of the International Society for Magnetic Resonance in Medicine*, vol. 51, no. 2, pp. 321–330, 2004.
- [101] K. Oshio, H. Shinmoto, and R. V. Mulkern, “Interpretation of diffusion mr imaging data using a gamma distribution model,” *Magnetic Resonance in Medical Sciences*, 2014.
- [102] K. M. Bennett, K. M. Schmainda, R. Bennett, D. B. Rowe, H. Lu, and J. S. Hyde, “Characterization of continuously distributed cortical water diffusion rates with a stretched-exponential model,” *Magnetic Resonance in Medicine: An Official Journal of the International Society for Magnetic Resonance in Medicine*, vol. 50, no. 4, pp. 727–734, 2003.
- [103] G. J. Stanisz, J. G. Li, G. A. Wright, and R. M. Henkelman, “Water dynamics in human blood via combined measurements of t2 relaxation and diffusion in the presence of gadolinium,” *Magnetic resonance in medicine*, vol. 39, no. 2, pp. 223–233, 1998.
- [104] D. S. Novikov, E. Fieremans, J. H. Jensen, and J. A. Helpert, “Random walks with barriers,” *Nature physics*, vol. 7, no. 6, pp. 508–514, 2011.

- [105] E. Fieremans, G. Lemberskiy, J. Veraart, E. E. Sigmund, S. Gyftopoulos, and D. S. Novikov, “In vivo measurement of membrane permeability and myofiber size in human muscle using time-dependent diffusion tensor imaging and the random permeable barrier model,” *NMR in Biomedicine*, vol. 30, no. 3, p. e3612, 2017.
- [106] D. B. Berry, E. K. Englund, V. Galinsky, L. R. Frank, and S. R. Ward, “Varying diffusion time to discriminate between simulated skeletal muscle injury models using stimulated echo diffusion tensor imaging,” *Magnetic resonance in medicine*, vol. 85, no. 5, pp. 2524–2536, 2021.
- [107] L. Avram, Y. Assaf, and Y. Cohen, “The effect of rotational angle and experimental parameters on the diffraction patterns and micro-structural information obtained from q-space diffusion nmr: implication for diffusion in white matter fibers,” *Journal of Magnetic Resonance*, vol. 169, no. 1, pp. 30–38, 2004.
- [108] F. Bloch, “Nuclear induction,” *Physical review*, vol. 70, no. 7-8, p. 460, 1946.
- [109] S. L. Codd and P. T. Callaghan, “Spin echo analysis of restricted diffusion under generalized gradient waveforms: planar, cylindrical, and spherical pores with wall relaxivity,” *Journal of Magnetic Resonance*, vol. 137, no. 2, pp. 358–372, 1999.
- [110] O. Söderman and B. Jönsson, “Restricted diffusion in cylindrical geometry,” *Journal of Magnetic Resonance, Series A*, vol. 117, no. 1, pp. 94–97, 1995.
- [111] A. Duh, A. Mohorič, and J. Stepišnik, “Computer simulation of the spin-echo spatial distribution in the case of restricted self-diffusion,” *Journal of Magnetic Resonance*, vol. 148, no. 2, pp. 257–266, 2001.
- [112] A. Szafer, J. Zhong, and J. C. Gore, “Theoretical model for water diffusion in tissues,” *Magnetic resonance in medicine*, vol. 33, no. 5, pp. 697–712, 1995.

- [113] E. Fieremans, D. S. Novikov, J. H. Jensen, and J. A. Helpert, “Monte carlo study of a two-compartment exchange model of diffusion,” *NMR in Biomedicine*, vol. 23, no. 7, pp. 711–724, 2010.
- [114] B. Balinov, B. Jonsson, P. Linse, and O. Soderman, “The nmr self-diffusion method applied to restricted diffusion. simulation of echo attenuation from molecules in spheres and between planes,” *Journal of Magnetic Resonance, Series A*, vol. 104, no. 1, pp. 17–25, 1993.
- [115] C. Cai, Z. Chen, S. Cai, and J. Zhong, “Propagator formalism and computer simulation of restricted diffusion behaviors of inter-molecular multiple-quantum coherences,” *Physica B: Condensed Matter*, vol. 366, no. 1-4, pp. 127–137, 2005.
- [116] E. Fieremans, Y. De Deene, S. Delputte, M. S. Özdemir, Y. D’Asseler, J. Vlassenbroeck, K. Deblaere, E. Achten, and I. Lemahieu, “Simulation and experimental verification of the diffusion in an anisotropic fiber phantom,” *Journal of magnetic resonance*, vol. 190, no. 2, pp. 189–199, 2008.
- [117] J. Bates, I. Teh, D. McClymont, P. Kohl, J. E. Schneider, and V. Grau, “Monte carlo simulations of diffusion weighted mri in myocardium: validation and sensitivity analysis,” *IEEE transactions on medical imaging*, vol. 36, no. 6, pp. 1316–1325, 2017.
- [118] B. A. Landman, J. A. Farrell, S. A. Smith, D. S. Reich, P. A. Calabresi, and P. C. Van Zijl, “Complex geometric models of diffusion and relaxation in healthy and damaged white matter,” *NMR in Biomedicine: An International Journal Devoted to the Development and Application of Magnetic Resonance In vivo*, vol. 23, no. 2, pp. 152–162, 2010.
- [119] C.-H. Yeh, B. Schmitt, D. Le Bihan, J.-R. Li-Schlittgen, C.-P. Lin, and C. Poupon, “Diffusion microscopist simulator: a general monte carlo simulation system for diffusion magnetic resonance imaging,” *PloS one*, vol. 8, no. 10, p. e76626, 2013.
- [120] M. Nilsson, J. Lätt, F. Ståhlberg, D. van Westen, and H. Hagslätt, “The importance of axonal undulation in diffusion mr measurements: a monte

- carlo simulation study,” *NMR in Biomedicine*, vol. 25, no. 5, pp. 795–805, 2012.
- [121] N. Naughton and J. Georgiadis, “Connecting diffusion mri to skeletal muscle microstructure: Leveraging meta-models and gpu-acceleration,” in *Proceedings of the Practice and Experience in Advanced Research Computing on Rise of the Machines (learning)*, pp. 1–7, 2019.
- [122] M. G. Hall and C. A. Clark, “Diffusion in hierarchical systems: A simulation study in models of healthy and diseased muscle tissue,” *Magnetic resonance in medicine*, vol. 78, no. 3, pp. 1187–1198, 2017.
- [123] L. Wang, Y.-M. Zhu, H. Li, W. Liu, and I. E. Magnin, “Simulation of diffusion anisotropy in dti for virtual cardiac fiber structure,” in *International Conference on Functional Imaging and Modeling of the Heart*, pp. 95–104, Springer, 2011.
- [124] M. Nilsson, J. Lätt, E. Nordh, R. Wirestam, F. Ståhlberg, and S. Brockstedt, “On the effects of a varied diffusion time in vivo: is the diffusion in white matter restricted?,” *Magnetic resonance imaging*, vol. 27, no. 2, pp. 176–187, 2009.
- [125] L. Wang, *Modélisation et Simulation de l’IRM de Diffusion des Fibres Myocardiques*. PhD thesis, Lyon, INSA, 2013.
- [126] M. G. Hall and D. C. Alexander, “Finite pulse widths improve fibre orientation estimates in diffusion tensor mri,” in *Proc. Intl. Soc. Mag. Reson. Med.*, vol. 14, p. 1076, 2006.
- [127] C. H. Yeh, *Diffusion Microscopist Simulator-The Development and Application of a Monte Carlo Simulation System for Diffusion MRI*. PhD thesis, Université Paris Sud-Paris XI; National Yang-Ming University (Taiwan), 2011.
- [128] W. S. Price, “Pulsed-field gradient nuclear magnetic resonance as a tool for studying translational diffusion: Part 1. basic theory,” *Concepts in Magnetic Resonance: An Educational Journal*, vol. 9, no. 5, pp. 299–336, 1997.

- [129] P. P. Mitra and B. I. Halperin, “Effects of finite gradient-pulse widths in pulsed-field-gradient diffusion measurements,” *Journal of Magnetic Resonance, Series A*, vol. 113, no. 1, pp. 94–101, 1995.
- [130] L. Wang, Y. Zhu, H. Li, W. Liu, and I. E. Magnin, “Multiscale modeling and simulation of the cardiac fiber architecture for dmri,” *IEEE Transactions on Biomedical Engineering*, vol. 59, no. 1, pp. 16–19, 2011.
- [131] J. N. Rose, S. Nielles-Vallespin, P. F. Ferreira, D. N. Firmin, A. D. Scott, and D. J. Doorly, “Novel insights into in-vivo diffusion tensor cardiovascular magnetic resonance using computational modelling and a histology-based virtual microstructure,” *Magnetic resonance in medicine*, vol. 81, no. 4, pp. 2759–2773, 2019.
- [132] Y. Jing, C. Frindel, and I. E. Magnin, “Simulation of water diffusion through a simple virtual cardiac cell model: optimization of monte carlo parameters and observation by simulated mri,” in *2020 15th IEEE International Conference on Signal Processing (ICSP)*, vol. 1, pp. 527–532, IEEE, 2020.
- [133] I. Alemany, J. N. Rose, J. Garnier-Brun, A. D. Scott, and D. J. Doorly, “Random walk diffusion simulations in semi-permeable layered media with varying diffusivity,” *arXiv preprint arXiv:2201.09609*, 2022.
- [134] K. Ginsburger, F. Poupon, J. Beaujoin, D. Estournet, F. Matuschke, J.-F. Mangin, M. Axer, and C. Poupon, “Improving the realism of white matter numerical phantoms: a step toward a better understanding of the influence of structural disorders in diffusion mri,” *Frontiers in Physics*, vol. 6, p. 12, 2018.
- [135] M. Lashgari, N. Ravikumar, I. Teh, J.-R. Li, D. L. Buckley, J. E. Schneider, and A. F. Frangi, “Three-dimensional micro-structurally informed in silico myocardium—towards virtual imaging trials in cardiac diffusion weighted mri,” *Medical Image Analysis*, p. 102592, 2022.
- [136] Y. Jing, C. Frindel, and I. E. Magnin, “Simulation of water diffusion through a simple virtual cardiac cell model: optimization of monte carlo

- parameters and observation by simulated mri,” in *2020 15th IEEE International Conference on Signal Processing (ICSP)*, vol. 1, pp. 527–532, IEEE, 2020.
- [137] M. G. Hall, G. Nadjati-Gilani, and D. C. Alexander, “Realistic voxel sizes and reduced signal variation in monte-carlo simulation for diffusion MR data synthesis,” *arXiv preprint arXiv:1701.03634*, 2017.
- [138] G. Marsaglia, “Choosing a point from the surface of a sphere,” *Annals of Mathematical Statistics*, vol. 43, pp. 645–646, 1972.
- [139] A. Einstein, *Investigations on the Theory of the Brownian Movement*. Courier Corporation, 1956.
- [140] R. Nossin-Manor, R. Duvdevani, and Y. Cohen, “Effect of experimental parameters on high b-value q-space mr images of excised rat spinal cord,” *Magnetic Resonance in Medicine: An Official Journal of the International Society for Magnetic Resonance in Medicine*, vol. 54, no. 1, pp. 96–104, 2005.
- [141] A. Bar-Shir, L. Avram, E. Ozarslan, P. J. Basser, and Y. Cohen, “The effect of the diffusion time and pulse gradient duration ratio on the diffraction pattern and the structural information estimated from q-space diffusion mr: experiments and simulations,” *Journal of magnetic resonance*, vol. 194 2, pp. 230–236, 2008.
- [142] M.-C. Chou, E.-F. Kao, and S. Mori, “Effects of b-value and echo time on magnetic resonance diffusion tensor imaging-derived parameters at 1.5 t: a voxel-wise study,” *J Med Biol Eng*, vol. 33, no. 1, pp. 45–50, 2013.
- [143] M. Nilsson, J. Lätt, E. Nordh, R. Wirestam, F. Ståhlberg, and S. Brockstedt, “On the effects of a varied diffusion time in vivo: is the diffusion in white matter restricted?,” *Magnetic resonance imaging*, vol. 27 2, pp. 176–187, 2009.
- [144] K. Moulin, A. Chazot, J. Chaptinel, P. Croisille, and M. Viallon, “Comparison of three diffusion encoding schemes for cardiac imaging under free

- breathing conditions.,” *Journal of Cardiovascular Magnetic Resonance*, vol. 18, no. 1, pp. 1–3, 2016.
- [145] M. G. Hall, G. L. Nedjati-Gilani, and D. C. Alexander, “Monte-carlo simulation of diffusion mri with realistic voxel sizes,” in *Proc. Intl. Soc. Mag. Reson. Med.*, vol. 22, p. 2643, 2013.
- [146] K. M. Hasan and P. A. Narayana, “Computation of the fractional anisotropy and mean diffusivity maps without tensor decoding and diagonalization: theoretical analysis and validation,” *Magnetic Resonance in Medicine: An Official Journal of the International Society for Magnetic Resonance in Medicine*, vol. 50, no. 3, pp. 589–598, 2003.
- [147] J. Latt, M. Nilsson, C. Malmberg, H. Rosquist, R. Wirestam, F. Stahlberg, D. Topgaard, and S. Brockstedt, “Accuracy of  $q$ -space related parameters in mri: Simulations and phantom measurements,” *IEEE transactions on medical imaging*, vol. 26, no. 11, pp. 1437–1447, 2007.



## FOLIO ADMINISTRATIF

### THESE DE L'INSA LYON, MEMBRE DE L'UNIVERSITE DE LYON

NOM : JING

DATE de SOUTENANCE : 23.10.2023

(avec précision du nom de jeune fille, le cas échéant)

Prénoms : Yuhan

TITRE : Monte Carlo simulation of water diffusion through cardiac tissue and observation by virtual MRI

NATURE : Doctorat

Numéro d'ordre : 2023ISAL0076

Ecole doctorale : EDISS

Spécialité : Ingénierie biomédicale

RESUME : Cardiovascular diseases remain one of the most serious health problems in the world, motivating research that deepens our understanding of the myocardial function. There are still large shadow areas in the understanding of the relationships between the mechanical function, hemodynamic/perfusion/diffusion/percolation/transfer rate and the adaptive structural changes emerging in cardiac diseases (Cardiomyopathy, ischemia). To better understand the way the water molecules diffuse within the cardiac tissue, the Ph.D. will build a simulator able to mimic the motion of water molecules through both simple and realistic virtual 3D cardiac tissue models and will couple it to a Virtual Magnetic Resonance Imaging device able to image the Diffusion (v\_DMRI)

MOTS-CLÉS : Monte-Carlo simulation, water diffusion, microstructure, cardiac tissue, diffusion magnetic resonance imaging

Laboratoire (s) de recherche :CREATIS

Directeur de thèse: Carole FRINDEL

Président de jury : Cyril Poupon

Composition du jury :

Stéphanie Bricq	Maître de Conférences HDR, Université de Bourgogne	Rapporteuse
Cyril Poupon	Directeur de Recherche, CEA NeuroSpin	Rapporteur
Bart Bijmens	Professeur, ICREA	Rapporteur
Carole Lartzien	Directeur de Recherche, INSA-LYON	Examinatrice
Stanislas Rappacchi	Chargé de recherche, Aix-Marseille Université	Examinateur
Carole Frindel	Maître de Conférences HDR, INSA-LYON	Directrice de thèse